

SOME THERMOPHYSICAL AND THERMOCHEMICAL  
PROPERTIES IMPORTANT IN ENCAPSULATED  
BULK CRYSTAL GROWTH OF GaAs

by

HYEON-DEOK LEE

A DISSERTATION PRESENTED TO THE GRADUATE SCHOOL OF THE  
UNIVERSITY OF FLORIDA IN PARTIAL FULFILLMENT OF THE  
REQUIREMENTS FOR THE DEGREE OF DOCTOR OF PHILOSOPHY

UNIVERSITY OF FLORIDA

1991

To  
My Parents

## ACKNOWLEDGMENTS

This work is one of the great adventures in my life and serves as a stepping stone to further quests of academic achievement. However, it could not have been accomplished without the help provided by people around me. Though it is difficult to express it in words, I would like to offer my sincere appreciation to them.

My appreciation to my advisor Professor T. J. Anderson will never be enough. Not to mention his academic advice, his moral encouragement has always been a source of new energy in my daily life. I would also like to thank Professor R. Narayanan, Professor P. Holloway, Professor R. Abbaschian, and Professor S. Svoronos as members of the supervisory committee for their advice and support.

I would like to extend my thanks to all of my colleagues in our research group for their friendship and caring. Special thanks are deserving to Chinho, Jaesoo, Sungmin, and Sangkook for their encouragement throughout this work, and Peter for technical support and his never-ending humor. I also thank Tracy, Ron, Peggy, Nancy, and Shirley for their help and cooperation.

My deepest appreciation and love to my parents, my brother and sisters and their families can never be expressed enough. My parents have always kept me in the right way with their love, patience and understanding. Finally, I would like to express my love to my niece, Boram.

## TABLE OF CONTENT

ACKNOWLEDGMENT .....	iii
ABSTRACT .....	vi
CHAPTERS	
1 INTRODUCTION .....	1
1.1 Importance of GaAs Bulk Crystal Growth .....	1
1.2 Properties of Gallium Arsenide .....	3
1.2.1 Crystal Structure .....	3
1.2.2 Thermal Characteristics .....	6
1.2.3 Band Gap Energy of Gallium Arsenide .....	7
1.2.4 Density of Solid Gallium Arsenide .....	9
1.3 Growth Techniques for Semi-Insulating GaAs .....	10
1.3.1 Liquid Encapsulated Czochralski (LEC) Technique .....	12
1.3.2 Horizontal Bridgman Technique .....	17
1.3.3 Vertical Gradient Freeze Method .....	21
1.3.4 Liquid Encapsulated Melt Zone .....	23
1.4 Overview of Thesis .....	29
2 CHEMISTRY OF INTERACTION BETWEEN GaAs, ENCAPSULANT, AND THE QUARTZ CRUCIBLE .....	31
2.1 Introduction .....	31
2.2 Interaction of $B_2O_3$ with the GaAs Melt and the $SiO_2$ Crucible During Bulk Crystal Growth .....	33
2.2.1 Experimental Description .....	33
2.2.2 Results and Discussion .....	42
2.2.3 Conclusions .....	60
2.3 Development of Alternative Encapsulants for the LEMZ Technique .....	60
2.3.1 Criteria for Selection of Alternative Encapsulants .....	61

	2.3.2 Possible Alternative Encapsulants .....	62
	2.3.3 Experiment .....	65
	2.3.4 Results and Discussion .....	67
3	MEASUREMENT OF THE Ga ACTIVITY ALONG THE Ga-RICH LIQUIDUS AND CRITICAL ASSESSMENT OF THE PHASE DIAGRAM AND THERMOCHEMISTRY OF THE Ga-As SYSTEM .....	83
3.1	Measurement of the Activity of Ga Along the Ga-rich Liquidus .....	85
3.1.1	Theory .....	85
3.1.2	Experimental .....	87
3.1.3	Results and Discussion .....	94
3.2	Optimization of the Thermochemical Properties and Phase Diagram for the Ga-As System .....	99
3.2.1	Introduction .....	99
3.2.2	Data Acquisition .....	101
3.2.3	Optimization Method .....	102
3.2.4	Results and Discussion .....	107
3.2.5	Conclusions .....	108
4	POINT DEFECT STRUCTURE AND IMPURITY INCORPORATION IN BULK GaAs .....	114
4.1	Introduction to Point Defects in GaAs .....	115
4.2	Review of Models of the Native Defect Structure in GaAs .....	117
4.2.1	Models of the Native Point Defect Structure in GaAs .....	117
4.2.2	EL2 in GaAs .....	124
4.2.3	Effect of Thermal Treatment on the EL2 Center .....	126
4.3	Incorporation of Isoelectronic Dopants in GaAs .....	130
4.4	Model for Si-Incorporation in GaAs .....	133
4.4.1	Chemical Equilibrium Model for Si Incorporation .....	134
4.4.2	Application of the Model to Growth of GaAs .....	141
4.4.3	Conclusions .....	154

5	SUMMARY AND RECOMMENDATIONS .....	156
5.1	Chemistry of Interaction Between GaAs, Encapsulant, and the Quartz Crucible .....	156
5.2	Measurement of the Ga Activity Along the Ga-Rich Liquidus and Critical Assessment of the Phase Diagram and Thermochemistry of the Ga-As System .....	158
5.3	The Thermochemical Model of Si Incorporation in GaAs During Crystal Growth .....	159
5.4	Recommendations .....	160
APPENDICES		
1	MEASUREMENT OF THE SURFACE TENSION BETWEEN A LIQUID ENCAPSULANT AND THE GaAs MELT BY THE WILHELMY PLATE METHOD .....	163
2	PROCEDURE FOR CALCULATING THE CONCENTRATION OF EACH DEFECT SPECIES .....	174
REFERENCES .....		179
BIOGRAPHICAL SKETCH .....		190

Abstract of Dissertation Presented to the Graduate School  
of University of Florida in Partial Fulfillment of the  
Requirements for the Degree of Doctor of Philosophy

SOME THERMOPHYSICAL AND THERMOCHEMICAL  
PROPERTIES IMPORTANT IN ENCAPSULATED  
BULK CRYSTAL GROWTH OF GaAs

By

Hyeon-Deok Lee

May, 1991

Chairman: Timothy J. Anderson  
Major Department: Chemical Engineering

Some thermophysical and thermochemical interactions important to encapsulated bulk crystal growth of *GaAs* were investigated. This process involves the contact of *GaAs* solid and liquid with a liquid encapsulant ( $B_2O_3$ -based) and quartz ( $SiO_2$ ). The thermochemical and thermophysical properties of these materials determine the electrical properties of the grown *GaAs* single crystals.

The dissolution kinetics of *Ga-As(l)* and  $SiO_2$  in liquid  $B_2O_3$  were examined in the three-phase *GaAs* melt, encapsulant and quartz system as a function of encapsulant water content and contact time. The *Ga* uptake by liquid  $B_2O_3$  was found to depend on the encapsulant water content, but not on the equilibration time. The

behavior of the *Si* uptake by encapsulant was opposite to that found with *Ga*. The concentrations of *Si* and *B* in the grown *GaAs* were found to be a function of water content in the starting  $B_2O_3$ .

A search for alternative encapsulant materials was initiated. Candidate materials were examined for chemical compatibility with *GaAs* and  $SiO_2$ . The materials studied were mixed oxides and it was hoped to improve crystal quality through alteration of the thermophysical properties, such as surface tension, viscosity and thermal conductivity. The mixed oxide systems,  $B_2O_3+Al_2O_3$ ,  $B_2O_3+La_2O_3$ , and  $B_2O_3+Nb_2O_5$  were found to be chemically compatible. Experimental apparatus to measure the liquid surface tension was constructed and tested.

Thermodynamic studies of *Ga-As* system were carried out in a solid-electrolyte galvanic cell. Using yttria stabilized zirconia as the solid electrolyte, the gallium activity along the liquidus line was measured. The experimental data obtained in this study were used along with the available literature data to assess the thermochemistry and phase diagram of the *Ga-As* system. The results indicate that the experimental activity data obtained in this study are in good agreement with other thermodynamic data from the literature.

A thermochemical model for the point defect structure in *Si*-doped *GaAs* has been developed. This model predicts the total concentration of *Si* and native defect concentrations in melt grown *Si*-doped *GaAs*. A compensation ratio of 0.43 and a segregation coefficient for *Si* of 0.26 was obtained from the model for *GaAs* growth from a stoichiometric melt.



## CHAPTER 1

### INTRODUCTION

#### 1.1 Importance of GaAs Bulk Crystal Growth

Gallium arsenide (*GaAs*) is classified as a group III-V compound semiconductor in the fact that it is composed of an element (*Ga*) from column III and an element (*As*) from column V of the periodic chart. Gallium arsenide has received considerable attention and research effort because it has many superior material properties relative to silicon. Though the technology to produce devices from silicon is in a mature stage, the use of silicon for photonic, optoelectronic and high-speed electronic device applications (e.g., Light Emitting Diodes (LEDs), lasers, infrared detectors, Field Effect Transistors (FETs), and low-noise integrated circuits) is limited by the fundamental material properties of silicon.

On the other hand, the high electron mobility and saturated drift velocity of gallium arsenide make this material suitable for devices operating at high frequencies. Unlike silicon, *GaAs* is available in semi-insulating form. The use of a semi-insulating substrate greatly reduces parasitic capacitances and allows the use of true monolithically integrated circuits operating at high speed (above 1 GHz). In addition, *GaAs* is suitable for space and military application due to a higher radiation hardness. Furthermore, *GaAs* substrates are the template for many heterostructure

devices based on materials in the *AlGaInP*, *AlGaAs* and *InGaAsP* families. This permits the band gap energy to be changed without significantly changing the interatomic distance, thus persevering structural integrity. Importantly, its direct band gap makes it very useful as a base material in optoelectronic and optical components (*e.g.*, LEDs and lasers).

Gallium arsenide is, however, not free from problems. One of the main disadvantages of this material is that metal-oxide-semiconductor (MOS) devices can not be fabricated on gallium arsenide because a suitable native oxide is not available. Therefore, the dominant *GaAs* device is the metal-semiconductor field effect transistor (MESFET). Another problem is that the critical resolved shear stress of *GaAs* is low so that it is prone to breakage during handling and formation of extended defects during thermal processing. Hardening *GaAs* by isoelectronic doping with indium during growth has reduced this problem somewhat. A high concentration of indium, however, causes out-diffusion of indium during device fabrication and lattice mismatch during subsequent epi-layer growth.

In spite of these problems, *GaAs* crystal growth technology has advanced to such an extent over the last two decades that large (4 inch diameter) single crystals now can be routinely produced. There still remains much room for improvement in the crystal quality to meet the high performance demands of devices. Acceptable yields of devices and circuits greatly depends on the thermal stability, low dislocation density, and a uniform high electron mobility in the material, even more so than for *Si*.

## 1.2 Properties of Gallium Arsenide

### 1.2.1. Crystal Structure

Gallium arsenide crystallizes in the sphalerite (Zincblende) lattice and was first produced by Goldschmidt (1) in 1920s. The sphalerite lattice consists of two interpenetrating face-centered cubic (fcc) sublattices, with the origin of the second sublattice located one fourth of the distance along the major diagonal of the first sublattice. The unit cube for *GaAs* is shown in figure 1-1 (a), which depicts the arrangement of *Ga* and *As* atoms in the volume  $a^3$ , where  $a$  is the lattice constant. Each gallium (or arsenic) atom has four nearest neighbor arsenic (or gallium) atoms, with a bond length of  $r_0 = 3^{1/4}a/4$ . These bonds are separated by the tetrahedral bond angle of  $109.47^\circ$ . The unit cell size of undoped *GaAs* single crystal is  $a = 5.65325 \pm 0.00002 \text{ \AA}$  at 300 K (2). Two other values of unit cell size have been reported in the literature (3, 4) and these values are both in good agreement with the above value. The density of stoichiometric *GaAs* at 300 K is  $\rho_{300} = 5.3174 \pm 0.0026 \text{ g/cm}^3$  (3). A number of other properties of *GaAs* are listed in Table 1-1 (5).

The {110} planes of gallium arsenide are the preferred cleavage planes. The reason for this is apparent from the diagram in figure 1-1 (b). The {110} faces contain an equal density of *Ga* and *As* atoms. Each surface atom is attached by one bond to an unlike atom in the lower layer and by two bonds to two nearest neighbors in the surface plane. This leaves a fourth dangling bond. Therefore, interatomic forces are strong within the {110} planes (2 bonds/atom), but weak between adjacent {110} planes (1 bond/atom). The family of {111} planes is also important in *GaAs*

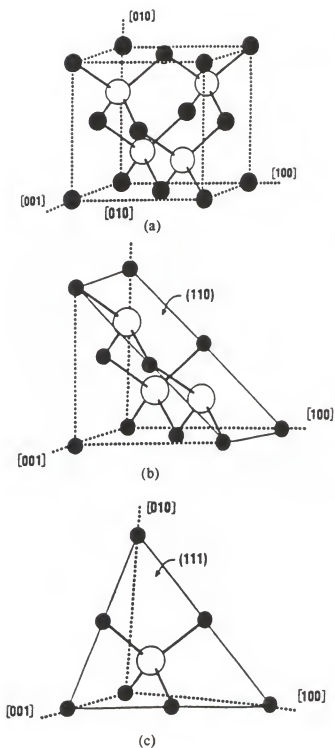


Figure 1-1. GaAs crystal structure. (a) Unit cube of GaAs crystal, (b) Truncation of the GaAs unit cube by the  $(110)$  plane, (c) Truncation of the GaAs unit cube by the  $(111)$  plane.  $\bullet$ : Ga,  $\circ$ : As

Table 1-1. Room Temperature (300 K) Properties of GaAs

Lattice Constant, $a$	5.65325 Å
Density	5.3174 g/cm <sup>3</sup>
Atomic Density	4.4279 x 10 <sup>22</sup> atoms/cm <sup>3</sup>
Molecular Weight	144.642 (69.720 + 74.922) g/mole
Bulk Modulus	7.55 x 10 <sup>11</sup> dyne/cm <sup>2</sup>
Shear Modulus	3.26 x 10 <sup>11</sup> dyne/cm <sup>2</sup>
Linear Expansion Coefficient, $\alpha$	5.73 x 10 <sup>-6</sup> /K
Specific Heat	0.327 J/gK
Lattice Thermal Conductivity, $\kappa_L$	0.55 W/cm K
Dielectric Constant	12.85
Band Gap	1.423 eV
Threshold Field	3.3 KV/cm
Peak Drift Velocity	2.1 x 10 <sup>7</sup> cm/s
Electron Mobility (Undoped)	8500 cm <sup>2</sup> /V s
Hole Mobility (Undoped)	400 cm <sup>2</sup> /V s
Melting Temperature	1511 K

processing technology in the fact that growth is easiest in the  $\langle 111 \rangle$  directions because the  $\{111\}$  planes are the most closely packed. As shown in figure 1-1 (c), each  $\{111\}$  plane contains only one type of atom, either gallium or arsenic. In order to distinguish the *Ga* terminated plane from the *As* terminated plane, the letter A or B is designated to the *Ga* or *As* terminated plane, respectively. Thus,  $\{111A\}$  planes contain only *Ga* atoms and  $\{111B\}$  planes contain only *As* atoms. Since the A and B surface contain different atoms, its chemical behavior is different from each other and different growth or etch rates are observed. For example, many of the chemical etchants for  $\{111B\}$  (6, 7) work poorly for the  $\{111A\}$  surface, producing a slower rate of attack and an irregular surface finish. Crystal growth in the  $\langle 100 \rangle$  direction is highly desirable for *GaAs*, which is difficult to cleave along  $\{111\}$  planes, because  $\{100\}$  *GaAs* cleaves readily along the  $\{110\}$  planes. Cleavage along some of these planes results in a rectangular dice with parallel faces.

#### 1.2.2. Thermal Characteristics

The thermal expansion coefficient ( $\alpha$ ) and thermal conductivity ( $\kappa_L$ ) of *GaAs* are important in crystal growth since both of these properties show rather unusual characteristics over extreme temperature ranges (8), especially for temperatures less than 200 and above 1000 K. The linear coefficient of thermal expansion,  $\alpha$ , which is defined by  $dL/dT = \alpha L$ , where  $L$  is length, has been investigated by several investigators (3, 9-12) with reported values in the range  $4.84 \times 10^{-6}$  to  $6.9 \times 10^{-6} (K^{-1})$ . A quadratic approximation has been used to fit the data from several of these investigators over moderate temperature ranges. A consensus polynomial was

recommended (13) and is given by

$$\alpha(T) = 4.24 \times 10^{-6} + 5.82 \times 10^{-9} T - 2.82 \times 10^{-12} T^2 \quad K^{-1} \quad (1.1)$$

for  $200 < T < 1000 \text{ K}$  (5), which gives a  $300 \text{ K}$  value of  $\alpha_{300} = 5.73 \times 10^{-6}/K$ .

Gallium arsenide is a very poor thermal conductor ( $\kappa_L = 0.55 \text{ W/cm-K}$ ) compared to silicon ( $\kappa_L = 1.5 \text{ W/cm-K}$ ) and its thermal conductivity is reasonably well-behaved over more moderate temperature ranges (5, 14, 15). Blakemore (5) illustrates several investigator's measurements over the approximate range of 200 to 1000 K. The thermal conductivity of *GaAs* has a general trend that as doping level increases, the thermal conductivity decreases.

### 1.2.3. Band Gap Energy of Gallium Arsenide

Temperature Dependence. The band gap energy of *GaAs* has been measured very precisely by optical measurements such as absorption (16-19), reflectance (20-23), and photoluminescence (23, 24). This is possible because gallium arsenide has a direct band gap. The band gap of *GaAs* shows non-linear behavior with temperature. It is shown by Thurmond (25) that the experimental results fitted well with the following equation in the temperature range 0 - 1000 K.

$$E_g(T) = 1.519 - \frac{(5.405 \times 10^{-4}) T^2}{(T+204)} \text{ eV} \quad (1.2)$$

The estimated standard deviation over this temperature range is 3 meV, but it is observed by Blakemore (5) that the fit was much better than this at room temperature and below. It is believed that the deviation of  $E_g$  with temperature is

related to the dialation of the lattice and to electron-phonon interactions. The effect of the dialation of the lattice accounts for a 27 meV decrease in  $E_g$  from 0 to 300 K (26) and can be calculated theoretically from the pressure dependence of  $E_g$ , the bulk modules, and the change in the lattice constant with temperature. The remainder of the variation in  $E_g$  is apparently due to the electron-phonon interactions.

Pressure Dependence. The direct band gap energy of *GaAs* at moderate pressure increases as pressure increases, and above 35 Kbar, *GaAs* becomes an indirect band gap material. The X6 conduction minimum falls in relation to the L6 and  $\Gamma_6$  minima as pressure increases (5), resulting in an indirect band gap. In their study of photocurrent as a function of optical excitation energy of the [100] oriented n-*GaAs*, Zurawsky *et al.* (27) found a pressure dependence of 12.2 meV/Kbar in the 0 - 10 Kbar range. A pressure dependence of  $10.73 \pm 0.05$  meV/Kbar in the 0 - 40 Kbar range was obtained by Wolford and Bradley (28) using photoluminescence and photoluminescence excitation spectroscopy on high purity MOCVD (Metalorganic Chemical Vapor Deposition) n-type gallium arsenide at 4.2 K in a diamond anvil apparatus.

Welber *et al.* (29) subjected *GaAs* to hydrostatic pressure up to 180 Kbar and obtained the following expression for the absorption edge,  $E_g$ , in eV at room temperature.

$$E_g(P) = 1.45 + 0.0126P - 3.77 \times 10^{-5} P^2 \text{ eV} \quad (1.3)$$

where  $P$  is the pressure in Kbars.



#### 1.2.4. Density of Solid Gallium Arsenide

Several authors have reported values of the density of gallium arsenide from both X-ray diffraction and direct measurements. Most of the values are scattered about the value  $5.317 \text{ g/cm}^3$  at room temperature, with only two reported values (30, 31) falling outside the range  $5.305$  to  $5.325 \text{ g/cm}^3$ . From the preferred values of the lattice constants of pure gallium arsenide (32) at room temperature, X-ray densities are found to be in the range of  $5.3158$  to  $5.3164 \text{ g/cm}^3$  with an uncertainty of about 3 in the last decimal place. (A last place uncertainty of about 2 arises from the lack of precision in our knowledge of the atomic weight and Avogadro's constants.) When the density is measured by X-ray diffraction, it is important that the defect concentrations are small because the variation in defect concentrations at this level of accuracy can be large enough to have a significant effect on the density. In the case of *GaAs*, it is believed that the defect concentrations for near to stoichiometric crystals are negligible (3, 33, 34) and the X-ray diffraction density is approximately  $5.3163 \text{ g/cm}^3$  (34).

There are two direct measurements of density with a precision comparable to that determined by the X-ray diffraction. To compare values the directly measured density values were corrected to room temperature by using the preferred value of the expansion coefficient (35). The values of the density are  $5.3175 \text{ g/cm}^3$  found by Straumanis and Kim (3) and  $5.3160 \text{ g/cm}^3$  found by Yarmolyu *et al.* (36) who also show that the density does not change with dopant concentrations up to levels in excess of  $2 \times 10^{18} \text{ cm}^{-3}$ .

Bublik *et al.* (34) claim an order of magnitude greater precision and quote use of  $5.31584 \text{ g/cm}^3$  (gallium-rich samples) to  $5.31691 \text{ g/cm}^3$  (arsenic-rich samples) with a precision of about 2 in last digit at 300 K. In the absence of other data with similar precision, it is impossible to access the accuracy of these measurements. For most purposes, the density of *GaAs* can be assumed to be  $5.3165 \text{ g/cm}^3$  with an uncertainty of  $\pm 0.0015$  at 300 K. Using the evaluated thermal expansion data (35), Brice (37) deduced the density as a function of temperature. The density calculated by this method in the range of 0 to 1500 K (37) is listed in Table 1-2.

### 1.3 Growth Techniques for Semi-Insulating GaAs

The major difficulty in *GaAs* growth is that *GaAs* decomposes incongruently when heated. The vapor pressure of elemental arsenic at the melting temperature of *GaAs* (1238 °C) is approximately 1 atmosphere. If left unconstrained, *As* will vaporize from the melt, altering the melt composition and thus the point defect structure of the grown crystals. Another difficulty lies in the limitation of the choice of material for containers used in *GaAs* growth because both *Ga* and *As* are chemically active and interactions between these elements and container materials can cause the incorporation of impurities into the final crystals. In addition, *GaAs* has a relatively low resolved shear stress, which means that even a small stress during growth can produce extended defects. A majority of the stress present during growth arises from either the expansion of the crystal during the solidification and cooling period or the stress imposed on the crystal by the container walls.

Table 1-2. Temperature Dependence of *GaAs* Density (37)

Temperature (K)	Density (g/cm <sup>3</sup> )	Temperature (K)	Density (g/cm <sup>3</sup> )
0 - 100	5.322	800	5.269
150	5.329	900	5.259
200	5.326	1000	5.249
250	5.322	1100	5.239
300	5.316	1200	5.228
400	5.307	1300	5.217
500	5.298	1400	5.207
600	5.289	1500	5.196
700	5.279		

There are three principle methods of growing *GaAs* bulk crystals; liquid encapsulated Czochralski (LEC), horizontal Bridgman (HB), and vertical gradient freeze (VGF) methods. Each of the three methods has its own advantages and disadvantages, and the crystals from each process show distinct characteristics in electrical properties. The LEC method is the most popular technique due to its higher yield and higher purity. Though growth techniques have improved to the extent that wafers with 4 inch diameter are produced commercially, it is too early to reach a definitive conclusion about the best technique. Extensive research has focused on the improvement of these three growth techniques and on the development of new techniques.

The following sections will discuss each of three existing techniques in relation to the newly developed liquid encapsulated melt zone (LEMZ) technique. It should be noted that *GaAs* crystal growth still remains as much of a technical art as a science, and that the following discussion is only a general overview. Since each of the four methods of growth has its own numerous variations, only the generic approaches are described.

#### 1.3.1. Liquid Encapsulant Czochralski (LEC) Technique

The LEC method was adapted to *GaAs* crystal growth in 1965 (38) after this technique was pioneered by Metz *et al.* (39) to grow semiconductor materials with high vapor pressures. Figure 1-2 shows a typical schematic diagram of the LEC process (40). In the LEC technique, the *GaAs* melt is contained in a crucible and covered by an immiscible liquid  $B_2O_3$  layer which is backed by an overpressure of an

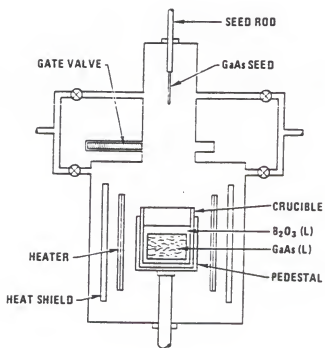


Figure 1-2. Schematic diagram of the LEC process (40).

inert gas. After the temperature of the melt stabilizes, a seed crystal with a desired crystallographic orientation penetrates the  $B_2O_3$  layer and contacts the melt. Growth is achieved by slowly withdrawing the seed from the melt. A typical growth rate is about 0.6 - 0.8 cm/hr. The seed and the crucible are usually rotated in opposite directions to eliminate azimuthal thermal gradients and to help the uniformity of dopant concentrations. The  $B_2O_3$  not only prevents the loss of arsenic from the melt but also provides a thin layer of liquid  $B_2O_3$  on both the surface of growing crystal (reduces thermal stress and thermal decomposition of solid  $GaAs$ ) and the melt (reduces dissolution of the container material by the melt).

Direct synthesis of gallium arsenide from the elements is the preferred method, because in-situ synthesis avoids possible contamination resulting from separate synthesis and the additional handling steps. In-situ synthesis can be achieved by either a high or low pressure process. In the high pressure process, pre-weighed gallium and arsenic are loaded in the crucible with  $B_2O_3$  (and possibly dopant) and the system is heated to approximately 800 °C in an inert gas at a pressure of 60 to 75 atm. At this condition, an exothermic reaction producing  $GaAs$  proceeds rapidly, resulting in a rapid increase in the temperature to about 1000 °C. The desired  $As/Ga$  ratio is obtained by loading excess arsenic in the initial charge because there will be a loss of  $As$  during the heating period until the solid  $B_2O_3$  becomes liquid and liquid  $B_2O_3$  covers the  $GaAs$  completely. There is no way to know the exact  $As/Ga$  ratio obtained in the melt during growth. The residual material in the crucible and the weight of the crystal after the run, however, can be used to

estimate the amount of arsenic lost (41). Low pressure synthesis (42-44) usually uses hot-wall technology to minimize arsenic loss during synthesis and is performed at a pressure of about 2 atm. The low pressure process has its own advantages over the high pressure process in the fact that arsenic loss during the heating process can be greatly reduced and that the low pressure LEC puller is smaller and less expensive. In the low pressure process,  $Ga$  is first heated to the melting temperature of  $GaAs$  with the  $B_2O_3(l)$  floating on top. Arsenic is then introduced into the crucible through a quartz tube in a controlled manner. This arsenic reacts immediately with the gallium until the melt is saturated with  $As$ . Since  $As$  is not present during the heating period and it reacts as soon as it is introduced into the crucible, the total arsenic loss in this low pressure synthesis method is usually less than 0.1 wt.%.

It is very difficult to monitor and control the diameter of the growing crystal because the  $B_2O_3$  encapsulant, which is typically 2 to 4 cm thick, complicates optical sensing of the diameter at the meniscus and further, thermal turbulence of the gas makes optical observation at high pressure difficult. Usually the diameter of the growing crystal is controlled by manipulating the pulling rate and heat transfer factors (e.g., heater power, crystal rotation rate). Sometimes a crystal weight sensor is used to deduce the crystal diameter during growth. The buoyant and surface effects of encapsulant influence this measurement. Computer control of the diameter has been achieved with the use of the crystal weight sensor method (45). Because gas turbulence is not a problem with the low pressure synthesis LEC, optical systems

(direct measurement of crystal diameter) have been investigated for the control of this process (46).

Either quartz ( $\text{SiO}_2$ ) or pyrolytic boron nitride (PBN) is used as a crucible material in the LEC process. The choice of crucible material is dependent on the required electrical properties of the crystals, though the high pressure synthesis LEC process uses the PBN crucible most exclusively and low pressure LEC uses both of the materials. When quartz is used as a crucible material, it can be difficult to grow undoped semi-insulating *GaAs* because silicon from the crucible incorporates into the crystal, resulting in n-type material. The incorporation rate of silicon in the LEC technique is, however, lower than that in the HB technique. It is believed that  $\text{B}_2\text{O}_3$  acts as a barrier for silicon transport into the *GaAs* melt, thus preventing silicon incorporation. In the case of a PBN crucible, there is little silicon incorporation in gallium arsenide, but boron incorporation occurs. However, since boron is an iso-electronic element in *GaAs*, it does not have any electrical activity in this material. When *GaAs* is grown in PBN crucible, a typical concentration of silicon in gallium arsenide is less than  $2 \times 10^{15}/\text{cm}^3$ . For PBN crucibles, carbon is present as the dominant impurity (acceptor), with concentrations in the range  $3$  to  $15 \times 10^{16}/\text{cm}^3$ . The presence of carbon in the *GaAs* is most likely from the graphite furnace parts with transport to the melt as  $\text{CO}$  and  $\text{CO}_2$ .

Large temperature gradients in the LEC method are the main source of the biggest problem in this technique. For example, the temperature gradient in the usually thin ( $2 - 4 \text{ cm}$ )  $\text{B}_2\text{O}_3$  layer is on the order of  $100 \text{ }^\circ\text{C}/\text{cm}$ . Even worse, this



large temperature gradient is near the growth interface (solid - melt interface) and introduces mechanical stress in the growing crystal. Gallium arsenide has a relatively low critical resolved shear stress compared to silicon, and if the stress due to temperature gradient exceeds the critical resolved shear stress, the grown material becomes heavily dislocated. LEC dislocation densities can easily be in the range  $10^4$  to  $10^5/\text{cm}^2$  for 2 inch or 3 inch material. It is typical that *GaAs* wafers shows a "W" pattern of dislocation density across any diameter (47). That is, the dislocation density is high in the center, lower in the annular space between the center and edge, then high again at the outside edge. The sheet resistance tends to follow the same pattern. Much effort has been expended to reduce both the axial and radial temperature gradient in the melt to a minimum, consequently lowering the dislocation density. One of these efforts uses a thick  $\text{B}_2\text{O}_3$  layer to reduce the thermal gradient and it is reported that the dislocation density can be reduced to  $5000/\text{cm}^2$  for 2 inch material (48).

### 1.3.2. Horizontal Bridgman Technique

In horizontal Bridgman (HB) growth, the starting material can be either pure *Ga* or poly-crystalline *GaAs*. The starting material is placed in a quartz boat with a seed crystal of the desired crystallographic orientation placed at the front of the quartz boat. The quartz boat containing *Ga* (or poly-crystalline *GaAs*) and elementary *As* are placed inside the quartz ampoule. This ampoule is evacuated and backfilled with inert gas before being sealed. A schematic of the HB growth apparatus is shown in figure 1-3 (49). The furnace is designed to control the

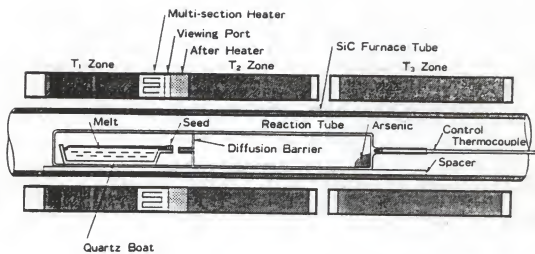


Figure 1-3. Schematic diagram of the HB process (49).

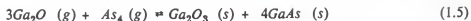
temperature gradient along the axial direction. The quartz boat, which contains the starting material, is placed in the region where the temperature is higher than the melting temperature of *GaAs*, and the seed crystal is in the region where the temperature is lower than the melting temperature of *GaAs*. Elemental *As* is placed in the other side of ampoule, where temperature is maintained at values such that the vapor pressure is close to that of *GaAs* at the melting temperature. During growth, the *As* source temperature is maintained at approximately 617 °C (the vapor pressure of pure *As* is about 1 atmosphere). This *As* pressure maintains stoichiometry of the *GaAs*. When pure *Ga* is used as a starting material, *As* vapor from the *As* source reacts with gallium to give a stoichiometric *GaAs* melt, similar to low pressure synthesis of *GaAs* in the LEC method.

Growth starts by moving either the furnace or the ampoule slowly so that the temperature front moves along the length of the boat. The furnace is normally tilted from horizontal to compensate for the thermal expansion of *GaAs* upon freezing, which would otherwise produce a constantly increasing crystal cross-sectional area. The yield of this technique is very low compared to the LEC process because crystals grown by the HB process have a D-shape cross section, matching the shape of the boat. Since device production processes require circular shaped wafers, D-shaped slices are not desirable. To make slices circular, a significant portion of the D-shaped slices have to be wasted, consequently lowering the yield. Of all the disadvantages, the asymmetrical thermal configuration poses the most significant problem inherent in this technique. As can be seen in figure 1-3, the boat is placed in the lower half

of the ampoule. The *GaAs* melt in the boat experiences a non-symmetric radial temperature gradient, which forces convection in the melt. This changes the shape of the interface between the *GaAs* melt and crystal, causing the interface shape to be concave in the growth direction. It is known that a non-planar interface has an effect on the propagation of defects in directional solidification (50). As in other crystal growth processes from the melt, a non-planar interface between the solid and melt phases is a major source of dopant concentration variations across the wafer diameter. A typical temperature gradient in the HB method is about  $10\text{ }^{\circ}\text{C}/\text{cm}$ , which is much smaller than that of the LEC method (about  $100\text{ }^{\circ}\text{C}/\text{cm}$ ). Consequently, crystals grown by the HB technique have a lower dislocation density (typically around  $5000\text{ cm}^{-2}$ ). In some cases, indium is added as a hardening element in *GaAs* growth to further reduce the dislocation density.

Silicon is the main impurity in HB material because the boat is made of quartz. The surface of the silica boat, which contacts the *GaAs* melt directly, is treated with a sandblast or HF etching to roughen the surface. This treatment helps to reduce the wetting problem and to eliminate subsequent sticking of the solid *GaAs* to the boat upon cooling (51-53). With this treatment, the *GaAs* crystal can be readily removed from the boat after growth. Typically, the concentration of silicon in HB grown *GaAs* ranges from 5 to  $10 \times 10^{16}/\text{cm}^3$  (53, 54). Though there is a possibility that some degree of silicon incorporation in the melt can occur through exposure of the ampoule walls to As vapor and subsequent vapor transport to the melt, silicon is incorporated mainly through the dissolution of the crucible (55). Possible reactions

include:



It has been reported that the presence of oxygen during growth decreases the incorporation of silicon into  $GaAs$  significantly. Martin *et al.* (56) found that when  $Ga_2O_3$  was added during growth, the concentration of silicon introduced into  $GaAs$  was at least 10 times lower than in a crystal grown without  $Ga_2O_3$ . In addition, Shikano and Kobayashi (57) added  $As_2O_3$  to the melt and found consistent results of low silicon incorporation into the gallium arsenide. It is believed that the decrease of silicon incorporation in the melt was caused by the decomposition of  $As_2O_3$  or  $Ga_2O_3$  to generate oxygen and subsequent reaction of silicon with oxygen to form  $SiO_2$  or  $SiO$ .

### 1.3.3. Vertical Gradient Freeze Method

There have been two reports (58, 59) of  $GaP$  crystals successfully grown by the vertical gradient freeze (VGF) method. Clemans *et al.* (60) reported improved  $GaP$  crystals grown by this method. The VGF method has, however, not been fully applied to gallium arsenide crystal growth. There are two main differences between the VGF and HB techniques. Firstly, the VGF method is a vertical configuration; growth occurs parallel to the gravity vector. Secondly, instead of moving the furnace or ampoule through a fixed temperature gradient to achieve directional solidification, all growth parts are stationary and the furnace temperature profile is varied

electronically, eliminating mechanical vibrations from moving parts. The crystal and melt are subject to a temperature gradient through the independent control of a number of closely spaced heater elements, linked with thermocouples situated along the growth axis.

The VGF method has several advantages over the HB and HGF (horizontal gradient freeze, which uses a horizontal configuration and gradient freeze) growth techniques. Solidification occurs in an axisymmetric fashion when power to the melt heater is reduced. The liquid-solid interface is in the horizontal plane as it advances vertically while the seed end cools. Very slow cooling is possible because the crucible defines the diameter and the cold-on-the bottom growth method is thermally stable with respect to convection. As in the HB method, melt decomposition is prevented by supplying a partial pressure of  $As$  from a separately heated  $As$  reservoir. The thermal profile of the crystal and melt is symmetric and the radial gradient can be maintained at low values so that a more planar interface can be achieved during growth. Also the container can be rotated to achieve thermal symmetry in the crystal and melt. Improvement of the thermal configuration has reduced the concentration of strain-generated dislocations and twins in  $GaP$  (60). The cold-on-the-bottom temperature profile reduces convection in the melt, decreasing impurity striations and inclusions in the crystal. In addition, since the shape of crystal grown by this method depends on the shape of the crucible (usually PBN), a crystal with a circular cross section can be grown and, furthermore, diameter control becomes much simpler. A crystal with a circular cross section prevents the loss of material significantly.

Abemathy *et al.* (61) reported growth of 2 inch *GaAs* crystals by the VGF method. Their results show that the etch pit density was much lower than that found in the standard LEC materials, presumably due to the low temperature gradient. The dislocation density at the seed end was  $2000\text{ cm}^{-2}$  and increased at the tail end to less than  $6000\text{ cm}^{-2}$ . The resistivities of wafers taken from the ingot were higher than  $10^7\text{ }\Omega\text{-cm}$  at the seed and the middle, making this material suitable for device processing. The resistivity, however, was lower at the tail.

#### 1.3.4. Liquid Encapsulated Melt Zone Method

The liquid encapsulated melt zone (LEMZ) technique is a new method for growth of III-V compound semiconductors. This technique was originally suggested by Pfann (62) as a way to avoid contamination of crystals from a container, to prevent a loss of a highly volatile element, and to permit a larger stable melt zone, thus producing larger crystals.

In 1.3.1-1.3.3 sections, the common techniques for *GaAs* crystal growth were reviewed. Though these are the most popular methods to produce *GaAs* crystals commercially, these techniques have one or more of the following problems (63) which need to be solved to achieve improved crystal quality:

1. Compositional variations along the growth axis, particularly for dopants.
2. Gravity induced deformation of the crystal and the melt surface.
3. Contamination of the crystal due to the interaction of the melt with its container.

4. Extended defect generation due to thermal stresses from the difference in the thermal expansion coefficients of the crystal and the container.
5. Vibration caused by motors used to move the liquid-solid interface.
6. Morphological instabilities and extended defects due to thermal gradients in the melt and solid.
7. Melt stoichiometry variations caused by incongruent evaporation.

It is believed that LEMZ process will address many of these problems. The LEMZ process is basically the floating zone (FZ) process (used for many years in the commercial production of *Si* bulk crystals) with the addition of a liquid encapsulant to prevent loss of elements by volatilization. This process is described in more detail later in this chapter, while the reasons for investigating this technique are given below.

The main advantage of this technique is that it is possible to eliminate the container effects. Unlike the LEC, HB and VGF processes (LEC process forms a very thin layer of encapsulant between the crucible and *GaAs* melt, while HB and VGF processes do not use an encapsulant) there is a thick layer of encapsulant separating the container and the *GaAs* solid and melt. Therefore, the molten gallium arsenide is only in contact with the liquid encapsulant, solid product, and precursor gallium arsenide. This eliminates the influence of the container which is a major source of elemental contamination in semiconductor growth. A solid that solidifies in contact with a container invariably suffers some strain due to the mismatch between the coefficients of thermal expansion of the two materials. This stress can



also be eliminated by a thick encapsulant layer, which prevents direct contact of the solid with the rigid wall as in HB and VGF process. In addition, vibration caused by motors used to move the liquid-solid interface can be minimized by using a small and light heating source. The stoichiometry control in this process is much easier than the HB process which uses a temperature sensitive As source. Another advantage is its ability to purify the crystal by repeated zone passes. Depending on their liquid-solid segregation coefficients, impurities either segregate into the liquid or remain in the precursor material during melt zone translation. As a result, the concentrations of impurities, whose segregation coefficients are less than 1, are very high at the end of the rod opposite to the seed crystal and the rest of the rod is very pure. It is possible to repeatedly process the same ingot, decreasing the impurity concentration with each pass.

Growth of low defect density gallium arsenide crystals in the microgravity environment using the floating zone (FZ) technique or newly developed LEMZ seems promising from both practical and theoretical points of view. Growth of bulk crystals in a microgravity environment can eliminate defects that are generated by the gravity induced fluid motions and even operate without the container (64). However, the common processes used for growing gallium arsenide crystal are not suitable for the microgravity conditions. For instance, in the popular LEC process, gravity is required to maintain a flat interface between the melt and boron oxide cover layer while the melt-crucible interface acts as a source of impurities. Encapsulated Bridgman growth, rarely used, has basically the same drawbacks. In addition, it

requires a solid container which can introduce thermal stresses and defects during cooling.

Floating zone refining, which is the basic process of LEMZ, has been utilized for many years to produce very high purity silicon crystals. In order for this method to be used in the modified LEMZ process for  $GaAs$  growth, several requirements must be met. The liquid-liquid surface tension between  $GaAs(l)$  and  $B_2O_3(l)$  is important in determining the shape of the molten zone. The Bond number is the critical dimensionless parameter that determine the shape of the zone and is defined as

$$L_B = \sqrt{\frac{\sigma}{\rho g}} \quad (1.6)$$

where  $\sigma$  is the surface tension,  $g$  is the gravitational constant, and  $\rho$  is the mass density of  $GaAs$  (65). Analysis shows that both the maximum length and width of the molten zone must be on the order of  $L_B$ . Therefore the bond number determines the diameter of the crystal that can be grown by the LEMZ method. It is obvious that the LEMZ method is not suitable for a material whose density is high relative to its surface tension. The practical limit on the diameter of LEMZ refined  $GaAs$  ingot grown on the earth is 8 - 10 mm. However, in a microgravity environment, there is no practical limit on the diameter since  $L_B$  is inversely proportional to the square root of  $g$  and practical values of  $g$  are on the order of  $10^{-4}g$ .

Previous attempts to grow crystals in a low gravity using a simple floating zone technique are limited in number. Eyer *et al.* (66) attempted to rapidly grow a

phosphorous doped silicon crystal during the six minute free fall of a Skylark sounding rocket. They also performed floating zone growth experiments on the European Spacelab I. The LEMZ process has not been attempted in low gravity, and apparently has been attempted only in normal gravity for the growth of *GaAs*. The schematic diagram of the LEMZ experimental apparatus is shown in figure 1-4. This process uses an encapsulant in the conventional floating zone process (62) to prevent the loss of *As* due to its high vapor pressure at operating temperature. The feed rod of poly-gallium arsenide is immersed vertically in the molten encapsulant and the melt zone is established at the bottom end of the feed rod by a resistance, inductive or optical heating method. The melt zone is moving along the feed rod to affect purification and establish the single crystal.

Johnson (67) attempted LEMZ growth of 8 - 15 mm *GaAs* on the earth. He used r.f. heating to achieve a melt zone with the aid of an auxiliary furnace. Single crystal *GaAs* as well as poly-crystalline *GaAs* feed rods were used, but resulting products were all poly-crystalline. Spark source mass spectrometry analysis of his samples showed that the concentrations of both boron and silicon increased from their initial values, but the concentrations of other impurities, which had the segregation coefficients less than 1, decreased, showing this process had a zone refining effect. Recently Swiggard (68) was able to grow single crystal gallium arsenide using the LEMZ method. In his experimental setup, a special furnace with a thermal spike was used to create a molten zone, and PBN was used as a crucible

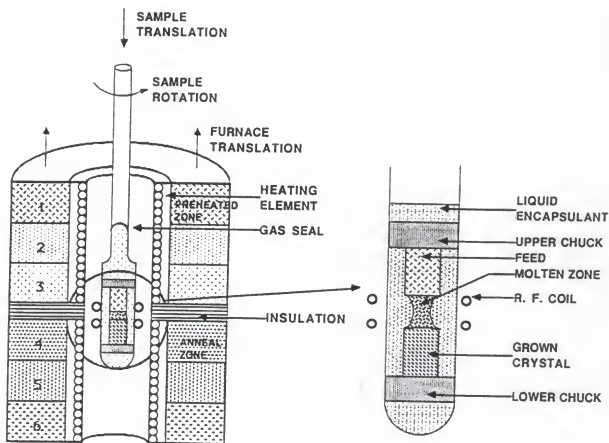


Figure 1-4. Schematic diagram of the LEMZ process.

material. The crystal was grown in the (100) direction and the resistivity was found to be  $5 \times 10^8 \Omega\text{-cm}$ . An etch pit density of  $2$  to  $5 \times 10^3 \text{ cm}^{-2}$  was the norm.

#### 1.4 Overview of Thesis

This thesis consists of three major subjects which are important in *GaAs* bulk crystal growth. As discussed in section 1.3, the encapsulant plays an important role in both LEC and LEMZ *GaAs* crystal growth. Encapsulant studies are important to understand its effect on crystals and to improve its thermophysical properties. Since the direct contact area between the solid and molten *GaAs*, encapsulant, and the crucible is much larger in the LEMZ process than that in the LEC process, the interaction between these materials becomes much more important. Furthermore, the thermophysical properties of the encapsulant need to be improved to take advantage of the LEMZ process in a low gravity environment. In chapter 2, such studies are presented. Several mixed oxides are studied as an alternative encapsulant, and these mixed oxides as well as the conventional  $B_2O_3$  encapsulant are investigated for chemical compatibility with *GaAs* crystal growth. In addition, attempts to measure the surface tension of encapsulant-molten *GaAs* systems are briefly described in Appendix 1.

As the semiconductor processing becomes more complex, accurate knowledge of the properties of these materials is essential. Many processes involve the liquid phase of *Ga-As* system (e.g., LPE (liquid phase epitaxy) and bulk crystal growth from the melt) and knowledge of the thermodynamic properties of this system is essential for the optimization of the operation. In chapter 3, measurement of the activity of

*Ga* in liquid *GaAs* along the liquidus line using a solid electrolyte is described. In addition, the results of this experimental measurement were included in an optimization calculation along with data in the literature. A new optimized set of coefficients for the excess Gibbs energy of liquid and solid *GaAs* were also obtained from this optimization calculation.

Silicon is the major impurity in *GaAs* grown in a quartz crucible. It is difficult to grow semi-insulating *GaAs* crystals if incorporation of silicon occurs to a significant extent during growth. Since silicon is an amphoteric dopant in *GaAs* it is very important to predict which lattice site will be occupied in the *GaAs* lattice (*Ga* or *As* site). In chapter 4, a thermochemical model is developed to understand incorporation of silicon during *GaAs* melt growth and the behavior of silicon in *GaAs* crystals. This model is used to predict the concentration of silicon incorporated in *GaAs* as a function of the amount of silicon in *GaAs* melt as well as segregation coefficient and compensation ratio of silicon.

Chapter 5 consists of summary and recommendations. Conclusions of each chapter are briefly discussed and summarized in this chapter. In addition recommendations for future work are addressed.

## CHAPTER 2

### CHEMISTRY OF INTERACTION BETWEEN GaAs, ENCAPSULANT, AND THE QUARTZ CRUCIBLE

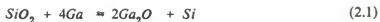
#### 2.1 Introduction

Boron oxide ( $B_2O_3$ ) has been used exclusively as the encapsulant in the growth of crystals which have a high vapor pressure at processing temperature. For instance, in LEC growth of gallium arsenide, the GaAs melt is covered with liquid boron oxide and backed by an over pressure of inert gas. The major roles of boron oxide in gallium arsenide crystal growth are a prevention of arsenic loss due to the incongruent vaporization of the gallium arsenide melt, formation of a diffusion barrier to the transport of impurities from the crucible into the gallium arsenide melt, and protection of the crystal surface from a loss of volatile arsenic. In addition, it was reported that boron oxide provided a purification of gallium arsenide because of its "gettering" action for many impurities (*e.g.*, Al, Ca, Cu, and Si) (69). As discussed in the chapter 1, gallium arsenide grown by the LEC technique using a quartz crucible has a lower concentration of silicon than that grown by the HB technique when a quartz boat is also used as the melt container. It is believed that in the LEC technique the liquid boron oxide wets the quartz crucible and forms a thin layer which separates the gallium arsenide melt from the quartz crucible. This barrier film reduces the incorporation rate of silicon into gallium arsenide. The

transport of silicon from the quartz crucible to the melt is accomplished by the partial dissolution of  $\text{SiO}_2$  into boron oxide at processing temperature.

Other studies (70, 71) show that the water content in the starting boron oxide encapsulant has a significant influence on the incorporation of silicon and boron impurities into gallium arsenide crystals. These studies found that boron oxide with a high water content ( $> 1000 \text{ ppm } \text{H}_2\text{O}$ ) yielded gallium arsenide crystals with low concentrations of silicon and boron, while boron oxide with a low water content ( $< 500 \text{ ppm } \text{H}_2\text{O}$ ) produced gallium arsenide crystals with high concentrations of silicon and boron. These results indicate that the incorporation of silicon and boron from the quartz crucible and boron oxide encapsulant, respectively, is a strong function of water content in the boron oxide encapsulant. Oliver *et al.* (72) were able to grow high purity, undoped gallium arsenide crystals from a quartz crucible using boron oxide with a high water content to suppress silicon contamination. It was, however, reported that the higher water content in boron oxide caused a deviation of the melt composition by the preferential removal of gallium from the melt, leading an arsenic-rich melt. This resulted in the generation of twins due to growth from a non-stoichiometric melt. The chemical kinetics controlling the incorporation of silicon and boron during crystal growth in a quartz crucible is not completely clear. It has been suggested (72) that introduction of silicon and boron into the melt derive from the chemical reduction of quartz crucible and boron oxide encapsulant in the presence of metallic gallium to produce  $\text{Ga}_2\text{O}$  according to following reactions:





However, these reactions are not able to explain the incorporation of silicon and boron in gallium arsenide as a function of water content in the boron oxide encapsulant. In the first part of this chapter, a study of the dissolution kinetics of gallium, arsenic and silicon in liquid boron oxide as a function of water content in encapsulant that is in contact with a gallium arsenide melt and quartz will be discussed. In the last part of this chapter, alternative encapsulant materials for gallium arsenide crystal growth will be discussed. The main purpose of this later study was to develop new encapsulant materials to improve the thermophysical properties of the encapsulant that are important in the LEMZ technique.

## 2.2 Interaction of $\text{B}_2\text{O}_3$ with the GaAs Melt and the $\text{SiO}_2$ Crucible During Bulk Crystal Growth

### 2.2.1. Experimental Description

Gallium arsenide crystals were grown by the vertical Bridgman growth technique using a quartz ampoule as a container. Grown gallium arsenide crystals were 1 cm in diameter and about 2-3 cm in length. Unlike the conventional vertical Bridgman growth, which uses a separate source of arsenic to maintain the melt's stoichiometry, a boron oxide encapsulant and an overpressure of inert gas (about 1.3 atm at growth temperature) were adopted to prevent arsenic loss from the melt. A

schematic of the apparatus is shown in figure 2-1. The furnace consists of two separate heating zones, and the temperature of each zone is controlled by a process controller, Micristar Model 828D. In addition, four shunts in each zone provide flexibility in achieving a desired temperature profile along the axial direction. During growth, the ampoule inside the furnace could be observed through two view ports installed 180° apart in the upper zone. Type S thermocouples (Platinum vs. Platinum-10% Rhodium) were installed in each zone to provide input to the process controller. Additional type S thermocouples were placed inside the chamber of furnace to monitor the growth temperature. Each thermocouple was calibrated against a NBS standard type S thermocouple. A desired temperature profile in the furnace was achieved by controlling power input to the furnace and adjusting the resistance of the shunt wires.

The crucible was made of quartz with a 1 cm inside diameter and 2 mm thickness. The bottom end of quartz ampoule was tapered to utilize the first gallium arsenide crystal solidifying at the tip of the tapered end as a seed for the rest of the growth. The quartz ampoule containing the gallium arsenide and encapsulant traveled along the axial temperature gradient in the furnace at a speed of 10 cm/hr. Grown crystals were polycrystalline mainly due to the high speed of travel.

It is well known that the gallium arsenide melt wets the quartz well and this wetting causes problems after crystal growth such as generation of dislocations and fracture of the crystal and the crucible. When the melt wets the quartz crucible, it

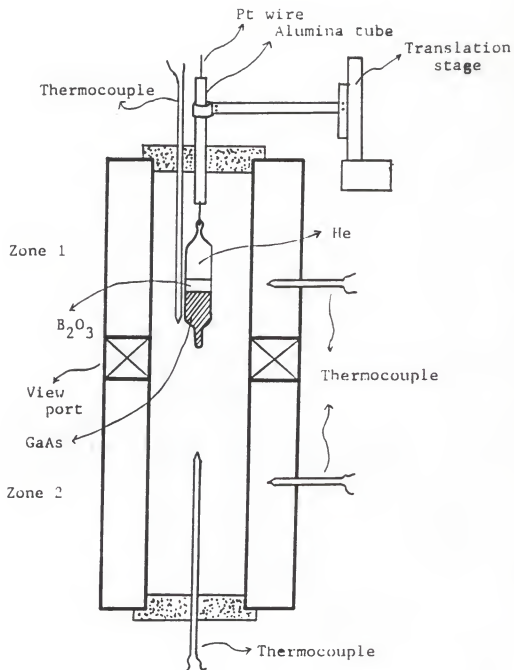


Figure 2-1. A schematic of the vertical Bridgman growth apparatus.

generates stress during cooling due to the mismatch of thermal expansion coefficients between gallium arsenide and quartz.

Three different preparations of the quartz ampoule were investigated in an attempt to prevent the wetting problem. The quartz ampoule was either sandblasted, etched with a  $HF$  solution, or scratched severely with  $10\ \mu m$  silicon carbide powder. After these treatments, the quartz ampoule was cleaned by the following procedure: *aqua regia* ( $HCl : HNO_3 = 3 : 1$ ), TCE (tetrachloroethylene), acetone, methanol, and finally DI water. Repeated experiments showed that scratching the quartz ampoule with silicon carbide powder was the best method to prevent the gallium arsenide melt from wetting the quartz ampoule. With this treatment, it was possible to grow gallium arsenide crystals without a fracture when no encapsulant was used. When an encapsulant was used, however, the gallium arsenide and the quartz ampoule still cracked a little, particularly at the tapered end. It was believed that the thin layer of encapsulant between the gallium arsenide and quartz ampoule caused the fracture during cooling due to the mismatch of thermal expansion coefficients between the three materials.

Approximately 7 g of gallium arsenide and 2 g of boron oxide were loaded in the quartz ampoule. The quartz ampoule was then evacuated, refilled with inert gas ( $Ar$  or  $N_2$ ) at about 0.3 atm, and finally sealed. At processing temperature ( $1250^\circ C$ ), the pressure of inert gas was over 1 atm. The inert gas served as an overpressure on the encapsulant to prevent arsenic bubbling through the protective encapsulant layer. Boron oxide with various water contents (nominally 100, 500, 1000, 1500, and 2000

ppm of water) was purchased from the Eagle-Picher Research Laboratory, Redwood City, CA. It was reported from the vendor that the water content in boron oxide was determined by infrared spectroscopy, in which the OH content was accessed from a thin film of boron oxide. Boron oxide was stored and prepared for experiment in a controlled atmosphere glove box equipped with a circulation pump and a moisture trap. Impurity analysis of the purchased boron oxide is shown in table 2-1. Grade "AA" undoped polycrystalline gallium arsenide was purchased from Morgan Semiconductor Division, Garland, TX, and was used as the raw material. This gallium arsenide was grown by the LEC technique with a reported carrier concentration of  $5 \times 10^{13}/\text{cm}$  (as supplied from the vendor). An impurity analysis of the grade "AA" gallium arsenide is shown in table 2-2.

After the temperature of the furnace was stabilized, growth proceeded from the bottom of ampoule as the crucible was lowered through the temperature gradient. The cooling process followed the growth and its schedule is shown in figure 2-2. Three different cooling rates,  $G_2 = 15^\circ\text{C/hr}$ ,  $G_3 = 40^\circ\text{C/hr}$ , and  $G_4 = 20^\circ\text{C/hr}$  were applied in this sequence. These cooling rates are much slower than the usual cooling rate of  $100^\circ\text{C/hr}$  in conventional Bridgman growth. Slow cooling rates were applied to reduce the thermal shock present during cooling since an encapsulant, which is not present in normal horizontal Bridgman growth, was used.

The grown gallium arsenide crystal and encapsulant were analyzed by several techniques. The quartz ampoule containing the gallium arsenide and encapsulant was cut radially in the middle and the cross section was polished for electron microprobe

Table 2-1. Impurities in the Starting  $B_2O_3$ \*

Element	Concentration ( $cm^{-3}$ )	Element	Concentration ( $cm^{-3}$ )
<i>Si</i>	$2 \times 10^{13}$	<i>Cr</i>	$0.2 \times 10^{13}$
<i>Al</i>	$1 \times 10^{13}$	<i>Ni</i>	$0.2 \times 10^{13}$
<i>Fe</i>	$0.5 \times 10^{13}$	<i>Mn</i>	$0.2 \times 10^{13}$
<i>Pb</i>	$0.05 \times 10^{13}$	<i>Mg</i>	$0.8 \times 10^{13}$
<i>Cu</i>	$0.05 \times 10^{13}$	<i>Ca</i>	$1 \times 10^{13}$
<i>Zn</i>	$0.1 \times 10^{13}$	<i>Na</i>	$1 \times 10^{13}$

- \*. Impurity concentrations were determined by emission spectrography and flameless atomic absorption analysis performed by Eagle-Picher Research Laboratory. Concentrations were reported in *ppm* by the vendor and converted in # atoms/ $cm^{-3}$  in this table.

Table 2-2. Impurity Analysis of GaAs by SIMS\* ( $cm^{-3}$ )

Cesium			Oxygen		
	Front	Tail		Front	Tail
<i>C</i>	$7 \times 10^{15}$	$7 \times 10^{15}$	<i>B</i>	$2 \times 10^{16}$	$2 \times 10^{16}$
<i>O</i>	$5 \times 10^{16}$	$5 \times 10^{16}$	<i>Mg</i>	$2 \times 10^{14}$	$4 \times 10^{14}$
<i>Si</i>	$3 \times 10^{14}$	$3 \times 10^{14}$	<i>Cr</i>	$0.2 \times 10^{13}$	$0.4 \times 10^{13}$
<i>S</i>	$3 \times 10^{14}$	$3 \times 10^{14}$	<i>Mn</i>	$1 \times 10^{14}$	$1 \times 10^{14}$
<i>Se</i>	$0.8 \times 10^{14}$	$0.8 \times 10^{14}$	<i>Fe</i>	$0.6 \times 10^{14}$	$0.7 \times 10^{14}$
<i>Te</i>	$4 \times 10^{13}$	$6 \times 10^{13}$	<i>Zn</i>	$1 \times 10^{16}$	$1 \times 10^{16}$
<i>Cu</i>	$6 \times 10^{15}$	$5 \times 10^{15}$			

\*. This data was supplied by Morgan Semiconductor Division.

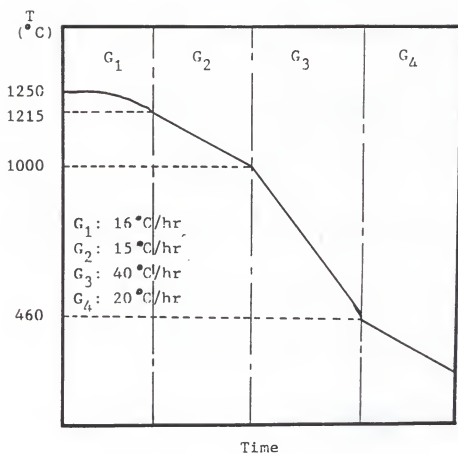


Figure 2-2. Cooling schedule for the vertical Bridgman growth.



and optical microscope analysis. The polishing procedure was as follows: samples were ground using 240, 320, 400, and 600 grit silicon carbide grinding paper and then polished with 5.0, 1.0, 0.3, and 0.5  $\mu\text{m}$   $\text{Al}_2\text{O}_3$  polishing powder. Polishing the samples was extremely difficult because the boron oxide was soluble in water, which forced the sample to be polished without a lubricant. If a lubricant which contained water was used, the thin layer of encapsulant between gallium arsenide crystal and the quartz ampoule was dislodged and caused the surface to be too rough for analysis.

The encapsulant sample taken along the gallium arsenide crystal was analyzed by Inductively Coupled Argon Plasma Emission Spectroscopy (ICP) to measure the amount of gallium, arsenic, and silicon. Calibration of the ICP method was accomplished with a standard solution for each element. The standard solutions were made by dissolving pure gallium arsenide and silicon into a solvent ( $\text{HF} : \text{HCl} : \text{HNO}_3 : \text{DI water}$  in the ratios 6 : 3 : 1 : 40). At least six different concentrations of standard solution were prepared for each element (from 0.01  $\text{ppmw}$  to 500  $\text{ppmw}$ ). With these standard solutions, the calibration curves were obtained and the analysis of the samples and calibration procedure were fully computerized. The concentration of each element in a blank solution (pure solvent) was automatically subtracted from the standard solution. The encapsulant samples were dissolved in the solvent used for the standard solutions. Since ICP gives the concentrations of elements in the liquid solution, data obtained were converted to the concentrations of elements in the solid encapsulant form the known amount of initial encapsulant. During the preparation of samples and standard solutions, it is very important not to use

glassware because of possible Si contamination. In our preparation, teflon and polypropylene containers were used.

Gallium arsenide crystals taken from the middle of the ingots were analyzed by SIMS and Hall measurement. The gallium arsenide was cut in a square shape ( $0.5 \times 0.5 \text{ cm}$  with  $0.05 \text{ cm}$  thickness) and polished mechanically by the same procedure used to polish the cross section of the quartz ampoule. In addition to mechanical polishing, chemical etching was also applied. Gallium arsenide samples were etched with a solution ( $\text{H}_2\text{SO}_4 : \text{H}_2\text{O} : \text{H}_2\text{O}_2$  in the ratios  $7 : 1 : 1$ ) for 6-10 minutes with gentle agitation. After etching, the samples were degreased using TCE, acetone, methanol, and DI water in an ultrasonic bath for 5 minutes in each solution. The contacts for Hall measurement (Van der Pauw method) were made by contacting indium dots at the periphery of the sample. The contacted samples were annealed at  $350^\circ\text{C}$  for 3 minutes in an alloying station with forming gas ( $\text{H}_2 : 9.3\%$  and  $\text{N}_2 : 92.7\%$ ) flowing. Though Hall equipments are capable of measuring the high resistivity samples, the Hall measurements were not successful because the silicon incorporation in gallium arsenide was inhomogeneous, resulting in unstable Hall voltages during measurement. The estimated resistivities of samples were higher than  $1 \times 10^6 \Omega\text{-cm}$ .

### 2.2.2. Results and Discussion

Analysis of the Encapsulant and GaAs. It was not easy to separate the gallium arsenide crystal from the quartz ampoule after growth because a thin layer of boron oxide glued the gallium arsenide to the quartz. The gallium arsenide was

retrieved from the quartz ampoule by dissolving the quartz ampoule and boron oxide layer in a  $HF$  solution. A typical crystal of gallium arsenide grown with the boron oxide encapsulant by the vertical Bridgman technique is shown in figure 2-3. The bottom tip of the crystal was cleaved during the retrieval process. The surface of crystal was shiny but rough on a macroscopic scale. It was believed that this irregular surface was an impression of the interface between gallium arsenide and the thin layer of boron oxide.

The optical micrographs of the polished cross sections revealed that the thickness of boron oxide layer between gallium arsenide and the quartz ampoule was about  $50 \pm 10 \mu m$ . This layer probably formed during the heating period because its thickness should have been  $16 \mu m$  if the boron oxide had flowed into the gap which was produced by the contraction of gallium arsenide during cooling period. For this calculation, equation  $\alpha_V = (1/V)(\partial V/\partial T)_P$ , where  $\alpha_V$  is the coefficient of volume expansion and  $V$  is the volume of solid, is integrated from the melting temperature of  $GaAs$  to that of boron oxide. For  $GaAs$ , equation (1.1) was used for the value of  $\alpha$  since  $\alpha_V = 3\alpha$ . The  $\alpha$  for  $Si$  was assumed to be constant, which is  $5.5 \times 10^{-7}/K$ . The optical micrograph of the quartz ampoule, encapsulant layer, and gallium arsenide crystal is shown in figure 2-4. This photograph also reveals that the interface between quartz ampoule and encapsulant is very rough. The roughness of this interface was too severe to be caused by scratching with  $10 \mu m SiC$  powder. Therefore it was suggested that the quartz ampoule and boron oxide reacted each other.



Figure 2-3. A typical *GaAs* polycrystal grown with boron oxide by vertical Bridgman growth.



Figure 2-4. Optical micrograph of the boron oxide layer (dark region) between *GaAs* (bright region) and quartz crucible (upper region). Magnification; 500x.

Processed (*i.e.*, grown with gallium arsenide) and starting boron oxide were analyzed by differential scanning calorimetry (DSC) analysis. The heat flow is plotted as a function of temperature in figures 2-5 and 2-6. The reference material was sapphire. The analysis of the starting boron oxide shows a glass transition temperature near 290 °C and melting temperature around 400 °C. The first two peaks around 110 °C and 150 °C are considered to be a result of evaporation of surface and bulk water, respectively (figure 2-5). On the other hand, the analysis of processed boron oxide shows neither glass transition nor the melting phenomena (figure 2-6). It is not clear but it seems that the thermal properties of boron oxide were changed by the dissolution of silicon from quartz ampoule into boron oxide during growth.

Electron microprobe analysis (EMPA) along with SEM micrographs was applied to the polished boron oxide layer, and the results are shown in figures 2-7 and 2-8. In figure 2-7(a) the bright white region is gallium arsenide, boron oxide is the middle region and the quartz is the gray area on the bottom side. The white line crossing the middle of picture is the scanning line of the electron microprobe. The y-axis of EMPA analysis represents the intensity of element detected. The sensitivity of EMPA is 0.1 wt %. Figure 2-7(b) shows that boron oxide is rich in gallium, arsenic and silicon, and that the concentration of these elements is not uniform. Figure 2-8 reveals that there are white precipitates in the boron oxide layer which are rich in gallium (probably  $Ga_2O_3$ ). It is obvious from the EMPA results that the boron oxide

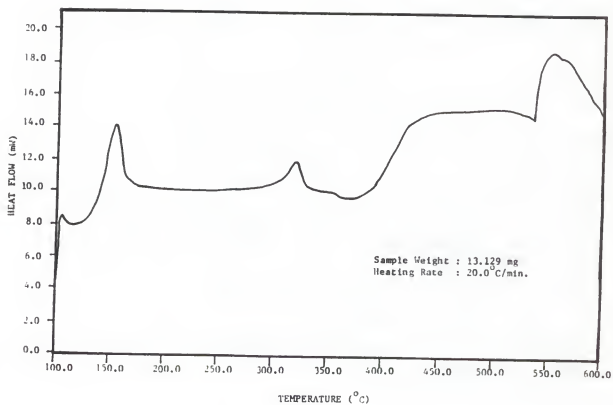


Figure 2-5. The differential scanning calorimetry (DSC) analysis of pure boron oxide.

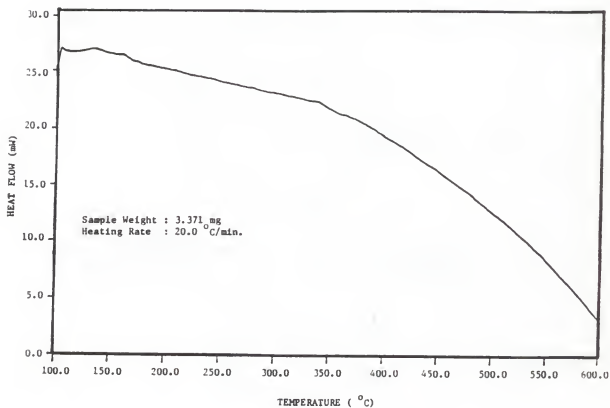
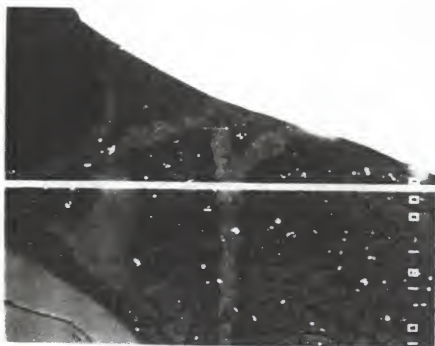
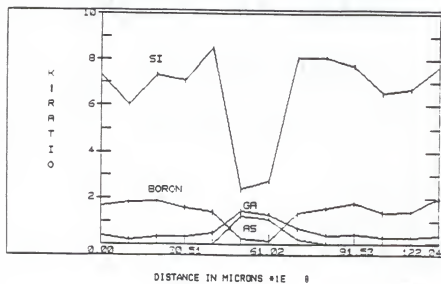


Figure 2-6. The differential scanning calorimetry (DSC) analysis of the processed (grown with *GaAs*) boron oxide.



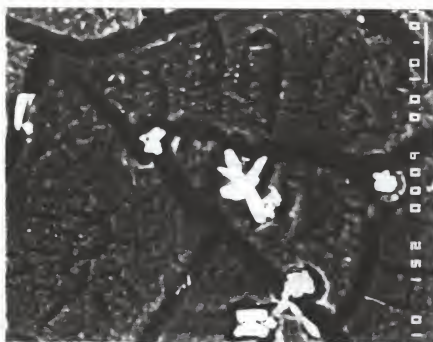


(a)

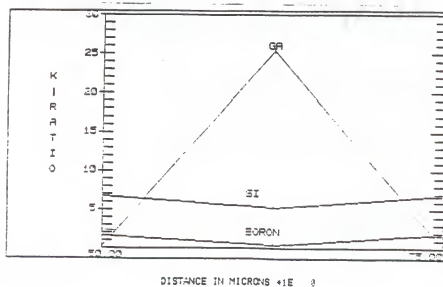


(b)

Figure 2-7. Microprobe line scan across "reacted band" in boron oxide encapsulant.  
 (a) SEM photo, magnification; 1000x (b) EMPA.



(a)



(b)

Figure 2-8. Microprobe analysis of precipitates in boron oxide encapsulant. (a) SEM photo, magnification; 5000x (b) EMPA.

not only dissolves the quartz ampoule but also removes gallium and arsenic from gallium arsenide melt.

For quantitative analysis, ICP was used to determine the concentrations of silicon, gallium and arsenic in the encapsulant while SIMS analysis was used to measure impurities in the grown gallium arsenide. The ICP results show that the uptake of silicon by boron oxide is dependent on contact time, but not on water content in the encapsulant. The behavior of gallium uptake is opposite to that found with silicon. Figures 2-9 and 2-10 show the silicon and gallium uptake as a function of the encapsulant water content. The time dependence of the silicon and gallium uptake is shown in figure 2-11. The results shows that the amount of gallium in the encapsulant after equilibration for one hour was significant and depended on the initial water content in the boron oxide. A higher water content in the encapsulant produced a higher concentration of gallium in the encapsulant. The gallium uptake was found not to depend on contact time, suggesting true equilibrium was reached. Similar studies were performed on the arsenic uptake, though the uptake level was too low to be detected accurately by ICP (detection limit for *As* is 0.1 ppm).

The incorporation level of several impurities in grown gallium arsenide was determined by SIMS analysis. *GaAs* samples were taken from the middle of the grown crystals and the results are listed in table 2-3. The main impurities in gallium arsenide were silicon and boron, and the concentrations of these impurities were dependent on the water content in starting boron oxide. A higher water content in the encapsulant suppresses the incorporation of silicon and boron in gallium arsenide.

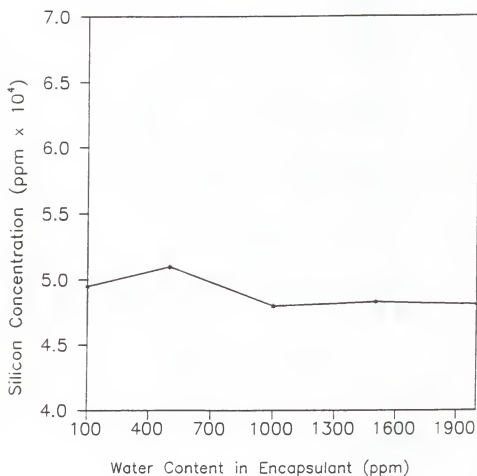


Figure 2-9. Silicon concentration in boron oxide as a function of boron oxide water content for contact at 1250 °C and 60 minutes.

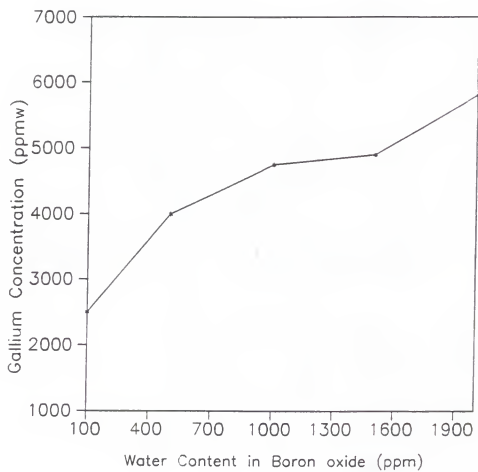


Figure 2-10. Gallium concentration in boron oxide as a function of boron oxide water content for contact at 1250 °C and 60 minutes.

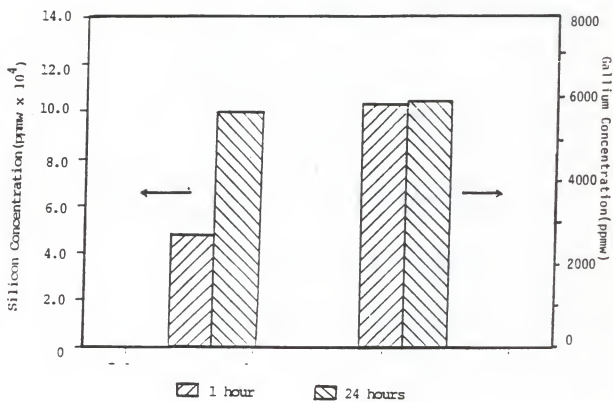


Figure 2-11. Silicon and gallium concentration in boron oxide as a function of contact time at 1250 °C.

Table 2-3. SIMS Analysis of GaAs\*

	GaAs Grown with			
	No Encapsulant	$B_2O_3$ (2000 ppm)**	$B_2O_3$ (100 ppm)	$B_2O_3+Ga_2O_3$ (100 ppm)
Si	$5 \times 10^{16}$	$\leq 5 \times 10^{14}$	$3 \times 10^{15}$	$\leq 6 \times 10^{14}$
B	$4 \times 10^{15}$	$2 \times 10^{14}$	$2 \times 10^{16}$	$9 \times 10^{15}$
O	$\leq 2 \times 10^{16}$	$\leq 6 \times 10^{16}$	$\leq 3 \times 10^{16}$	$2 \times 10^{20***}$
Cr	$8 \times 10^{15}$	$4 \times 10^{13}$	$2 \times 10^{13}$	$2 \times 10^{13}$
Fe	$2 \times 10^{15}$	$2 \times 10^{15}$	$6 \times 10^{14}$	$1 \times 10^{15}$
Mn	$4 \times 10^{14}$	$4 \times 10^{14}$	$3 \times 10^{14}$	$2 \times 10^{14}$
S	$3 \times 10^{15}$	$3 \times 10^{15}$	$1 \times 10^{16}$	$6 \times 10^{16}$
P	$1 \times 10^{16}$	$1 \times 10^{16}$	$3 \times 10^{15}$	$\leq 3 \times 10^{14}$
Se	$\leq 6 \times 10^{12}$	$\leq 6 \times 10^{12}$	$\leq 1 \times 10^{13}$	$2 \times 10^{13}$
Na	$\leq 1 \times 10^{14}$	$\leq 1 \times 10^{14}$	$\leq 1 \times 10^{14}$	$\leq 8 \times 10^{13}$
Mg	$4 \times 10^{13}$	$4 \times 10^{13}$	$2 \times 10^{14}$	$\leq 2 \times 10^{13}$
Be	$\leq 4 \times 10^{13}$	$\leq 4 \times 10^{13}$	$\leq 3 \times 10^{13}$	$\leq 5 \times 10^{13}$
C	$\leq 1 \times 10^{16}$	$\leq 1 \times 10^{16}$	$3 \times 10^{16}$	$\leq 4 \times 10^{15}$
H	$8 \times 10^{16}$	$8 \times 10^{16}$	$\leq 5 \times 10^{16}$	$\leq 3 \times 10^{16}$

\*. SIMS analysis was performed by Charles Evans & Assoc..

\*\*. Water concentration in encapsulant.

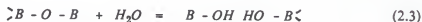
\*\*\*. The high concentration is due to poor sample quality.

Impurity concentrations in atoms/cm<sup>3</sup>.

SIMS analysis results of gallium arsenide grown without the presence of boron oxide are also listed in table 2-3. The concentrations of most impurities (except boron and oxygen) were less in gallium arsenide grown with the encapsulant than in gallium arsenide grown without the encapsulant. Thus the encapsulant has a beneficial gettering effect. The boron concentration in gallium arsenide grown with 100 ppm water content  $B_2O_3$  was higher than that grown without boron oxide. The source of boron is thus obviously the encapsulant.

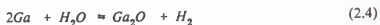
Chemistry of Ga Uptake and Incorporation of Si and B. It is obvious from our results and those of previous studies (72, 73) that the water content in boron oxide has a strong influence on the structural and electrical properties of gallium arsenide. Water in boron oxide is very difficult to remove, especially when the concentration is less than 500 ppm. Several researchers have proposed different drying process for boron oxide and the subsequent measurement of the water content (74-79). A typical drying procedure is to maintain the boron oxide at 1250 °C for one week in a vacuum furnace and then bubble  $N_2$  through the melt until the desired concentration is achieved (75).

In his study of infrared absorption due to water in the glass, Adams (77) found that in pure boron oxide glass,  $OH$  fundamentals occurred at 2.79 micron together with a sharp overtone at 1.4 micron. It was thus confirmed that water held internally in the glass is unassociated or, at most, only weakly associated. The solution of water in boron oxide can then be represented formally;





Since the gallium uptake is dependent on the water content in boron oxide, two mechanisms for the water-gallium reaction seem plausible;



These possible mechanisms imply that the water in boron oxide reacts with gallium in the melt to produce  $Ga_2O$  or  $Ga_2O_3$ , and that the amount of gallium dissolved in boron oxide is dependent on the amount of water in the boron oxide. To determine which, if either, mechanism is correct, the loss of gallium from the melt during growth was studied. The amount of gallium loss from the melt as determined by experiment was compared to the theoretical amount of gallium loss calculated stoichiometrically from equations (2.4) and (2.5). In every growth, several chunks of deposits were observed at the top of the quartz ampoule. Analysis by ICP showed that these deposits consisted of 20% gallium and 80% arsenic by weight. The total loss of gallium from the melt, therefore, is the sum of the gallium in the encapsulant (see figure 2-10) and the gallium in the deposits. In figure 2-12, the dotted line (line b) represents the total loss of gallium from the melt as a function of water content in boron oxide. The two straight lines, (a) and (d), represent the theoretical values of gallium loss based on the stoichiometry of reactions (2.4) and (2.5), respectively.

The solubility of gallium with zero water content in boron oxide was found to be 2000 ppmw by extrapolating the experimental data to zero water content (in figure 2-12). This solubility was confirmed experimentally by growing gallium arsenide with

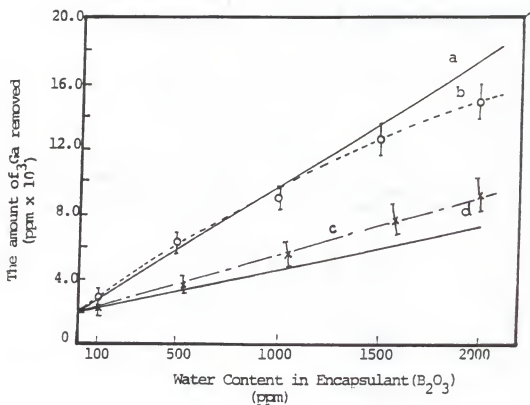


Figure 2-12. Comparison of experimental data with two possible mechanisms for Ga oxidation by water in the encapsulant. (The y-axis represents the concentration of Ga in  $B_2O_3$  assuming all Ga remain in  $B_2O_3$ .)

- (a)  $2Ga + H_2O = Ga_2O + H_2$
- (b) Total Ga in  $B_2O_3$  and deposit
- (c) Total Ga in  $B_2O_3$
- (d)  $2Ga + 3H_2O = Ga_2O_3 + 3H_2$

aluminum added to the boron oxide. Since the Gibbs energy of formation of  $Al_2O_3$  is much more negative at growth temperature than that of gallium oxide, most of the water in the boron oxide would be consumed to produce  $Al_2O_3$  instead of gallium oxide, simulating the true solubility of gallium at zero water content. After growth with the addition of aluminum, the boron oxide was analyzed by ICP and the concentration of gallium was around 2100 ppm, independent of the water content in boron oxide. This result is consistent with the result from extrapolation.

Figure 2-12 shows that the experimental data fits reaction (2.4) very well up to 1500 ppm. It seems at high water contents that the water in the boron oxide may show non-ideal behavior. Based on this study, formation of  $Ga_2O$  by the reaction of gallium with water (*i.e.*, by equation (2.4)) seems to give a stoichiometry consistent with the observed removal of gallium from the melt as the water content of the encapsulant increases. The amount of gallium removed is not dependent on the processing time and it can be explained by the fact that after all the water in encapsulant is depleted by reaction (2.4), no more gallium is removed from the melt.

Our SIMS analysis, as well as those of previous studies (72, 73), show a dependence of the silicon and boron incorporation in gallium arsenide on the water content in encapsulant (see table 2-3). It was also reported (80) that a small amount of  $Ga_2O_3$  added to the gallium arsenide melt in Bridgman growth with a quartz boat could suppress the incorporation of silicon in gallium arsenide. Gallium arsenide was grown with added  $Ga_2O_3$  to the boron oxide and the crystal was found to contain less silicon and boron (see table 2-3). These facts suggest that the high water content in

the boron oxide produces more  $Ga_2O$  by reaction (2.4), and this excess  $Ga_2O$  drives reactions (2.1) and (2.2) to the left. Therefore, the incorporation of silicon and boron is reduced. The high incorporation of silicon and boron with lower water content in encapsulant can be explained by the same reasoning.

### 2.2.3. Conclusions

This study included an examination of gallium, arsenic, and silicon uptake in the encapsulant  $B_2O_3$  and impurity incorporation in gallium arsenide during crystal growth. The results show that silicon contamination of gallium arsenide originates from the dissolution of the quartz crucible by the boron oxide encapsulant, while the boron oxide is the source of boron incorporation in gallium arsenide crystals. Silicon dissolution in the  $B_2O_3$  is dependent on processing time, but not on water content in the encapsulant, while the amount of gallium removed from the gallium arsenide melt is dependent on the water content in the encapsulant, but not on the processing time. A base solubility of gallium in boron oxide was found to be approximately 2000 ppmw. It was found that the higher water content in the encapsulant removes more gallium than arsenic from the melt, changing the melt stoichiometry. This explains the dependence of silicon and boron concentration in gallium arsenide.

## 2.3 Development of Alternative Encapsulants for the LEMZ Technique

In this section, the chemical compatibility of several alternative encapsulants for use in the LEMZ technique will be discussed. As mentioned in section 1.3.4., the thermophysical properties of the current encapsulant, boron oxide, could be improved

to successfully operate this technique in space. To vary these properties, several mixed oxides were selected as possible alternative encapsulants and tested for chemical compatibility with *GaAs* by growing gallium arsenide crystals in the presence of the mixed oxide encapsulants. The mixed oxides which pass the chemical compatibility test should then be subjected to measurement of thermophysical properties (e.g., surface tension, thermal conductivity, and viscosity) to determine if any improvement in the LEMZ process is possible. An attempt to measure the surface tension between the encapsulant and *GaAs* melt was made. Unfortunately these experiments were not successful because of experimental difficulties. However, because the author believes that it is worthy of presentation for those who will do continuing studies, the experimental procedure and progress are described in Appendix 1.

#### 2.3.1. Criteria for Selection of Alternative Encapsulants

The encapsulant material should satisfy following requirements:

- (1) The encapsulant should be immiscible with or show very limited solubility in the gallium arsenide melt.
- (2) The melting temperature of the encapsulant should be considerably lower than that of gallium arsenide. Otherwise, arsenic will be lost during the heating period due to incongruent vaporization and considerably change the stoichiometry of the melt.
- (3) The vapor pressure of the encapsulant at processing temperature should be low. A high vapor pressure causes a loss of encapsulant during the growth. In

the LEC process, it has been found that the amount of encapsulant in the crucible (especially the thickness of encapsulant layer over the melt) greatly affects the thermal profile of the process, thus changing the quality of the final crystals (81).

- (4) The encapsulant should be non-reactive with the *GaAs* melt and the crucible material.
- (5) In case that an element of the encapsulant is incorporated into *GaAs*, it should not be electrically active in the crystal.
- (6) The encapsulant should be less dense than the melt. The density of gallium arsenide melt is 5.71 g/cm at 1245 °C (30).
- (7) It is desirable that the encapsulant be transparent. This requirement becomes very critical if an optical heating method is chosen in the LEMZ growth of gallium arsenide.
- (8) The encapsulant should be available in a high purity grade in order to prevent contamination of the gallium arsenide by impurities from the encapsulant.

#### 4.3.2. Possible Alternative Encapsulants

The thermophysical properties of the encapsulant are very important in both LEC and LEMZ growth of gallium arsenide. Consider the LEMZ process. If the dynamic viscosity of the encapsulant is much higher than that of the melt, then natural convection due to buoyancy and surface tension gradients (Marangoni flow) will be diminished provided that the radius to thickness ratio ( $r/t$ ) of the melt zone is less than 8. By the same token, the "moving" melt zone behaves like "flow through

a tube with rigid wall". In this case, the encapsulant acts as a rigid wall in contact with the melt. The effect of Marangoni flow between the melt and encapsulant is of interest in the choice of alternative encapsulant. In LEMZ growth, a large surface tension reduces the prospect of a vertical wave along the surface. Thermal conductivities of the encapsulant and the melt are related to the magnitude of a preset mode of convection, and the threshold for the onset of convection in the event of a nearly insulating encapsulant. If the thermal conductivity of the encapsulant is not very small, then natural convection will occur instantaneously. If the encapsulant is virtually an insulant, then it may be possible to avoid natural convection with careful monitoring of the heat source. Since the former is more likely to occur, the effects of improved thermal conductivity of the encapsulant need to be examined. A large thermal conductivity will help to diminish the Marangoni effect, and help the decay of thermal disturbances.

Based on the reasons discussed above, new encapsulant materials with flexible thermophysical properties were investigated. An initial survey of elemental oxides indicated no candidate oxide was superior to boron oxide. The attention, therefore, was focused on the group III A or B, and the group V A or B mixed oxides since they are isoelectronic elements with respect to *Ga* or *As*. Every combination of oxides in these groups were examined and three mixtures of oxides were chosen as the candidate encapsulants. These are  $B_2O_3+Al_2O_3$ ,  $B_2O_3+La_2O_3$  and  $B_2O_3+Nb_2O_5$ . The properties of the pure oxides in this group of selected mixed oxides are listed in table 2-4 along with the properties of  $Ga_2O_3$  and  $As_2O_3$  (82, 83). The phase

Table 2-4. The Properties of Elemental Oxides (82, 83)

Group	Oxide	$T_m$ (°C) <sup>(a)</sup>	$T_b$ (°C) <sup>(b)</sup>	$\Delta G_f^\circ$ (°C) <sup>(c)</sup>
III A	$Ga_2O_3$	1725	-	-44.8(s)
	$B_2O_3$	450	2124	-73.2(l)
	$Al_2O_3$	2046	2980	-95.1(l)
III B	$La_2O_3$	2217	4200	-107.5(l)
V A	$Nb_2O_5$	1490	2927	-60.0(s)
V B	$As_2O_3$	313	457	-25.7(s)

- a. Melting Temperature
- b. Boiling Temperature
- c. Gibbs Energy of Formation at 1500 K, Kcal/g atom oxygen



diagrams of these mixtures (84) were studied to find the melting temperatures of the mixtures as a function of composition. It is desirable that the Gibbs energy of formation of the elemental oxide be more negative by approximately 20 Kcal/g-atom oxygen than that of  $Ga_2O_3$  to prevent oxidation of gallium in the melt by the encapsulant oxide. As expected, no electrical activity of elements (e.g., Al, La, and Nb) of selected oxides in gallium arsenide crystal has been reported since these elements are isoelectronic species in gallium arsenide.

Before considerable effort is devoted to the study of the thermophysical properties of selected mixed oxides, these materials should be first tested to verify their chemical compatibility with gallium arsenide and the crucible material. The tests will be described in the next sections.

### 2.3.3. Experiment

Gallium arsenide samples were grown with each of the selected mixed oxides as the encapsulant. The apparatus and growth procedure were the same as described in section 2.2.1.. Before loading the encapsulant in the quartz ampoule for growth, the boron oxide and the secondary oxide were mixed. The secondary oxides were of puratronic grade (99.999%) and purchased from Johnson Matthey Chemical Limited. The compositions of the mixed oxides used to grow the crystals are listed in table 2-5. The composition of the mixed oxides were  $B_2O_3$ -rich to maintain a low melting temperature. The most important property which needs to be adjusted for growth in space is the surface tension between the gallium arsenide melt and the encapsulant. Since the surface tension is very sensitive to impurities, even small amounts of the

Table 2-5. Compositions of Mixed Oxide Encapsulants

Encapsulant	Compositions (mole %)			
$B_2O_3$	$B_2O_3$ 100%			
$B_2O_3 + Al_2O_3$	$B_2O_3$ 98%	$Al_2O_3$	2%	
$B_2O_3 + La_2O_3$	$B_2O_3$ 95.5%	$La_2O_3$	0.5%	
$B_2O_3 + Nb_2O_5$	$B_2O_3$ 99%	$Nb_2O_5$	1%	

secondary oxide can change the surface tension substantially. The quartz ampoule, which contained the gallium arsenide and the encapsulant was cut radially with a diamond blade and the cross section was polished for energy dispersive X-ray spectroscopy (EDS) and optical microscopy. Polished gallium arsenide samples taken in the middle of crystal were analyzed by SIMS while encapsulants were analyzed by ICP for *Si* and *Ga* concentrations.

#### 2.3.4. Results and Discussion

A photo of the gallium arsenide crystal grown with the encapsulant ( $B_2O_3 + Nb_2O_5$ ) synthesized from  $B_2O_3$  with 2000 ppm  $H_2O$  is shown in figure 2-13. The bottom tip of crystal was broken during recovery. The surface of the crystal was shiny and irregular, which was the same result as described in the section 2.2.2 (see figure 2-3). The cross sectional optical micrographs of these samples are shown in figures 2-14, 2-15 and 2-16. These photos reveal that the thin layer of encapsulant had a thickness of approximately  $50 \pm 10 \mu m$ . The dark bands in the middle of photos are the layers of encapsulant, the bright and smooth areas are the gallium arsenide, and the dark and rather rough areas are the quartz ampoule. The photos also show a rough interface between the quartz ampoule and the encapsulant, indicating irregular dissolution of quartz into encapsulant. The results of the EDS analysis on encapsulant layer are shown in figures 2-17, 2-18 and 2-19. Silicon and aluminum were detected in all three mixed oxides along with the metallic element of the secondary oxide. It is obvious that silicon originated from the dissolution of the quartz ampoule and the aluminum from  $Al_2O_3$  powder used to polish the samples.



Figure 2-13. Polycrystalline *GaAs* grown with the mixed oxide encapsulant  $B_2O_3+Nb_2O_5$ .

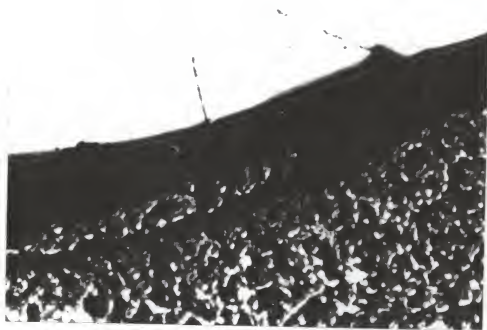


Figure 2-14. Cross sectional optical micrograph of encapsulant ( $B_2O_3+Al_2O_3$ ), *GaAs* and quartz crucible. Magnification; 200x.

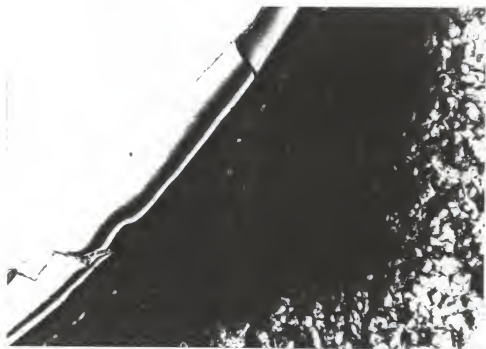


Figure 2-15. Cross sectional optical micrograph of encapsulant ( $B_2O_3+La_2O_3$ ), GaAs and quartz crucible. Magnification; 500x.

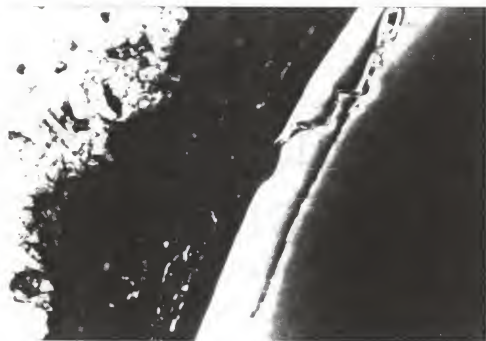


Figure 2-16. Cross sectional optical micrograph of encapsulant ( $B_2O_3+Nb_2O_5$ ), GaAs and quartz crucible. Magnification; 500x.

University of Florida / MAIC  
Cursor: 0.000kev = 0

FRI 08-JUL-88 11:13

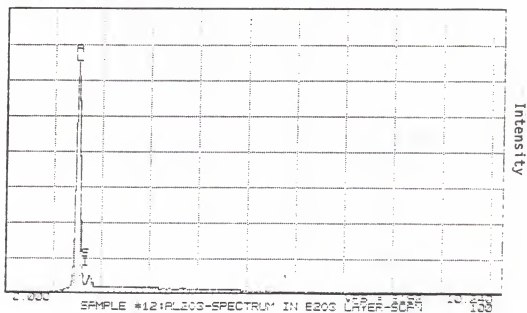


Figure 2-17. EDS analysis of the mixed oxide encapsulant  $B_2O_3+Al_2O_3$ .



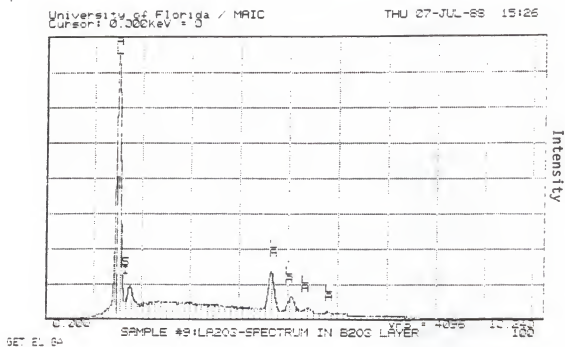


Figure 2-18. EDS analysis of the mixed oxide encapsulant  $B_2O_3+La_2O_3$ .

University of Florida / MAIC  
Cursor: 0.000keV = 0

FPI 08-JUL-88 10:15

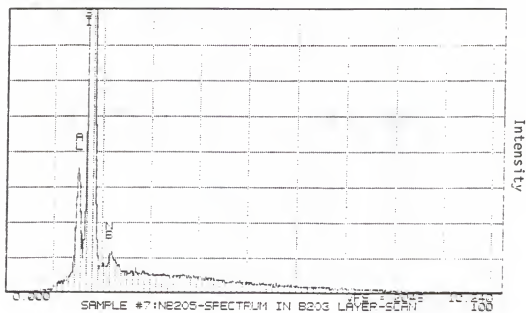


Figure 2-19. EDS analysis of the mixed oxide encapsulant  $B_2O_3+Nb_2O_5$ .

In the case of encapsulant ( $B_2O_3+Al_2O_3$ ), however, some of the aluminum came from the  $Al_2O_3$  mixed with the boron oxide. The dependence of silicon and gallium dissolution in the mixed encapsulants on the water content and processing time were also studied and the results are shown in figures 2-20, 2-21, 2-22 and 2-23. The results show a similar dependence on water content as in the pure boron oxide. The result of pure boron oxide is also included in these figures for comparison. The encapsulant ( $B_2O_3+Al_2O_3$ ) had the lowest concentration of silicon while the encapsulant ( $B_2O_3+Nb_2O_5$ ) had the highest concentration (figure 2-20). The encapsulant ( $B_2O_3+Nb_2O_5$ ) also showed the highest concentration of gallium while pure boron oxide showed the lowest (figure 2-21). The high concentration of both impurities in the encapsulant ( $B_2O_3+Nb_2O_5$ ) are probably due to the high Gibbs energy of formation of  $Nb_2O_5$ , causing oxidation of  $Ga$  in the melt.

SIMS analysis was performed on the polished samples of gallium arsenide. The results of the SIMS analysis are listed in table 2-6. The encapsulant ( $B_2O_3+Al_2O_3$ ) showed the highest concentrations of silicon and boron as well as the concentrations of aluminum (from  $Al_2O_3$ ). The encapsulant ( $B_2O_3+Nb_2O_5$ ) showed the same or lower concentrations of silicon and boron compared to pure boron oxide. Furthermore, the incorporation of  $Nb$  was on the order of  $10^{14}/cm^3$ . Based on these results the encapsulant ( $B_2O_3+Nb_2O_5$ ) is the best candidate for an alternative encapsulant, though the other two candidates showed acceptable characteristics. These three candidates should be further studied in terms of their thermophysical properties. A final conclusion can not be made until the measurements of the

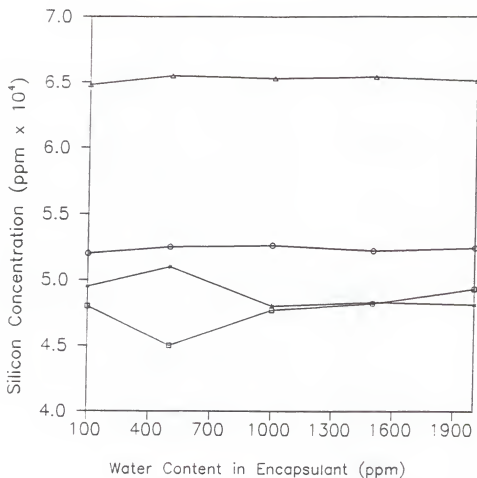


Figure 2-20. Silicon concentration in the encapsulant as a function of the encapsulant water content at 1250 °C for a contact time of 60 minutes. \*,  $B_2O_3$ , □,  $B_2O_3 + Al_2O_3$ , ○,  $B_2O_3 + La_2O_3$ , Δ,  $B_2O_3 + Nb_2O_5$ .

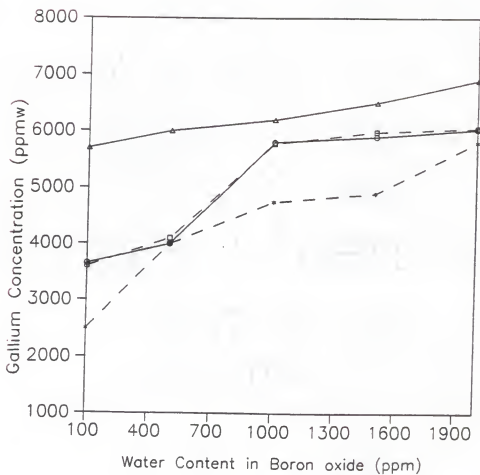


Figure 2-21. Gallium concentration in the encapsulant as a function of the encapsulant water content at 1250 °C for a contact time of 60 minutes. \*,  $B_2O_3$ , □,  $B_2O_3+Al_2O_3$ , ○,  $B_2O_3+La_2O_3$ , Δ,  $B_2O_3+Nb_2O_5$ .

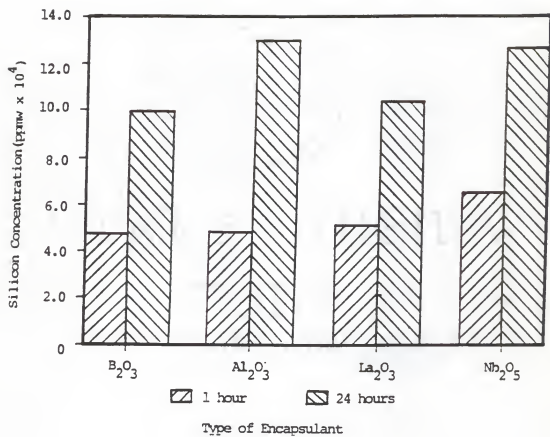


Figure 2-22. Time dependence of silicon dissolution in the various encapsulants at 1250 °C.

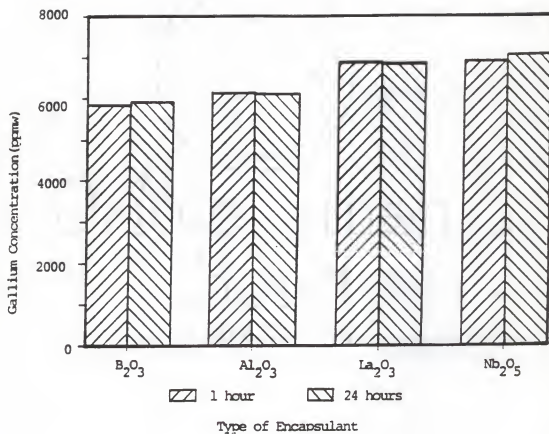


Figure 2-23. Gallium concentration in the various encapsulants as a function of contact time at 1250 °C.

Table 2-6. SIMS Analysis of GaAs \*

	GaAs grown with various encapsulants			
	$B_2O_3$	$B_2O_3+Al_2O_3$	$B_2O_3+La_2O_3$	$B_2O_3+Nb_2O_5$
<i>Si</i>	$3 \times 10^{15}$	$8 \times 10^{16}$	$\leq 3 \times 10^{14}$	$2 \times 10^{15}$
<i>B</i>	$2 \times 10^{16}$	$2 \times 10^{17}$	$5 \times 10^{15}$	$1 \times 10^{15}$
<i>Al</i>	$2 \times 10^{15}$	$1 \times 10^{17}$	$2 \times 10^{15}$	$4 \times 10^{15}$
<i>La</i>	-	-	$\leq 1 \times 10^{16}$	-
<i>Nb</i>	-	-	-	$3 \times 10^{14}$
<i>O</i>	$\leq 3 \times 10^{16}$	$\leq 3 \times 10^{16}$	$\leq 4 \times 10^{16}$	$2 \times 10^{18}$
<i>Cr</i>	$2 \times 10^{13}$	$3 \times 10^{13}$	$2 \times 10^{13}$	$3 \times 10^{13}$
<i>Fe</i>	$6 \times 10^{14}$	$2 \times 10^{15}$	$2 \times 10^{15}$	$1 \times 10^{15}$
<i>Mn</i>	$3 \times 10^{14}$	$3 \times 10^{14}$	$3 \times 10^{14}$	$4 \times 10^{14}$
<i>S</i>	$1 \times 10^{16}$	$5 \times 10^{15}$	$3 \times 10^{16}$	$2 \times 10^{16}$
<i>P</i>	$3 \times 10^{15}$	$4 \times 10^{15}$	$4 \times 10^{15}$	$4 \times 10^{15}$
<i>Se</i>	$\leq 1 \times 10^{13}$	$1 \times 10^{14}$	$2 \times 10^{13}$	$1 \times 10^{14}$
<i>Na</i>	$\leq 1 \times 10^{14}$	$\leq 1 \times 10^{14}$	$\leq 1 \times 10^{14}$	$\leq 1 \times 10^{14}$
<i>Mg</i>	$2 \times 10^{14}$	$\leq 6 \times 10^{13}$	$\leq 5 \times 10^{13}$	$\leq 3 \times 10^{13}$
<i>Be</i>	$\leq 3 \times 10^{13}$	$\leq 7 \times 10^{13}$	$\leq 4 \times 10^{13}$	$\leq 4 \times 10^{13}$
<i>C</i>	$3 \times 10^{16}$	$3 \times 10^{16}$	$2 \times 10^{16}$	$\leq 1 \times 10^{16}$
<i>H</i>	$\leq 5 \times 10^{16}$	$7 \times 10^{16}$	$\leq 6 \times 10^{16}$	$7 \times 10^{16}$

\*. SIMS analysis was performed by Charles Evans & Assoc..

The water concentration in all encapsulants was 100 ppm.

Impurity concentrations in  $\text{atoms}/\text{cm}^3$ .



thermophysical properties are performed. The optimization must consider not only the thermophysical properties but also the incorporation rate of impurities in the gallium arsenide.

After each growth, the encapsulant was visually examined and it was found that encapsulant had changed from transparent to a gray color. In addition, many bubbles were formed in the encapsulant. Several growths were performed to determine the cause of the color change and bubble formation in the cooled encapsulant. In these experiments the boron oxide and the mixed oxides were grown by the same procedure with or without gallium arsenide and the results are summarized in table 2-7. From these experiments the following conclusions can be made:

- (1) Boron oxide grown in a quartz ampoule remained transparent after growth and the boron oxide grown with either gallium arsenide or other oxides became gray after growth. It appears that precipitates of the secondary metallic oxides caused the color change.
- (2) The gallium plays a role in the bubble formation since Ga was required to form the bubbles. This fact leads to the conclusion that  $Ga_2O$  is produced by reaction (2.4). This species then precipitates on cooling (possibly forming  $Ga_2O_3$ ). Some of  $Ga_2O$  is trapped in the liquid encapsulant and forms the bubbles, while the remainder of  $Ga_2O$  escapes the liquid encapsulant and deposits on the top of quartz wall.

Table 2-7. Occurrence of Color Change and Bubble Formation in the Processed Encapsulant

Samples	Observation After Growth
$B_2O_3$	No Bubbles, Transparent
Mixed Oxides	No Bubbles, Gray
$B_2O_3 + Ga_2O_3$	Bubbles, Gray
$B_2O_3 + GaAs$	Bubbles, Gray
Mixed Oxide + $GaAs$	Bubbles, Gray

## CHAPTER 3

### MEASUREMENT OF THE Ga ACTIVITY ALONG THE Ga-RICH LIQUIDUS AND CRITICAL ASSESSMENT OF THE PHASE DIAGRAM AND THERMOCHEMISTRY OF THE Ga-As SYSTEM

As the commercial applications of compound semiconductors increase in number and device processing steps become more complex, there is an increased need for more accurate and comprehensive knowledge of the thermodynamic properties and phase diagrams of these materials. Since many of the processing steps, such as liquid phase epitaxy (LPE) and bulk crystal growth, involve near equilibrium contact of liquid and solid phases, the phase diagram is important for providing boundary conditions. Equilibrium between the solid and vapor is also important in such processes as chemical vapor deposition (CVD) and rapid thermal annealing. Important to the work reported in this dissertation is the contact of *Ga-As* melt with quartz and the liquid encapsulant. An analysis of impurity distributions will necessarily require knowledge of the phase diagram and thermochemistry of the *Ga-As* system.

In this chapter, the activity of gallium along the liquidus line in gallium-rich melts of *Ga* and *As* was measured using a solid electrolyte galvanic cell. There have been two previous attempts to measure the activity of gallium in *Ga-As* melts using the same method. Wypartowicz and Fitzner (85) measured the activity of gallium

with a galvanic cell using yttria stabilized zirconia (YSZ) as the solid electrolyte. More recently, Katayama *et al.* (86) determined the activity of gallium using a calcia stabilized zirconia (CSZ) solid electrolyte. Though their experimental apparatus and procedure were similar, there was significant differences in their results. In the temperature range 994-1154 K, Katayama *et al.* (86) obtained an almost constant value of the cell potential (2.0 to 2.8 mV). The activity of gallium determined from their measurements showed a negative deviation from ideal solution behavior. However, Wypartowicz and Fitzner (85) in the temperature range 973-1273 K found that the cell potential decreased rapidly toward zero with increasing temperature and the absolute values of the emf gave negative deviation from ideal solution behavior. A major problem in studying the Ga-As system is arsenic loss due to volatilization during the experiment. Loss of As would drive the working electrode composition chosen to that of the reference electrode and thus drive the voltage toward zero. In our experiment, the loss of arsenic element was minimized by using a self-sealing configuration as described in section 3.1.2.

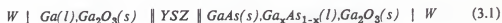
The measured activity data of this study were then included in a critical assessment of the phase diagram and thermodynamic properties of the Ga-As system. Tmar *et al.* (87) and Chatillon *et al.* (88) had optimized the thermodynamic properties and phase diagram of the Ga-As system using the procedure developed by Lukas *et al.* (89). A similar analysis was performed in which the activity measurements of this study were included. The consistency of this new data with that of others was evaluated, and new optimized coefficients of the excess Gibbs energy

of the liquid phase were obtained. In this optimization, careful evaluation of available thermodynamic data is critical to achieving a reliable calculated description of the system, as is the choice of a reasonable solution model.

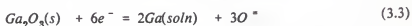
### 3.1 Measurement of the Activity of Ga Along the Ga-rich Liquidus

#### 3.1.1. Theory

The solid-state galvanic cell employed to measure the activity of gallium along the liquidus line for the Ga-rich segment of the Ga-As system is represented schematically as



where YSZ is  $ZrO_2$  stabilized in the tetragonal lattice by  $Y_2O_3$ . The half cell reactions are



Therefore the overall reaction can be represented by



where  $Ga(soln)$  represents gallium in the mixture  $Ga_xAs_{1-x}$ . The Gibbs energy change for reaction (3.4) is

$$\Delta G = \Delta G^\circ + RT \ln K = \Delta G^\circ + 2RT \ln \left( \frac{a_{Ga(soln)}}{a_{Ga(pure)}} \right) \quad (3.5)$$

If pure  $Ga(l)$  at the temperature and pressure of interest is chosen as the reference

state, then  $\Delta G^0=0$  and  $a_{\text{Ga(pure)}}=1$ , and equation (3.5) becomes

$$\Delta G = 2RT \ln a_{\text{Ga(soln)}} \quad (3.6)$$

If the cell is considered as a thermodynamic system, then one of the combined statements of the first and second laws of thermodynamics for a reversible process is

$$dG = VdP - SdT - dW \quad (3.7)$$

The Gibbs energy change,  $dG$ , on passing one Faraday of electrical charge,  $F$ , across the cell is equal to the reversible electrical work,  $nFdE$ , as long as the intensive properties temperature and total pressure are constant, so that

$$dG = -dW = -nFdE, \quad \Delta G = -nEF \quad (3.8)$$

where  $F$  is the Faraday constant (96,500 coulomb),  $n$  the number of electrons involved in the cell reaction, and  $\Delta G$  the Gibbs energy change when one Faraday of electricity is passed at constant  $E$ . Then by equations (3.6) and (3.8),

$$\Delta G = 2RT \ln a_{\text{Ga}} = -nEF \quad (3.9)$$

and with  $n=6$ ,

$$a_{\text{Ga}} = \exp\left(\frac{-3EF}{RT}\right) \quad (3.10)$$

where the simpler notation  $a_{\text{Ga}}$  has been substituted for  $a_{\text{Ga(soln)}}$ . Therefore the activity of gallium in the Ga-As system can be obtained by measuring the open-circuit emf of the galvanic cell (3.1).

### 3.1.2. Experimental

After the initial work by Kiukkola and Wagner (90, 91), galvanic cells have become an important experimental technique, along with calorimetric and vapor pressure measurement methods, for the determination of thermodynamic properties of alloy systems. Since the usefulness of solid electrolytes in galvanic cells was demonstrated by their measurements of the standard Gibbs energies of formations of several oxides, sulfides, and tellurides, several review papers have been published on this subject (92-95).

In using solid electrolytes for high temperature equilibrium measurements, there are several factors that should be considered in the cell design. First, the solid electrolyte chosen for the experiment should have an ionic transference number,  $t_{ion}$ , greater than 0.99. The ionic transference number is defined as the ratio of the ionic conductivity of the solid electrolyte to its total conductivity and depends mainly on the temperature and ionic species partial pressure of the system. If  $t_{ion}$  is less than 0.99, there is sufficient electronic conduction in the electrolyte to create a problem in maintaining fixed chemical potentials at the electrode-electrolyte interfaces, resulting in a non-stable emf. Any reaction within the electrode or between the electrodes and the electrolyte can lead to chemical potential variations in the electrode. When using alloy-oxide electrodes, one can prevent an oxide-alloy reaction by using only those alloys in which one metal oxide is at least 84 kJ/mol (20 Kcal/mol) more stable than the other.

Because the oxygen pressure in an inert gas can be reduced to as low as  $10^{-15}$  atm by purification, it is preferable to make high temperature electrochemical measurements in a flowing argon or helium atmosphere rather than in a vacuum. However, there are two experimental precautions which can be taken to avoid problems with an inert gas atmosphere, particularly when the oxygen pressure fixed by the electrode is below  $10^{-20}$  atm. First, an oxygen getter (*i.e.*, tantalum or niobium foil) can be placed inside the reaction tube upstream from the cell. The metal foil will remove any residual oxygen or water which may arise from the internal sources such as degassing of the refractory tubes. Second, one can determine the effect of the inert gas flow rate on the measured emf. If there is a flow rate effect, oxygen in the inert gas is establishing a mixed potential at the electrode-electrolyte interface.

With careful cell preparation and cell design, the influence of electronic conductivity, chemical reactions and the gaseous atmosphere can be eliminated. However, the time necessary to equilibrate constituents must be considered. With single phase electrodes of solid metals or non-stoichiometric oxides, equilibration is obviously limited by diffusion processes in the solid phase. To avoid compositional gradients in the electrode at the electrode-electrolyte interface, intimate interfacial contact is essential.

The above precautions were taken into consideration in the cell design. The yttria stabilized zirconia (YSZ) was used as the solid electrolyte since its electrolytic domain, in which the ionic transference number was greater than 0.99, was found to be suitable for this experiment. Products from possible side reactions between lead



wire, electrolyte and electrodes were checked by X-ray diffraction. In the inert gas line, two traps (titanium sponge heated at 850 °C to remove  $O_2$ ,  $N_2$ ,  $CO$ , and  $CO_2$  and type 13X molecular sieve to remove water vapor) were installed to purify the inert gas ( $Ar$ ). The effect of argon gas flow rate on the cell potential was examined during experiments.

The measurement of open-circuit emf values in galvanic cells can provide thermodynamic quantities such as component activity data, Gibbs energies of formation, and enthalpy values, as well as phase diagram data, depending on the type of cell used and the system studied. In addition, the method of coulometric titration, introduced by Wagner (96), allows accurate changes in composition to be determined, whereby deviations from ideal stoichiometry and the defect structures in binary compounds can be determined (97).

Experimental Cell Design. A schematic of the experimental cell design is depicted in figure 3-1. This cell was designed to minimize the volatilization of  $As$  during cell operation at elevated temperature. The faces of the alumina cups, which contained the electrode materials, and the YSZ electrolyte discs were carefully polished to eliminate any gap between these parts. The stacked electrode cups were pressed between stainless steel plates which were held together by four  $Ta$  rods. A tight seal between the electrolyte and electrode cups was produced upon heating by the greater expansion of the  $Ta$  rods. Tungsten lead wires were inserted into the electrode through very small grooves on the face of alumina cups. These grooves were made sufficiently small to fit the wires tightly and alumina cement was applied

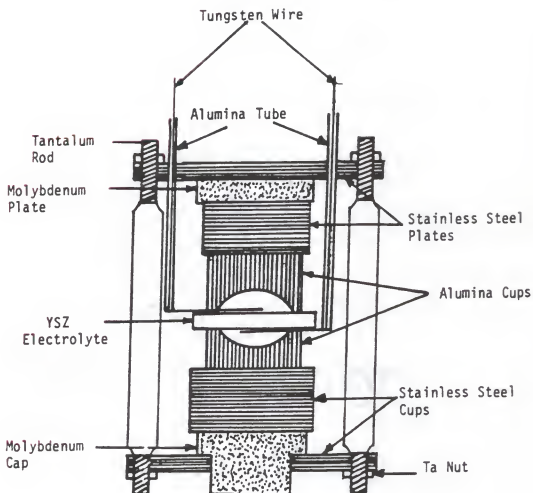


Figure 3-1. Schematic of the solid state electrochemical cell used for the activity measurement.

to ensure leak a tight seal. Approximately 0.1 g of a gallium and gallium arsenide mixture (75 mole % of *Ga* and 25 mole % of *As*) was combined with 0.1 g of gallium oxide in the working electrode cup. Similarly, approximately 0.1 g of gallium and gallium oxide mixture (mole ratio of 3/2) was placed in the reference electrode.

The cups were made of alumina to avoid any reaction between the electrodes and cups. A type S thermocouple was placed just beside the YSZ electrolyte to monitor the cell temperature. The molybdenum cap and plate were centered by fitting them into the holes drilled in the center of stainless steel plates.

The assembled cell was placed inside a 2 inch diameter closed-one-end alumina tube 20 inches in length and secured by a Viton O-ring to a water cooled brass cell-head. The thermocouple and lead wires sheathed with alumina were passed through Cajon through-bore fittings and the bores of the alumina sheathes were sealed with epoxy. The cell was suspended by platinum wire from the cell head. Two additional fittings were located on the cell head for gas entrance and exit. The overall cell configuration is shown in figure 3-2.

The furnace used was the same as described in chapter 2. A flat temperature zone of approximately 30 inches was established to ensure that no temperature gradient existed along the cell. The temperature uniformity and stability were held to within  $\pm 0.5$  °C in the vicinity of the electrodes. The inert gas (*Ar*) was purified in two steps before entering the cell. Residual oxygen, nitrogen, carbon monoxide and carbon dioxide were removed by first passing the inert gas over hot (850 °C) titanium sponge. Next water vapor was removed again by flowing through a

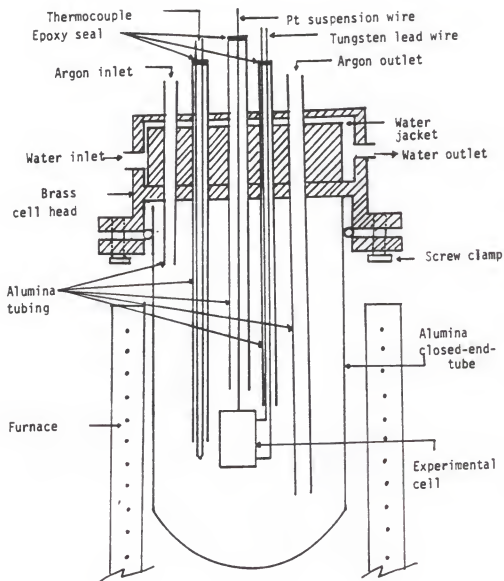


Figure 3-2. Schematic of overall cell configuration.

molecular sieve trap. All the valves in the system were pneumatically operated while tubing was 1/4 inch stainless steel and the pressure of inert gas was controlled by a pressure controller (MKS type 250B). The cell emf was measured with a Keithley 614 electrometer. A Princeton Applied Research Model 273 Potentiostat/Galvanostat was used to titrate the cell to confirm the reversibility of emf.

Materials. The *GaAs* used for crystal growth in chapter 2 was used in a powder form. The *Ga* metal used in the study was semiconductor grade, 99.9999 mole percent pure (Alcan Electronic Materials AG). The mixture of *GaAs* and *Ga* in the working electrode was prepared to have 75 mole percent of gallium and 25 mole percent of arsenic. Gallium oxide had a purity of 99.99 mole percent (Alfa Products). The YSZ disks were 1 inch in diameter and 1/16 inch in thickness (Zircona Corporation of America) and contained 8 mass percent  $Y_2O_3$ . The purified *Ar* purged the system at a flow rate of approximately 60 *sccm*.

Procedure. In each of several experiments the cell compartments were leak-checked using a vacuum system by monitoring any pressure increase, then purged with high purity argon. The cell was first baked overnight at 200 °C with argon flowing to drive off water vapor from the cell. Then the cell emf was measured and periodically recorded at each temperature until equilibrium was reached and confirmed. In most experiments it took approximately 2 hours for the cell to reach equilibrium after a constant cell temperature was achieved. The cell emf was confirmed by titration, *i.e.*, passing current ( $\pm 20 \mu A$  for 20 seconds) through the cell and observing reversibility of cell emf. Only increases in temperature could be made,

since decreasing the temperature by more than 10 °C incurred the risk of breaking the seal between the electrode cups due to the difference of thermal expansion of stainless steel and Ta rods. All thermocouples used in this measurement were calibrated with NBS standard type S thermocouple. The argon flow rate did not affect the cell emf in the range selected. At the conclusion of each experiment the cell compartments were again checked for leak as described earlier and the tungsten lead wire was examined for evidence of oxidation or any side reactions by X-ray diffraction. Uncertainties in the measured values arose from the sensitivity of the electrometer used to measure the cell emf ( $\pm 0.01$  mV) and the temperature measurement ( $\pm 0.5$  K).

### 3.1.3. Results and Discussion

Emf data were obtained for the Ga-rich segment of the Ga-As system along the liquidus line in the temperature range of 923-1373 K using the cell (3.1). The measure cell potentials and temperatures are listed in Table 3-1. The gallium activity along the liquidus line in this temperature range was calculated from the measured cell potential by equation (3.10). The emf data from this cell are directly related to the relative partial molar Gibbs energy of gallium,  $g_{Ga}^M$ , along the liquidus line in the Ga-As system by the following equation:

$$g_{Ga}^M = -3EF \quad (3.11)$$

Table 3-1. Emf and Calculated Thermodynamic Properties

$T(K)$	emf (mV)	$x_{Ga}^*$	$g_{Ga}^M$ (J/mol)	$g_{Ga}^E$ (J/mol)	$a_{Ga}$	$\gamma_{Ga}$
923	0.11	0.9965	-32	-5.3	0.995	0.999
973	0.23	0.9910	-67	0.8	0.991	1.000
1023	0.67	0.9865	-198	-82.9	0.976	0.990
1048	0.92	0.9810	-265	-99.0	0.969	0.988
1073	1.21	0.9755	-349	-127.6	0.961	0.985
1098	1.57	0.9650	-453	-128.7	0.951	0.986
1123	1.77	0.9585	-512	-116.5	0.946	0.987
1148	2.50	0.9470	-723	-203.5	0.927	0.978
1173	3.41	0.9345	-988	-328.3	0.903	0.966
1198	4.24	0.9250	-1228	-398.3	0.884	0.960
1223	5.22	0.9075	-1511	-523.7	0.861	0.949
1248	6.57	0.8865	-1901	-652.0	0.832	0.939
1273	7.80	0.8715	-2286	-830.8	0.805	0.924
1298	9.49	0.8575	-2746	-1087.9	0.775	0.904
1323	11.02	0.8315	-3189	-1160.1	0.748	0.899
1348	13.85	0.8145	-4009	-1711.1	0.699	0.858
1373	17.26	0.7865	-4996	-2255.6	0.645	0.820

\* The mole fractions of gallium along the liquidus temperature were obtained from the optimizatoin results of Tmar *et al.* (87).

Other thermodynamic properties of gallium can be obtained by the following equations:

$$g_{Ga}^E = g_{Ga}^M - RT \ln x_{Ga} \quad (3.12)$$

$$a_{Ga} = \exp\left(\frac{g_{Ga}^M}{RT}\right) \quad (3.13)$$

$$\gamma_{Ga} = \exp\left(\frac{g_{Ga}^E}{RT}\right) \quad (3.14)$$

where  $g_{Ga}^E$  and  $\gamma_{Ga}$  are the excess partial molar Gibbs energy and the activity coefficient of gallium, respectively. The emf data are plotted in figure 3-3 as a function of liquidus temperature, and listed with other calculated thermodynamic properties from equations (3.11) to (3.14) in table 3-1.

As mentioned previously, there were two studies that measured the activity of gallium in the *Ga-As* system along the liquidus line using the emf method (85, 86). In figure 3-3, these emf data are also plotted. As shown in figure 3-3, each data set is quite different from each other. The  $a_{Ga}$  calculated from the emf data listed in table 3-1 is plotted in figure 3-4. In this figure, curves representing ideal solution and the activity of gallium deduced from the measurement of arsenic vapor pressure over solid gallium arsenide by Arthur (98) are also included. In his experiment, mass spectrometric and weight loss measurements of the species effusing from a Knudsen-cell containing *GaAs* were used to obtain vapor pressures over the temperature range 900 to 1200 K. In Arthur's original calculation, the activity of arsenic was determined from the measured partial pressure of  $As_4$  above the saturated solution. This was



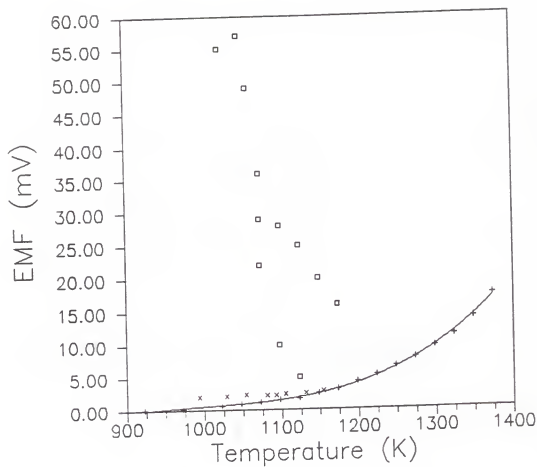


Figure 3-3. Emf of cell (3.1) as a function of temperature. +---+: this study, □: Wypartowicz and Fitzner (85), x: Katayama *et al.* (86).

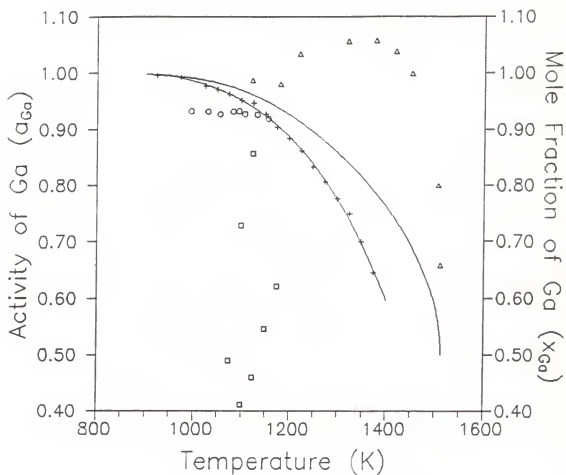


Figure 3-4. The activity of gallium along the liquidus line (gallium-rich segment), calculated with emf data obtained. +--+ : this work by emf, — : ideal solution, □: Wypartowicz and Fitzner by emf (85), ○: Katayama *et al.* by emf (86), △: Arthur by vapor pressure measurement (98).

accomplished by using the relationship between the partial pressure of  $As_4$  and the activity of arsenic,  $\gamma_{As}$ , proposed by Thurmond (99). The activity of gallium was calculated from the equilibrium constant expression for the reaction of the decomposition of  $GaAs$  to form  $As_4$  and a liquid phase. For this calculation  $x_{As}$ , the atomic fraction of arsenic on the liquidus line, was obtained from the phase diagram data of Hall (100) and Köster and Thoma (101). However, their phase diagram data are not believed to be accurate. This seems to be the reason that Arthur's activity of gallium shows positive deviation from the ideal solution behavior. The activity of gallium from Katayama *et al.* (86) is negatively deviated from ideal solution behavior while the activity from Wypartowicz and Fitzner (85) is scattered very much and seems that their data are erroneous. Our activity shows slight negative deviation from ideal solution at low temperature. But as temperature increases the negative deviation becomes more severe. Our emf data are included in the optimization calculation described in the next section to see the consistency with other thermodynamic properties of gallium arsenide. The activity coefficient from this work is shown in figure 3-5.

### 3.2 Optimization of the Thermochemical Properties and Phase Diagram for the Ga-As System

#### 3.2.1. Introduction

An intense investigation of the thermochemical properties and phase diagram for the  $Ga-As$  system has been performed using a variety experimental techniques. This system is very difficult to study since gallium and arsenic are very reactive,  $GaAs$

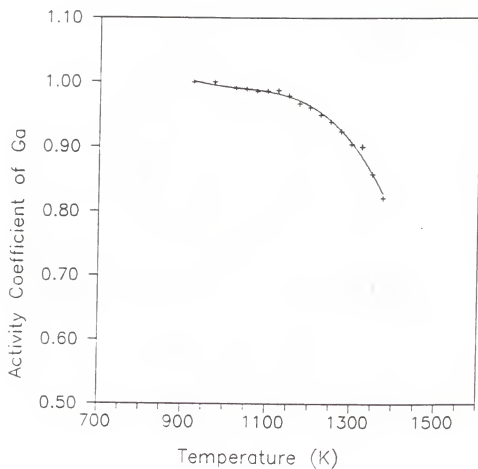


Figure 3-5. The measured activity coefficient of gallium along the liquidus line (gallium-rich region).

has a high melting temperature (1238 °C) and high vapor pressures can be encountered (*As* sublimates at 1 atm and 617 °C). Furthermore, *As* polymerizes in the vapor phase to form predominantly the  $As_2$  and  $As_4$  species. As a result much of the data in the literature has been shown to be inconsistent (87). For instance, measured activities of gallium in the *Ga-As* system have not been in agreement between investigators. The high *As* vapor pressures encountered in the *As*-rich compositions has produced a paucity of data in this region of the phase diagram.

Tmar *et al.* (87) performed a thorough analysis and optimization of the available data to achieve a consistent set of thermodynamic and phase diagram data when using selected experimental values from the literature. In this study, each original data set was evaluated for experimental error and the revised data sets were included in a broad optimization scheme (Lukas software). In this procedure, data sets were selectively eliminated and a final assessment gave a consistent property set. Later Chatillon *et al.* (88) re-optimized the *Ga-As* system while including several new published phase diagram data, enthalpy of mixing and the partial Gibbs energies.

The data sets originally used by Chatillon *et al.* (88) were obtained from these researchers and the activity measurements of this study were simultaneously reevaluated. The results of this optimization are presented below.

### 3.2.2. Data Acquisition

Phase Diagram. The various measured gallium arsenide phase diagrams show relatively good agreement between each other. However the phase diagram for arsenic-rich compositions is not well defined due to the lack of experimental data.

A full discussions of the data set can be found in references (87) and (88). A summary of the experimental techniques and the estimated errors are listed in table 3-2. For the optimization, reference (109) was discarded due to the large disagreement with other data.

Thermodynamic Data. The thermodynamic data published for the gallium arsenide system are listed in tables 3-3 and 3-4. References (86), (111), (114), (116), (118), (119), (120), (121), and (122) were not included in the optimization due to a disagreement with other data.

### 3.2.3. Optimization Method

The original data file used for optimization in reference (88) was obtained from the authors of this reference. The activity data of this study and two additional thermodynamic property measurements (86, 125) were included in the final optimization. An optimization program developed by Lukas *et al.* (89) was used. All of the selected experimental data, with their estimated errors, were utilized in the program to obtain an optimal set of coefficients for the temperature and concentration dependence of the excess Gibbs energy of the liquid and the temperature dependence of the excess Gibbs energy of solid *GaAs*. The phase stabilities of the pure components, gallium and arsenic, were calculated assuming a linear dependence of Gibbs energy of fusion with respect to temperature;

$$G^{\circ,l} - G^{\circ,s} = A + BT \quad (3.15)$$

Table 3-2. Summary of the Experimental Phase Diagram Data for *GaAs* in the Literature

Method	Range $T(K)$ $x_{As}$	Estimated $\pm \Delta T$	Error <sup>(*)</sup> $\pm \Delta x_{As}$	Ref.
Solubility Measurement	1013-1121 0.01170-0.03848	10	0.005	102
Differential Thermal Analysis (DTA)	1273-1511 0.15-0.80	20	0.01	101
Surface Reflectivity Measurement	958-1178 0.00559-0.0628	10	0.02	103
Heterogeneous Equil. and DTA	723-1273 0.000041-0.122	10	0.01	100
Filtration Technique	723-1511 -	20	0.05	104
Dew Point and Continuous Weighing	1447-1505 0.31-0.54	5	0.05	105
Bourdon Gauge and Vapor Density	1253-1353 0.104-0.22	20	0.05	106
Heterogeneous Equil. and Weight Loss	853-943 -	5	0.05	107
Direct Visual Obs. and Source Dissolution	623-923 -	20	0.05	108
Visual Obs. of Crystal <sup>**</sup>	965-1173 -	5	0.01	109
Neutron Diffraction	1020-1173 -	15	0.02	110

\* Estimated errors were cited from reference (87)

\*\* Data not included in the optimization

Table 3-3. Summary of Experimental Activity Measurements for *GaAs* in the Literature

Method	Temperature Range (K)	Estimated Error $\pm \Delta T(K)$ Press. <sup>(a)</sup>		Ref.
Knudsen-cell Mass Spectrometry	890-1190	10	20	98
Dew Point Method*	1323-1473	3	20	111
$H_2+PH_3$ Flow Method	1255-1435	10	20	112
Standard Bourdon Gauge	1323-1527	3	20	113
Vapor Density and Microscopic Obs.*	1511	-	-	114
Knudsen-cell Mass Spectrometry	1035-1239	10	20	115
Knudsen-cell Mass Spectrometry*	850-1100	10	20	116
Dynamic Method	973-1273	-	-	117
Knudsen-cell Mass Spectrometry*	1031-1136	10	30	118
Knudsen-cell Mass Spectrometry*	1068-1255	10	30	119
Continuous Weighing	1448-1511	3	20	105
Dew Point Method*	1054-1508	3	20	120
emf	923-1373	5	-	(b)
emf*	944-1154	10	-	86

(a) Estimated error of pressure is obtained by  $\Delta P(As_2)/P(As_2)$ .

(b) From this work

\* Data not included in the optimization



Table 3-4. Summary of the Thermodynamic Experimental Measurements in the Ga-As System

Data Type	Method	Temp. Range or Value	Estimated Error	Ref.
Gibbs Energy of formation	emf	673-741(K)	-	121
	emf	638-1373(K)	-	122
Enthalpy of Formation at 298 K	Precipitation	-41148(J/g atom)	$\pm 5000$ (J/g atom)	123
	Oxygen Calorimetric Bomb	-43848(J/g atom)	$\pm 5000$ (J/g atom)	124
Enthalpy of Fusion	Drop Calorimetry	52702(J/g atom)	$\pm 2500$ (J/g atom)	125
Heat Content	Drop Calorimetry	400-1513(K)	$\pm 10(K)$	125
Heat of Mixing	Drop Calorimetry	800-1550(K)	$\pm 10(K)$	126

where  $A$  and  $B$  are related to the enthalpy and entropy of fusion. These equations are given by SGTE (127).

$$\{G^{\circ,l} - G^{\circ,s}\}_{Ga} (J/mol) = 5589.80 - 18.45310T(K) \quad (3.16)$$

$$\{G^{\circ,l} - G^{\circ,s}\}_{As} (J/mol) = 24442.90 - 22.42470T(K) \quad (3.17)$$

The Gibbs energy of formation of the compound ( $Ga(s) + As(s) = GaAs(s)$ ) was represented by the following equation:

$$\Delta G_f^{\circ} = a - bT + cT(1 - \ln T) - \frac{dT^2}{2} - \frac{e}{2T} \quad (3.18)$$

For the liquid phase, the Redlich-Kister polynomial was chosen:

$$\Delta G^E = x_i x_j \sum_{\nu=0}^n (x_i - x_j)^{\nu} L_{ij}^{(\nu)} \quad (3.19)$$

where the coefficient  $L_{ij}^{(\nu)}$  are linear functions of temperature, which can be represented by

$$L_{ij}^{(\nu)} = A_{ij}^{(\nu)} - B_{ij}^{(\nu)} T \quad (3.20)$$

When  $n=0$  the expression corresponds to that derived from the regular solution model. Moreover, if  $n=0$  and  $L_{ij}^{(0)}$  is temperature dependent,  $\Delta G^E$  will describe the thermodynamic properties of mixing according to the "simple model". The coefficients  $A_{ij}$  and  $B_{ij}$  correspond to the temperature independent contributions to the enthalpy and excess entropy from the optimization program. The overall Gibbs energy of the liquid, in  $J/mol$ , is represented by following equation:

$$\begin{aligned}
 G = & x_{Ga}(G^{o,l} - G^{o,g})_{Ga} + x_{As}(G^{o,l} - G^{o,g})_{As} + RT\{x_{Ga}\ln x_{Ga} + x_{As}\ln x_{As}\} \\
 & + x_{Ga}x_{As}\sum_{\nu=0}^n \{A_{GnAs}^{(\nu)} - B_{GnAs}^{(\nu)}\}(x_{Ga} - x_{As})^\nu
 \end{aligned} \quad (3.21)$$

where  $T$  is in  $K$  and the third term represents the ideal configurational entropy.

During optimization the following procedure was used:

1. The optimization started with four parameters ( $a, b, A_{ij}^0, B_{ij}^0$ ).
2. Using only enthalpy of mixing data, the two enthalpy coefficients ( $a, A_{ij}^0$ ) were allowed to float while the rest of coefficients were held constant.
3. The two enthalpy coefficients obtained in step 2 were fixed, and then the two entropy coefficients ( $b, B_{ij}^0$ ) were allowed to float using the phase diagram data and the partial Gibbs energy data to optimize the entropy coefficients.
4. All four coefficients were allowed to float using all the selected data.
5. Because these four coefficients gave poor convergence in the optimization, the number of coefficients was increased to six, while steps 2, 3, and 4 were repeated. The optimized six coefficients then gave satisfactory convergence. (During optimization the number of coefficients was increased to eight. The result showed, however, poor convergence.)

### 3.2.4. Results and Discussion

The rejection of selected experimental data sets from those listed in tables 3-2, 3-3 and 3-4 was executed during the optimization procedure. After optimization, the percent of error of each data point (defined as  $(M_{opt} - M_{exp}) \times 100 / M_{opt}$ ) calculated

by the program was carefully examined. If the percent of errors of a certain data group were found to be very large (by 100 %) compared to the other groups, they were discarded for the next run. Although some data did not appear drastically different from others, they were omitted if their inclusion yielded a poor convergence and the predicted phase diagram was unsatisfactory.

The final set of coefficients for the *Ga-As* system is listed in table 3-5. The calculated phase diagram is shown in figure 3-6 along with all of the experimental phase diagram data. The calculated melting temperature is 1237.75 °C, which agrees very well with the optimized value (1237.85 °C) by Chatillon *et al.* (88). Figure 3-7 shows the calculated enthalpy of mixing at 1300 °C along with the experimental data. Though there is only one experimental data set for the enthalpy of mixing, it seems that they are fully consistent with the calculated values. More importantly, it was found that the partial Gibbs energies calculated using activity values obtained in this work showed good consistency with the selected data sets. The other two emf data (85, 86) were found to be erroneous, giving poor convergence and large percent of error during optimization. The activity of *Ga* along the liquidus line (gallium-rich region) obtained by the optimization with the selected data sets is shown in figure 3-8 along with that obtained by this experiment and those of others in the literature.

### 3.2.5 Conclusions

An optimization of the thermodynamic properties and phase diagrams of the *Ga-As* system was performed. In the current study, two terms in the Redlich-Kister expression for the excess Gibbs energy of the liquid have been used. The partial

Table 3-5. Thermodynamic Description of the Ga-As System using the Redlich-Kister Model for the Liquid Phase.

Optimized Coefficients for the Solid GaAs in Equation (3.18)			
Phase	Compound	Coefficients	
		$a(J/g\ atom)$	$b(J/g\ atom\ K)$
Solid	GaAs	-45618.6	-8.66357
Excess Terms of the Liquid Phase in Equation (3.19) (Redlich-Kister Model) <sup>(a)</sup>			
$x$ -Multipliers		$T$ -Multipliers	
		$A_{GaAs}^{(\nu)}(J/mol)$	$B_{GaAs}^{(\nu)}(J/mol\ K)$
$x_{Ga}(1 - x_{Ga})$		-27583.1	2.80801
$x_{Ga}(1 - x_{Ga})(2x_{Ga} - 1)$		11340.6	5.87674

(a) These values were adjusted by the least squares method.

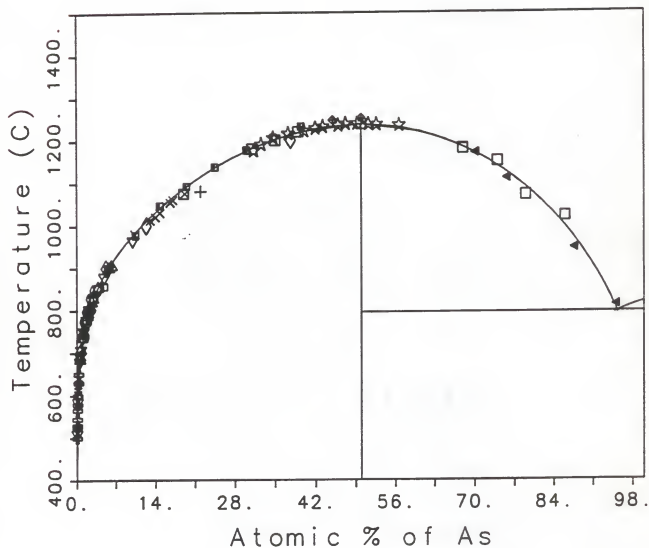


Figure 3-6. The optimized *GaAs* phase diagram.  $\circ$ ; Sol *et al.* (102),  $\square$ ; Köster and Thoma (101),  $\Delta$ ; Hsieh (103),  $\nabla$ ; Hall (100),  $\diamond$ ; Rubenstein (104),  $\star$ ; Rakov *et al.* (105),  $+$ ; Vidorovich *et al.* (106),  $\times$ ; Perea and Fonstad (107),  $*$ ; DeWinter and Pollack (108),  $\oplus$ ; Dutartre (109),  $\triangleleft$ ; Ceolin *et al.* (110).

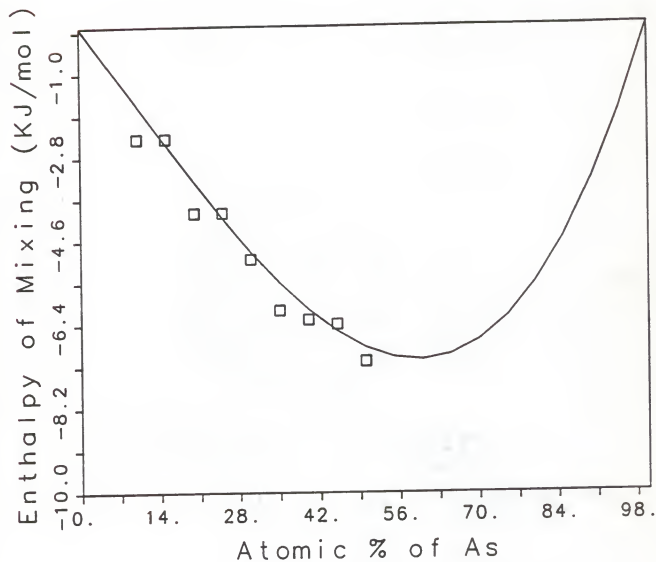


Figure 3-7. The optimized enthalpy of mixing at 1300 °C. □: Yamaguchi *et al.* (126).

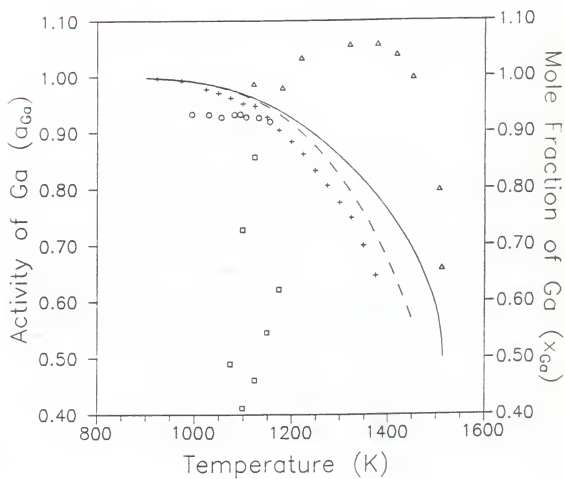


Figure 3-8. The optimized activity of gallium along the liquidus line. ---: optimized value, \_\_\_\_: ideal, +: this work,  $\square$  Wypartowicz and Fitzner (85),  $\circ$  Katayama *et al.* (86), and  $\triangle$  Arthur (98).



Gibbs energy of gallium along the liquidus line in gallium arsenide liquid, obtained from the activity measurement, were included in the optimization. Results showed very good consistency of our data with other selected data. This optimization has yielded a very consistent set of data for the *Ga-As* system and the coefficients obtained from this optimization provided an excellent fit to the phase diagram and the enthalpy of mixing data.

## CHAPTER 4

### POINT DEFECT STRUCTURE AND IMPURITY INCORPORATION IN BULK GaAs

Impurity and native point defects in crystals have been studied for the last two decades by many researchers, but a full understanding of their chemistry and influence on properties as a function of processing conditions is not known, even for well studied materials such as *Si* and *GaAs*. It is known that point defects play a key role in most mechanisms for diffusion and greatly influence the electrical properties of semiconductors. Defects in general can be divided into four groups based on their dimensionality. Defects of zero dimension (point defects) include vacancies, interstitials, and substitutional defects. Impurities in crystals are classified in this group. Point defects can be further classified according to elementary atomic, electronic and complex defects. One dimensional defects such as dislocations or line defects are large continuous array of point defects. There are gross, two dimensional defects such as slip and twin planes, which occur along one or more planes in the crystal. Finally, there are three dimensional defects such as voids and inclusions.

In this chapter, the focus is on point defects rather than dislocations or gross defects because point defects are always present (thermodynamically stable) and

strongly affect the electrical and optical characteristics of semiconductor materials while higher order defects are not stable and can be reduced or eliminated by effective crystal growth. After an introduction to the point defect chemistry of GaAs, a model of the native point defect structure of GaAs is reviewed. Incorporation of boron, which is a major isoelectronic impurity in GaAs grown in the presence of a boron oxide encapsulant, and its electrical behavior is also discussed briefly. Later in this chapter, a model is presented for incorporation of Si during melt growth.

#### 4.1 Introduction to point defects in GaAs

The vacancy is an atomic point defect in a crystal. This defect is produced when an atom located on a normal lattice site migrates to the surface to leave behind a vacant lattice site. In a compound both cation and anion atoms can reach the surface in stoichiometric amounts to create Schottky disorder. A second elementary atomic point defect is the interstitial. Such a defect occurs when an atom is placed in the interstitial void within the crystal structure. It is obvious that the energy of formation of an interstitial defect is relatively large in a closed-packed crystal structure, but the energy can be relatively small in loosely packed crystal structures such as the diamond and zinc blende structure. The maximum proportion of space which may be filled by hard spheres arranged in the closed-packed crystal structures, (*i.e.*, face centered cubic or hexagonal closed-packed) is 0.74 and that in the diamond and zinc blende structures is 0.34. The extra atom in an interstitial site in the crystal structure causes stress in the lattice and displacement of native atoms from their equilibrium position. Frenkel disorder is a combination of a vacancy and an

interstitial in a way that overall charge neutrality prevails. The interstitial is usually in the vicinity of the newly formed vacancy, so that the energy of formation of Frenkel defects is comparable to that of interstitial defects.

Impurity atoms can also incorporate in crystals to form elementary point defects. Impurity atoms can sit in interstitial sites as well as substitute for host atoms in the lattice. Substitutional impurities from neighboring columns of the periodic table are usually thermally ionized (but not always) and, at high concentrations, determine the conductivity type. Interstitial impurities, on the other hand, are often electrically inactive. The possibility of impurity atoms or their ions residing in an interstice depends on the size of the foreign species. Atoms which are in the same or adjacent columns in periodic table to the native atoms in the crystal tend to occupy substitutional sites. In a semiconductor, electrons and holes can be introduced into the conduction and valence bands, respectively, by the thermal ionization of impurity atoms from adjacent columns. These electrons and holes can be considered electronic defects relative to the perfect crystal.

The different kinds of significant native point defects in gallium arsenide are much larger than in an elementary semiconductor such as silicon or germanium. For example, there are four possible types of interstitials in *GaAs* because either a gallium or an arsenic atom can be interstitially located in a gallium or an arsenic void. The anti-structure or anti-site defect (gallium atom is located on an arsenic site or vice versa) is possible in *GaAs* and not in *Si* or *Ge*. Also, Schottky defects may exist as the equal number of gallium and arsenic vacancies, and four kinds of Frenkel

pairs are possible, depending on the type of atom and type of void into which it is displaced. Simplified defects in the gallium arsenide two dimensional crystal structure are shown in figure 4-1. Studying the native defect structure experimentally is difficult for several reasons. First, the electrical properties of *GaAs* can change considerably with temperature and gallium or arsenic partial pressure. Also, the native defects can react with impurities in the crystal to form complexes. Possible native defects and complexes in gallium arsenide are listed in table 4-1 and table 4-2.

#### 4.2 Review of Models of the Native Point Defect Structure in GaAs

Since the comprehensive study by Hurle (33), there have been several studies on the nature of native point defects in *GaAs*. In this section, these recent models of the native defect structure, the identity of the EL2 center and its dependence on the melt stoichiometry, and the after-growth thermal annealing of *GaAs* are reviewed.

##### 4.2.1. Models of the Native Point Defect Structure in GaAs

An equilibrium description of the native point defect structure of *GaAs* was first proposed by Logan and Hurle (128). They assumed that the Schottky disorder was dominant defect. Later measurements (34, 129) of the density and lattice parameter of *GaAs* prompted modification of this model. Bublik *et al.* (34) and Driscoll and Willoughby (129) measured the density and the lattice parameter of melt grown *GaAs* as a function of composition. Their results indicated that arsenic interstitials were a major native point defect. It was also found by Hall measurement

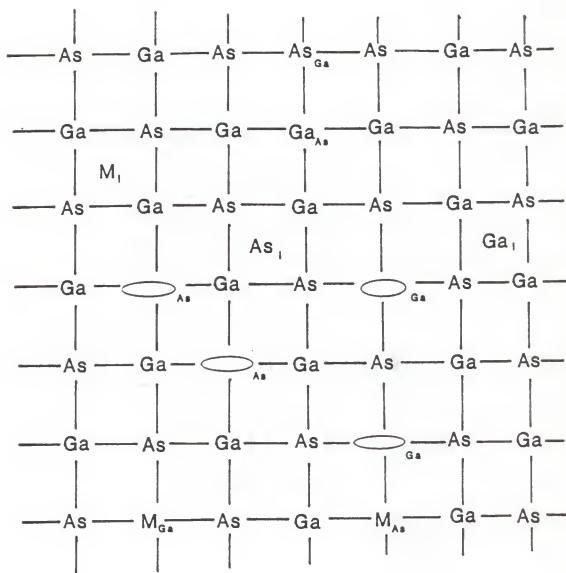


Figure 4-1. Elementary atomic point defects in *GaAs*, idealized 2-dimensional structure.  $\bigcirc_{\text{As}}$   $\bigcirc_{\text{Ga}}$ : As, Ga vacancy.  $\text{M}_i$ ,  $\text{Ga}_i$ ,  $\text{As}_i$ : Impurity, gallium, arsenic interstitial.  $\text{Ga}_{\text{As}}$ ,  $\text{As}_{\text{Ga}}$ : Antisite defect.  $\text{M}_{\text{Ga}}$ ,  $\text{M}_{\text{As}}$ : Impurity at gallium, arsenic site

Table 4-1. Some Possible Complex Point Native Defects in GaAs

Gallium Vacancies Involved	Arsenic Vacancies Involved	Antisite Defects	Interstitials Involved	Three Component Defects <sup>(a)</sup>
$V_{Ga}$	$V_{As}$	$Ga_{As}$	$Ga_i$	
$V_{Ga}V_{Ga}$	$V_{As}V_{As}$	$As_{Ga}$	$As_i$	
$V_{Ga}V_{As}$	$V_{Ga}V_{As}$		$Ga_iAs_i$	
		$Ga_{As}As_{Ga}$		
$Ga_iV_{Ga}$			$Ga_iV_{Ga}$	
	$As_iV_{As}$		$As_iV_{Ga}$	
$Ga_{As}V_{Ga}$		$Ga_{As}V_{Ga}$		
	$Ga_{As}V_{As}$	$Ga_{As}V_{As}$		
$As_{Ga}V_{Ga}$		$As_{Ga}V_{Ga}$		
	$As_{Ga}V_{As}$	$As_{Ga}V_{Ga}$		
	$Ga_iV_{As}$		$Ga_iV_{As}$	
$As_iV_{Ga}$			$As_iV_{Ga}$	
				$V_{Ga}V_{As}V_{Ga}$
				$V_{Ga}As_{Ga}V_{Ga}$
				$V_{As}Ga_{As}V_{As}$

(a) : Many other defects are possible in addition to the three listed in the table.

Table 4-2. Some Hypothetical Complexes Between Native Defects and Elemental Impurities in GaAs<sup>(a)</sup>.

Group II Impurities <sup>(b)</sup>	Group IV Impurities <sup>(c)</sup>	Group VI Impurities <sup>(d)</sup>	Transition Impurities <sup>(e)</sup>
$A_{Ga}$	$M_{Ga}$	$D_{Ga}$	$T_{Ga}$
$A_{As}$	$M_{As}$	$D_{As}$	$T_{As}$
$A_{Ga}V_{As}$	$M_{Ga}V_{As}$	$D_{Ga}V_{As}$	$T_{Ga}V_{As}$
$A_{Ga}V_{Ga}$	$M_{Ga}V_{Ga}$	$D_{Ga}V_{Ga}$	$T_{Ga}V_{Ga}$
$A_{Ga}Ga_{As}$	$M_{Ga}Ga_{As}$	$D_{Ga}Ga_{As}$	$T_{Ga}Ga_{As}$
$A_{Ga}As_{Ga}$	$M_{Ga}As_{Ga}$	$D_{Ga}As_{Ga}$	$T_{Ga}As_{Ga}$
$A_{Ga}A_{As}$	$M_{Ga}M_{As}$	$D_{Ga}D_{As}$	$T_{Ga}T_{As}$
$A_{As}V_{As}$	$M_{As}V_{As}$	$D_{As}V_{As}$	$T_{As}V_{As}$
$A_{As}V_{Ga}$	$M_{As}V_{Ga}$	$D_{As}V_{Ga}$	$T_{As}V_{Ga}$
$A_{As}Ga_{As}$	$M_{As}Ga_{As}$	$D_{As}Ga_{As}$	$T_{As}Ga_{As}$
$A_{As}As_{Ga}$	$M_{As}As_{Ga}$	$D_{As}As_{Ga}$	$T_{As}As_{Ga}$

- No defects involving interstitials have been listed or defects involving three components.
- $A = Be, Mg, Zn, Cd$
- $M = C, Si, Ge, Sn$
- $D = O, S, Se, Te$
- $T = Ti, V, Cr, Mn, Fe, Co, Ni, Cu$



at high temperature that the conductivity was dominated by charged native point defects rather than thermally generated electron-hole pairs. Based on these results, Hurle (33) proposed that Frenkel defects are the major disorder in GaAs rather than Schottky defects. In addition to Frenkel defects, the electron/hole pair equilibrium was, of course, included in the model. The point defects were then allowed to interact with the external phase (*e.g.*,  $As_2$ ). The model was completed by requiring electrical neutrality. An independent set of reactions and the corresponding equilibrium constants amongst these species are:

$$As_{As} + V_i = As_i + V_{As}, \quad K_{fa} = \frac{[V_{As}][As_i]}{[V_i][As_{As}]} \quad (4.1)$$

$$0 = e^- + h^+, \quad K_{cv} = np \quad (4.2)$$

$$As_i = As_i^+ + e^-, \quad K_{ai} = \frac{[As_i^+]n}{[As_i]} \quad (4.3)$$

$$V_{As} = V_{As}^+ + e^-, \quad K_{av} = \frac{[V_{As}^+]n}{[V_{As}]} \quad (4.4)$$

$$\frac{1}{2}As_2(g) + V_i = As_i, \quad K_{As_2i} = \frac{[As_i]}{[V_i]^{1/2}P_{As_2}^{1/2}} \quad (4.5)$$

where  $K$ 's are the equilibrium constants for these reactions. The electroneutrality condition amongst the charged species is

$$n = p + [V_{As}^+ ] + [As_i^+ ] \quad (4.6)$$

In this model, the concentrations of gallium vacancies, interstitials and antisite defects ( $Ga_{As}$  or  $As_{Ga}$ ) were assumed small in comparison to the concentrations of other defects.

In his paper, Hurle (33) reviewed some important experimental work to justify his choice of dominant species at elevated temperatures. The measurement of lattice parameter by Driscoll and Willoughby (129) showed that the change in lattice parameter as a function of melt composition (in the range 50.5 to 56 at. % As in the melt) was on the order of  $\sim 10^{-6}$ , implying the presence of either arsenic interstitials or of antisite defects. Later, Bublik *et al.* (34) found that the lattice parameter was constant to within 5 parts in  $10^6$  over the range of melt composition (46.7 to 53.5 % As) and the density increased linearly with melt composition. By determining the differential number of point defects in the sample from the density and lattice parameter data, they obtained a result which was in good agreement with the results of Driscoll and Willoughby (129). Based on these observations, Hurle interpreted their results as being due to arsenic Frenkel defects because the lattice parameter did not change as a function of melt composition yet the density increased as the As melt concentration ( or arsenic partial pressure in the model) increased. High temperature Hall data (130-132) showed that carrier concentration for LPE and VPE material was larger than the intrinsic value (Eq. 4.2) above 500-600 K. Thus, Hurle inferred that there was a high concentration of ionized arsenic vacancies on the Ga-rich side of the single phase field but that the concentration of ionized arsenic

interstitials in undoped material on the *As*-rich side was considerably smaller, implying that the charged native defect dominated the electrical behavior at high temperature.

Using experimental data from the literature, values of the equilibrium constants were estimated. With these constants, Hurle predicted a significant extent of the *GaAs* solid field at or just below the melting temperature. The analysis proposed that *GaAs(s)* has a broad range of melt composition around the melting point and a high concentration of gallium and arsenic point defects are likely to form during growth from the melt. It is also noted that the congruent melting point is slightly shifted to the *Ga*-rich side of the stoichiometric composition. More recently, Inada *et al.* (133) investigated the solidus curve on the *As*-rich side of the *Ga-As* system and showed that the solidus line was a parabolic shape and the congruent point was shifted from the stoichiometric composition by 0.00003 at. % toward the *As*-rich side. Their results were obtained assuming that  $[EL2]_{max}$  corresponded to the concentration of the excess dissolved *As* atoms and that EL2 formation reaction involved one excess *As* atom.

The kinetics of defect reactions are difficult to assess (*e.g.*, change upon cooling from growth temperature to room temperature). Based on the lattice parameter results, which showed a nearly constant lattice parameter across the phase extent on cooling, Hurle suggested that excess  $V_{As}$  precipitate out of solution on a scale which is coarse enough so that they no longer affect the X-ray measured lattice

parameter. This precipitation is expected to be to internal sinks rather than to the free crystal surface.

#### 4.2.2. EL2 in GaAs

The semi-insulating behavior of undoped *GaAs* has been attributed to the EL2 deep donor level and the concentration of the EL2 defect was found to depend on the crystal stoichiometry, increasing with increasing arsenic composition (41, 134). Uncompensated residual acceptors, usually carbon impurities, are responsible for the p-type behavior and low resistivity of crystals pulled from the *Ga*-rich melts. The higher resistivity and n-type *GaAs* can be obtained above a critical arsenic composition. For instance, a slightly arsenic-rich melt ( $[Ga]/[As] = 0.98$ ) produces uniformly, n-type and highly resistive material over the full length of the crystal. On the other hand, a gallium-rich melt ( $[Ga]/[As] = 1.2$ ) or a near stoichiometric gallium-rich melt produces low resistivity, p-type material. The transition from n-type high resistivity behavior to low resistivity behavior occurs at a gallium-rich composition of about 0.53 atomic fraction gallium ( $[Ga]/[As] > 1.13$ ).

The defect(s), which is(are) responsible for EL2 level, has(have) not been clearly identified yet and is still the subject of investigation (135, 136-141). The sublinear dependence of EL2 concentration on the oxygen content in the sample discounted the association of EL2 with an oxygen midgap level (142). Holmes *et al.* (41, 134) suggested that the EL2 level involved native point defects such as  $As_{Ga}$  or  $V_{Ga}$  based on their optical absorption coefficient study. In their study, the EL2 absorption dropped abruptly as the solid composition moved from the arsenic to the

gallium-rich side, which was presumably due to a corresponding reduction in the concentration of EL2 deep donor level. Lagowski *et al.* (143) also suggested that the EL2 deep donor is associated with  $As_{Ga}$  native defect based on their electron paramagnetic resonance measurements and shallow donor doping experiments in Bridgman grown  $GaAs$ . There are two different models proposed for the formation of EL2 level. Figielski (144) and Aref'ev *et al.* (145) suggested that EL2 ( $As_{Ga}$ ) level is grown-in during the growth from the melt. On the other hand, Lagowski *et al.* (143) proposed a two step process for the formation of the EL2 level. The first step was the formation of a gallium vacancy ( $V_{Ga}$ ) in the crystal lattice during growth, and the second step was an interaction of this vacancy with an arsenic atom during post-growth cooling/annealing to form  $As_{Ga}$  antisite defect. Later Hurle (146) put forward the suggestion by Morrow (147) that EL2 centers must arise as a result of some annihilation reaction, and concluded that the very strong dependence of the concentrations of a double acceptor "A" (probably  $Ga_{As}$ ) and the EL2 on arsenic concentration of the melt found by Holmes *et al.* (41) could not be accounted for by a "grown-in" model. In addition Hurle (146) proposed a point defect model which included the deep double acceptor "A" with the defect  $Ga_{As}$  and EL2 with  $As_{Ga}$  and fitted the data of Holmes *et al.* (41) to this model, showing good agreement. However, he did not rule out the possibility of the EL2 being a complex such as  $As_{Ga}As_i$  or  $As_{Ga}V_{As}$ . Though it is most accepted that EL2 is a simple  $As_{Ga}$  antisite defect, there are still various suggestions about the formation and identity of the EL2. For instance, while the EL2 was assigned to the antisite defect complex  $As_{Ga}-$

$V_{As}$  by Lagowski *et al.* (148),  $As_{Ga}-As_i$  was identified as EL2 by Bardeleben *et al.* (149) and Bourgoin *et al.* (150).

#### 4.2.3. Effect of Thermal Treatment on the EL2 Center

Hurle (33) predicted theoretically a significant extent of the gallium arsenide solid field at or just below the melting temperature as shown in the phase diagram in figure 4-2. Gallium arsenide has a broad range of melt compositions around the melting point and the high concentration of gallium or arsenic point defects are likely to form during growth from the melt. Liquid phase epitaxy operates at relatively lower temperatures ( $\sim 750^\circ\text{C}$ ) where the extent of solid solution is much narrower, resulting in nearly exact stoichiometric solid compositions. The idea of thermal treatment of gallium arsenide after growth lies in the fact that thermal annealing at lower temperatures can modify and reduce the defect content in the melt grown gallium arsenide crystals. In the conventional thermal conversion annealing procedure, samples are encapsulated by a 900 Å thick, low temperature plasma silicon nitride and subjected to annealing at about  $860^\circ\text{C}$  in forming gas. Experiments showed that only the substrates with the stoichiometric or arsenic-rich compositions had high thermal stability, but as the gallium composition, annealing time, and annealing temperature increased, the sheet resistance decreased and conduction became p-type (151). Therefore, only *GaAs* substrates with *Ga* compositions below 51.5 % atomic fraction can be used for implantation device processing (*i.e.*, yield  $\geq 10^7 \Omega/\text{sq.}$ , n-conduction after a standard  $860^\circ\text{C}/15\text{-min}$  encapsulated anneal).

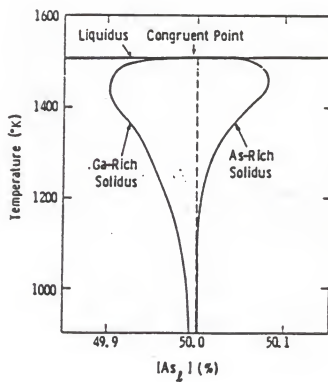


Figure 4-2. Predicted GaAs solidus curve (33).

The effects of deep levels in semi-insulating gallium arsenide have already been discussed in the previous section. When undoped gallium arsenide substrates of near-stoichiometric compositions are subjected to thermal annealing the predominant surface phenomenon conversion occurs. This conversion occurs when the EL2 concentration at the surface falls below the residual acceptor concentration. Thermal conversion effects in undoped LEC gallium arsenide are governed mainly by out-diffusion of gallium and/or arsenic defects to the surface, a phenomenon first observed by DLTS in VPE gallium arsenide layers (152) and from *Se*-doped LEC gallium arsenide pulled from fused silica crucibles (153). Based on these facts, the diffusion kinetics of the EL2 defect level is responsible for thermal conversion effects in undoped, semi-insulating LEC gallium arsenide. Near-stoichiometric substrates showed limited conversion within the surface region, while gallium-rich substrates show conversion over large depth. Figure 4-3 shows a model of the influence of stoichiometry and out-diffusion on thermal stability. It has been known that the stoichiometry of the melt controls EL2 levels in the crystal. In the near surface region, however, an alteration in the stoichiometry of the solid occurs under thermal treatment, and consequently the concentration of the EL2 level changes. Since gallium arsenide crystals pulled from gallium-rich melts ( $[Ga]/[As] \geq 1.13$ ) have a low concentration of the EL2 deep donor level (below the concentration of residual acceptor level), these crystals with low resistivity and p-type conduction are not dependent on post-growth thermal treatments (figure 4-3 (a)). Gallium arsenide grown from the stoichiometric melt ( $[Ga]/[As] \geq 1$ ) exhibits semi-insulating behavior,



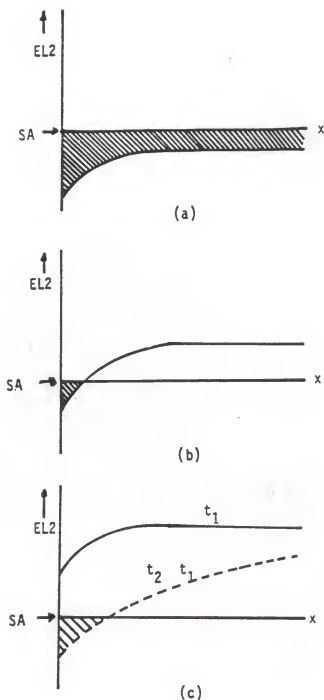


Figure 4-3. Schematic representation of the influence of stoichiometry and out-diffusion on the thermal stability of undoped, semi-insulating *GaAs* by compensation of residual shallow acceptors (SA) by deep-donor level (EL2). (a) p-type bulk with  $Ga/As \gg 1$ , (b) p-type skin with  $Ga/As \geq 1$ , (c) n-type semi-insulating with  $Ga/As \leq 1$ .

and if subjected to sufficiently long thermal treatment that is employed commonly in implantation processing, the concentration of defect related to deep donors in the near surface region is reduced and the thermal conversion occurs (figure 4-3 (b)). Undoped semi-insulating gallium arsenide from the stoichiometric or arsenic-rich melt ( $[Ga]/[As] \leq 1$ ) maintains high surface sheet resistance (typically  $>10^7 \Omega/sq.$ ) under standard implantation annealing conditions ( $860^\circ C/15 \text{ min.}$ ). However, as the annealing time increases, the concentration of deep donor levels reduces, and finally p-type conversion occurs (figure 4-3 (c)).

#### 4.3 Incorporation of Isoelectronic Dopants in GaAs

As shown in chapter 2, boron is one of the main impurities in *GaAs* crystal grown with a  $B_2O_3$  encapsulant. Presumably the main source of boron contamination is the  $B_2O_3$  encapsulant. The incorporation of boron has been shown to depend on the water content of the encapsulant, with the boron concentration decreasing as the water content increases (see table 2-3) (70, 71).

Little is known about the behavior of boron in *GaAs*. Boron belongs to the group III column of the periodic chart and has the same number of valence electrons as gallium. When boron occupies the gallium site ( $B_{Ga}$ ) in *GaAs*, it is not electrically active. Though boron incorporation on a gallium site may produce strains and reduce carrier mobilities, its effect on device performance should not be significant. However, when boron occupies a arsenic site ( $B_{As}$ ) it is electrically active as a double acceptor. Gledhill *et al.* (154) found electron irradiated *GaAs* had local vibration mode (LVM) lines at  $601$  and  $628 \text{ cm}^{-1}$  that were due to the single-negative-charge

state of the two isotopes of boron on arsenic site ( $B_{As}$ ). Later, Fischer and Yu (155) performed infrared absorption and photoluminescence measurements on a series of as-grown p-type  $GaAs$  crystals grown by the LEC technique from  $Ga$ -rich melts. They observed a rather high boron impurity concentration. All their samples had measurable boron concentrations at the gallium site ( $B_{Ga}$ , LVM lines at  $517\text{ cm}^{-1}$ ), and two of their samples had boron-antisite concentrations ( $B_{As}$ , LVM at  $601\text{ cm}^{-1}$ ). They also showed the presence of a double acceptor in the PL spectra of these materials. Emission lines occurred at 1.441 and 1.351 eV which were due to the 78 and 204 meV levels, respectively (156-158). The 204 meV level appeared to be the only one of the two associated with the double acceptor. However, a correlation between boron concentration and double acceptor concentration (combination of 78 and 204 meV levels) suggested that there may be the possibility that the double acceptor was a complex involving an isoelectronic boron impurity atom (e.g.,  $Ga_{As}B_{Ga}$ ).

Moore and Hawkins (159) investigated the conditions under which boron on the arsenic site was introduced during irradiation with 2 MeV electrons. Monitoring the strength of the  $B_{As}$  LVM and the position of the Fermi level as determined by the presence of 1S-2P transitions of acceptor impurities with binding energies ranging from 27 to 203 meV, they suggested a model for the formation of  $B_{As}$  in electron irradiated  $GaAs$ . They observed that (1) compensation of 203 meV acceptors (possibly  $Ga_{As}^-$  centers are compensated by the deep donors produced by irradiation) proceeded linearly with fluence, but the rate was a function of the Fermi level, and

(2) formation of  $B_{As}$  LVM proceeded linearly with fluence with a threshold corresponding to the movement of the Fermi level above 78 meV. Based on these observations, it was suggested that the process which produced boron on the arsenic site was not effective when the Fermi level lay at or below 78 meV and only became effective when the Fermi level rose to a value, as yet undetermined, between 78 and 203 meV. A Fermi level dependent diffusion rate for boron, which is known to be present in silicon (160), seemed to be responsible for the dependence of this process (i.e., the diffusion of boron in *GaAs* is inhibited when the Fermi level is low). In that case, the primary damage (e.g., arsenic vacancy) could anneal before a diffusing boron atom could occupy it. Rapid diffusion of boron after the Fermi level rises could allow boron to occupy some significant fraction of arsenic vacancies prior to the annealing of the vacancies.

Though there has been some progress in understanding the incorporation of boron in *GaAs* crystals, there still remain many questions about the electrical behavior of boron in *GaAs* crystals. There have been conflicting reports in the literature on whether the boron antisite ( $B_{As}$ ) exists in as-grown material and whether luminance measurements have identified one or more defect levels in the 200 to 230 meV range (157, 158). Also it is still not clear whether the double acceptor levels found at 78 and 203 or 204 meV have anything to do with the presence of  $B_{As}$ . These questions need to be answered to produce crystals with the desired electrical properties on which the device performance is dependent.

#### 4.4 Model for Si-Incorporation in GaAs

Silicon is an important impurity in gallium arsenide crystal growth because of its amphoteric behavior in III-V semiconductors. It has long been known that silicon acts as a shallow donor when it takes a gallium site and creates a substitutional point defect,  $Si_{Ga}^+$ . On the other hand, it acts as an acceptor,  $Si_{As}^-$ , when it takes an arsenic site. The donor site is preferred under the stoichiometric conditions of growth, while p-type gallium arsenide can be grown only by the liquid phase epitaxy from a gallium-rich solution at a relatively low temperature. An unintentional doping of gallium arsenide with silicon can occur during crystal growth, especially when a silica container is used. If the silica container is used in LEC or Bridgman growth, interaction between the silica and the melt or arsenic vapor causes the dissolution of silicon, and consequently the incorporation of silicon into gallium arsenide. Silicon behavior in gallium arsenide has been studied by many investigators (161-164), but it is still not possible to accurately control its incorporation.

Teramoto (165, 166) calculated the solid solubility isotherms for amphoteric silicon in gallium arsenide as a function of silicon concentration along the gallium-arsenic-silicon liquidus isotherms. In his work, the temperature dependent equilibrium constants for the incorporation of silicon in gallium arsenide were obtained by evaluating the Gibbs energy change involved in the transfer of silicon atoms from the arsenic to the gallium sublattice. He also developed a chemical equilibrium model of silicon incorporation in gallium arsenide (165), in which he approximated the electroneutrality condition to two of its dominant species

depending on the temperature and activity in the liquid to solve his thermochemical model of solid solubility of silicon in gallium arsenide. However, Hurle (33) proved in his study of point defect equilibria and non-stoichiometry in gallium arsenide, that the application of Brouwer's approximation to the electroneutrality condition by its two dominant members (*i.e.*, the equilibrium relations can be solved analytically for the regimes;  $n = p$ ,  $n = [V_{As}^{+}]$ , and  $n = [As_i^{+}]$ ) could lead to an invalid solution at high temperature close to melting point. It was also found (33) that the dominant disorder in gallium arsenide was Frenkel defect formation on the arsenic sublattice with an arsenic vacancy exhibiting donor-like behavior at high temperature instead of Schottky disorder previously suggested by Logan and Hurle (128). Hurle (33) also obtained equilibrium constants from a compilation of a priori estimates and fitting of experimental data.

In the next sections, an equilibrium model of silicon incorporation in melt grown gallium arsenide will be discussed. Existing data will be used to estimate some equilibrium constants at the melting temperature. These calculated values are used to predict the incorporation of silicon in melt-grown gallium arsenide with the assumptions that the melt is cooled so slowly that thermal equilibrium with the solid phase is maintained and that the growth period is also very short so that the growth temperature is virtually unchanged.

#### 4.4.1. Chemical Equilibrium Model for Si Incorporation

As in the previous work (166), the standard procedures of equilibrium thermodynamics are used to derive expressions for the equilibrium concentrations of

the various defects considered. Hurle (33, 167-170) has proposed models for native defects in gallium arsenide and for *Te*, *Sn* and *Ge* doped gallium arsenide. These models are extended here to account for the doping of gallium arsenide with silicon. This defect model includes arsenic Frankel defect as well as Schottky disorder. Silicon is allowed to take either on the gallium or arsenic sublattice and is excluded from the interstitial sites. Furthermore, silicon atoms can form complex defects such as  $Si_{Ga}Si_{As}$  or  $Si_{Ga}V_{Ga}$ . The presence of  $Si_{Ga}Si_{As}$  complex defects was observed by LVM measurements (171) and that of  $Si_{Ga}V_{Ga}$  was suggested by several researchers (172-174) based on the compensation ratio of Si-doped *GaAs*. A set of independent formation reactions for neutral species is shown below.

$$\frac{1}{2}As_2(g) + V_i = As_i \quad (4.7)$$

$$As_{As} + V_i = As_i + V_{As} \quad (4.8)$$

$$0 = V_{Ga} + V_{As} \quad (4.9)$$

$$Si_i + V_{Ga} = Si_{Ga} \quad (4.10)$$

$$Si_i + V_{As} = Si_{As} \quad (4.11)$$

The notation used here is consistent with that of Hurle (170). For example, equation (4.7) represents the reaction that an arsenic dimer in the vapor phase and a vacant interstitial site in gallium arsenide produce an arsenic interstitial. Thus, in the solid state, a subscript represents the site where an atom is residing.  $Si_i$  in equations (4.10) and (4.11) represents silicon in the melt. Equation (4.8) accounts for arsenic Frenkel

defect on the arsenic sublattice. The concentrations of Frenkel disorder on the gallium sublattice and anti-site defects are assumed to be small compared to the concentrations of arsenic vacancies and arsenic interstitials based on the fact that Hurle (33) has found the dominant disorder in gallium arsenide during growth is Frenkel disorder on the arsenic sublattice. Schottky defect formation is accounted for by equation (4.9).

The interstitial species are assumed to remain electrically neutral while other defects may ionize. The following set of formation reactions may be written to represent the ionized species.

$$V_{As} = V_{As}^{+} + e^{-} \quad (4.12)$$

$$V_{Ga} = V_{Ga}^{-} + h^{+} \quad (4.13)$$

$$0 = e^{-} + h^{+} \quad (4.14)$$

$$Si_I + V_{Ga} = Si_{Ga} = Si_{Ga}^{+} + e^{-} \quad (4.15)$$

$$Si_I + V_{As} = Si_{As} = Si_{As}^{-} + h^{+} \quad (4.16)$$

$$Si_{Ga}^{+} + V_{Ga}^{-} = Si_{Ga}V_{Ga}^{-} + h^{+} \quad (4.17)$$

$$Si_{Ga}^{+} + Si_{As}^{-} = Si_{Ga}Si_{As} \quad (4.18)$$

Equations (4.12) and (4.13) represent the ionizations of native point defects while equations (4.15) and (4.16) the amphoteric behavior of silicon. The generation and



recombination of electrons and holes are illustrated by equation (4.14) and the silicon complex formations by equations (4.17) and (4.18). Assigning donor type to the arsenic vacancy is based on the following facts:

- (a) the expectation that all group V vacancies will form donors (166) in the zinc-blend lattice,
- (b) the high temperature Hall coefficient data which suggests that at high temperature and away from the arsenic rich solidus, the electron concentration in gallium arsenide is much greater than the intrinsic electron concentration, and
- (c) the calculation by (i) Jaros (175) which indicates that arsenic vacancies should form shallow singly-ionized donors, whereas the gallium vacancies were acceptors (176), (ii) Il'im and Masterov (177) who concluded that the arsenic vacancy could be regarded as a donor with an electron activation energy of 0.25 eV.

An electroneutrality condition is all that is needed to complete the model

$$n + [V_{Ga}^-] + [Si_{As}^-] + [Si_{Ga}V_{Ga}^-] = p + [Si_{Ga}^+] + [V_{As}^+] \quad (4.19)$$

where [ ] denoted concentration, and  $n$  and  $p$  represent electron and hole concentrations, respectively.

The equilibrium relations corresponding to above reactions (4.7)-(4.18) are as follows, except equations (4.10) and (4.11) which are combined in equations (4.15) and (4.16).

$$K_1 = [As_i]P_{As_2}^{-\frac{1}{2}} \quad (4.20)$$

$$K_2 = [As_i][V_{As}] \quad (4.21)$$

$$K_3 = [V_{Ga}][V_{As}] \quad (4.22)$$

$$K_6 = \frac{\gamma_n[V_{As}^+]^n}{[V_{As}]} \quad (4.23)$$

$$K_7 = \frac{\gamma_p[V_{Ga}^-]p}{[V_{Ga}]} \quad (4.24)$$

$$K_8 = \gamma_n \gamma_p n p \quad (4.25)$$

$$K_9 = \frac{\gamma_n[Si_{Ga}^+]^n}{[V_{Ga}]\gamma_{Si}[Si_i]} \quad (4.26)$$

$$K_{10} = \frac{\gamma_p[Si_{As}^-]p}{[V_{As}]\gamma_{Si}[Si_i]} \quad (4.27)$$

$$K_{11} = \frac{\gamma_p[Si_{Ga}V_{Ga}^-]p}{[Si_{Ga}^+][V_{Ga}^-]} \quad (4.28)$$

$$K_{12} = \frac{[Si_{Ga}Si_{As}]}{[Si_{Ga}^+][Si_{As}^-]} \quad (4.29)$$

where  $K$ 's are equilibrium constants, and  $\gamma_n$ ,  $\gamma_p$ , and  $\gamma_{Si}$  are the activity coefficients of the electron, hole, and silicon, respectively. The equilibrium constants have the form of

$$K = \exp\left(\frac{\Delta S^\circ}{k}\right)\exp\left(\frac{-\Delta H^\circ}{kT}\right) \quad (4.30)$$

$$= K_0 \exp\left(\frac{-\Delta H^\circ}{kT}\right) \quad (4.31)$$

where  $\Delta S^\circ$  and  $\Delta H^\circ$  are the standard entropy and enthalpy changes of the given reaction, and  $T$  is in Kelvin.  $P_{As_2}$  is the partial pressure of  $As_2$  in the given growth system. Provided all the values of  $K$  are known, equations (4.19)-(4.29) can be solved for the following unknowns over the region of  $P_{As_2}$ ,  $[Si_i]$ , and  $T$  within the single phase field of gallium arsenide;  $n$ ,  $p$ ,  $[As_i]$ ,  $[V_{As}]$ ,  $[V_{Ga}]$ ,  $[V_{As}^+]$ ,  $[V_{Ga}^-]$ ,  $[Si_{Ga}^+]$ ,  $[Si_{As}^-]$ ,  $[Si_{Ga}Si_{As}]$ , and  $[Si_{Ga}V_{Ga}^-]$ . Several equilibrium constants of the native point defect reactions in gallium arsenide have been estimated by theoretical or experimental methods (33, 165), and are listed in table 4-3. In the present study, it is assumed that the ternary melt of gallium-arsenic-silicon is regular, and that the activity coefficients of the constituent elements in the liquid phase may be calculated using following equations given by Prigogine and Defay (178).

$$RT \ln \gamma_{Ga} = \alpha_{Ga-As} [As_i]^2 + \alpha_{Ga-Si} [Si_i]^2 + (\alpha_{Ga-As} - \alpha_{As-Si} + \alpha_{Ga-Si}) \\ \times [As_i][Si_i] \quad (4.32)$$

Table 4-3. Equilibrium Constants for Several Native Point Defect Reactions and Silicon Incorporation

Eq. No.	Equilibrium Constant	Value at 1511 K	Ref.
3.20	$K_1 = 16.4 \exp\left(\frac{-1.12}{kT}\right)$	$3.022 \times 10^{-3}$	(33)
3.21	$K_2 = 2.92 \times 10^6 \exp\left(\frac{-4.84}{kT}\right)$	$2.124 \times 10^{-10}$	(33)
3.23	$K_6 = 442 \exp\left(\frac{-0.27}{kT}\right)$	55.609	(33)
3.25	$K_8 = 1 \times 10^{-12} T^3 \exp\left(\frac{-1.62}{kT}\right)$	$1.368 \times 10^{-8}$	(33)
3.29	$K_{12} = 1.68 \times 10^{-1} \exp\left(\frac{-0.66}{kT}\right)$	$1.058 \times 10^{-3}$	(166)

$k$  is the Boltzman's constant in  $eV/K$  and  $T$  is the absolute temperature in  $K$ .

$$RT \ln \gamma_{As} = \alpha_{As-Si} [Si]_l^2 + \alpha_{Ga-As} [Ga]_l^2 + (\alpha_{As-Si} - \alpha_{Ga-Si} + \alpha_{Ga-As}) \times [Si]_l [Ga]_l \quad (4.33)$$

and

$$RT \ln \gamma_{Si} = \alpha_{Ga-Si} [Ga]_l^2 + \alpha_{As-Si} [As]_l^2 + (\alpha_{Ga-Si} - \alpha_{Ga-As} + \alpha_{As-Si}) \times [Ga]_l [As]_l \quad (4.34)$$

where  $\alpha$  is the binary interaction parameter of the subscripted component in the liquid phase. An interaction parameter for the gallium-arsenic system was found by Arthur (98) who determined the activity coefficients along the liquidus line in the gallium arsenic system in the form of

$$\alpha_{Ga-As} = 5160 - 9.16T \quad (4.35)$$

Thurmond and Kowalchik (179) determined the interaction parameters for the silicon-gallium and silicon-arsenic systems from the ( $T$ - $x$ ) phase diagrams as

$$\alpha_{Si-Ga} = 3250 - 0.83T \quad (4.36)$$

$$\alpha_{Si-As} = -49990 + 32.40T \quad (4.37)$$

where the units of  $\alpha$  are  $cal/mol$ .

#### 4.4.2. Application of the Model to Growth of GaAs

Manipulating the equilibrium constants in equations (4.20) - (4.29), one can express the concentrations of silicon on the gallium site,  $[Si_{Ga}^+]$ , the arsenic site,

$[Si_{As}^-]$ , and the complex of silicon on the gallium site and the gallium vacancy,  $[Si_{Ga}V_{Ga}^-]$  with respect to the silicon concentration in the melt,  $[Si_i]$ . The results are as follows (for detail, see Appendix 2):

$$[Si_{Ga}^+] = K_{13} \frac{P_{As_2}^{\frac{1}{2}}}{\gamma_n^{n(gf)}} \gamma_{Si} [Si_i] \quad (4.38)$$

$$[Si_{As}^-] = K_{14} \frac{\gamma_n^{n(gf)}}{P_{As_2}^{\frac{1}{2}}} \gamma_{Si} [Si_i] \quad (4.39)$$

$$[Si_{Ga}V_{Ga}^-] = K_{15} P_{As_2} \gamma_n^{n(gf)} \gamma_{Si} [Si_i] \quad (4.40)$$

where

$$K_{13} = \frac{K_9 K_3 K_1}{K_2} \quad (4.41)$$

$$K_{14} = \frac{K_2 K_{10}}{K_1 K_8} \quad (4.42)$$

$$K_{15} = \frac{K_1^2 K_3^2 K_7 K_9 K_{11}}{K_2^2 K_8^2} \quad (4.43)$$

For melt growth,  $P_{As_2}$  is the partial pressure of  $As_2$  which equilibrates with the melt of a given the arsenic concentration. In this study 0.96 atmosphere is taken for the value of  $P_{As_2}$ , which is the equilibrium vapor pressure of arsenic at the melting

temperature (1511 K) of gallium arsenide. Activity coefficients for electron and hole were expressed by Hwang and Brews (180). However, other investigators (181) claimed that their results were seriously in error and badly overestimated the magnitude of  $|\gamma_i - 1|$  in uncompensated materials. It is believed that the effects of the activity coefficient are important only in very closely compensated materials. The quantities of  $\gamma_n$  and  $\gamma_p$  are formally included in this paper but their magnitude is everywhere set equal to unity.  $n(gt)$  is the electron concentration at growth temperature.

Brozel *et al.* (182) determined the concentrations of  $[Si_{Ga}]$  and  $[Si_{As}]$  by the measurement of localized vibrational mode (LVM) intensities in gallium arsenide grown from the melt. The behavior of silicon can be determined directly because each defect species gives rise to infrared absorption lines of characteristic frequencies arising from the LVM of silicon impurity atoms. Their data show  $[Si_{Ga}]$  is much higher than  $[Si_{As}]$  by the factor of 6, implying that most of  $V_{Ga}$  react with silicon in the melt and are consumed to produce  $Si_{Ga}^+$  by equation (4.10). Since Hurle (170) has shown the Frenkel defect on the arsenic sublattice dominated the electron concentration, it is assumed that  $[V_{Ga}^-]$  is small enough to be neglected in the electroneutrality condition, equation (4.19). With  $[V_{Ga}^-]$  neglected, equation (4.19) can be solved for the electron concentration at growth temperature,  $n(gt)$ , with respect to  $[Si_i]$ . (See Appendix 2 for detail.)

$$n^2(gt) = \frac{K_8 + \underline{K}_{13} P_{As_2}^{\frac{1}{2}} \gamma_{Si} [Si_i] + \frac{K_2 K_6}{K_1 P_{As_2}^{\frac{1}{2}}}}{1 + \frac{\underline{K}_{14} \gamma_{Si} [Si_i]}{P_{As_2}^{\frac{1}{2}}} + \underline{K}_{15} \gamma_{Si} [Si_i]} \quad (4.44)$$

To apply this chemical equilibrium model to melt grown gallium arsenide, one needs to estimate the lumped equilibrium constants, *i.e.*,  $\underline{K}_{13}$ ,  $\underline{K}_{14}$ , and  $\underline{K}_{15}$ , and  $\gamma_{Si}$ . The activity coefficient of silicon,  $\gamma_{Si}$ , for melt growth is estimated using equation (4.34) with the interaction parameters, equations (4.35), (4.36), (4.37). At growth temperature (1511 K),  $\gamma_{Si}=2.4$  assuming the melt is stoichiometric (*i.e.*,  $[Ga]/[As] = 1$ ). Brozel *et al.*'s LVM data (182) was applied to this model to estimate the lumped equilibrium constants,  $\underline{K}_{13}$ ,  $\underline{K}_{14}$ , and  $\underline{K}_{15}$ , with the assumptions that (a) all of  $Si_{Ga}$  and  $Si_{As}$  are ionized to  $Si_{Ga}^+$  and  $Si_{As}^-$ , (b) the net electron concentration is  $[Si_{Ga}^+] - [Si_{As}^-] - [Si_{Ga}V_{Ga}^-]$ , and (c) only the value obtained from the front end of crystal is applicable because the silicon concentration in the melt is changing as growth proceeds due to segregation effects. Equations (4.38), (4.39), (4.40) and equation (4.44) were solved simultaneously to give the following values at the melting temperature.

$$\underline{K}_{13}(1511K) = 1.33 \times 10^{-4} \quad (4.45)$$

$$\underline{K}_{14}(1511K) = 5.651 \quad (4.46)$$

$$\underline{K}_{15}(1511K) = 9.013 \quad (4.47)$$



This chemical equilibrium model was applied to data existing in the literature. Green (183) grew silicon doped gallium arsenide by the horizontal gradient freeze technique and measured room temperature values of  $N_D - N_A$  for grown gallium arsenide with respect to the amount of silicon added to the melt.  $[Si_{Ga}^+]$ ,  $[Si_{As}^-]$ , and  $[Si_{Ga}V_{Ga}^-]$  were calculated using his data by equations (4.38), (4.39), (4.40), and (4.44).  $N_A$  was calculated as  $[Si_{As}^-] + [Si_{Ga}V_{Ga}^-]$  and  $N_D$  as  $[Si_{Ga}^+]$  assuming all Si defects were "frozen-in" while the crystal cooled to room temperature. Comparison between his  $N_D - N_A$  data and calculated  $N_D - N_A$  by this model shows good prediction of the carrier density by this model. Figure 4-4 shows the comparison between the model and the existing data which are from the experiments of Green (183) as well as from Mo *et al.* (173) who measured  $N_D$  and  $N_A$  of Si-doped gallium arsenide grown by gradient freeze technique.

The total silicon concentration in crystal can be predicted from this model as follows:

$$\begin{aligned} \Sigma Si &= [Si_{Ga}^+] + [Si_{As}^-] + [Si_{Ga}V_{Ga}^-] + 2[Si_{Ga}Si_{As}] \\ &= K_{13} \frac{P_{As_2}^{\frac{1}{2}}}{n(gt)} \gamma_{Si}[Si_i] + K_{14} \frac{n(gt)}{P_{As_2}^{\frac{1}{2}}} \gamma_{Si}[Si_i] + K_{15} P_{As_2} n(gt) \gamma_{Si}[Si_i] \\ &\quad + 2K_{12} K_{13} K_{14} \gamma_{Si}^2 [Si_i]^2 \end{aligned}$$

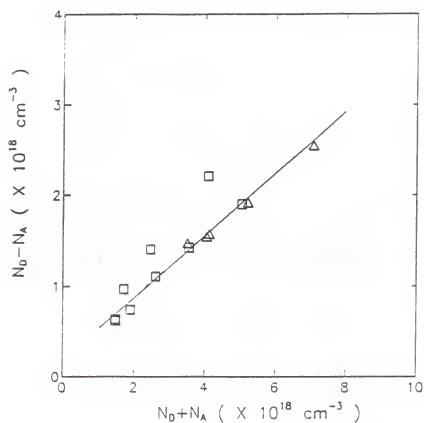


Figure 4-4. Comparison of  $N_D - N_A$  vs.  $N_D + N_A$  between the model prediction and the experimental values.  $\square$ : Mo *et al.* (1973),  $\triangle$ : Green (1983), and - : model's prediction.

$$\begin{aligned}
&= \left( K_{13} \frac{P_{As_2}^{\frac{1}{2}}}{n(gt)} + K_{14} \frac{n(gt)}{P_{As_2}^{\frac{1}{2}}} + K_{15} P_{As_2} n(gt) \right) \\
&\quad + 2K_{12} K_{13} K_{14} \gamma_{Si}[Si_i] \times \gamma_{Si}[Si_i] \quad (4.48)
\end{aligned}$$

where  $n(gt)$  is given by equation (4.44). Figure 4-5 shows the total silicon concentration in gallium arsenide as a function of the amount of silicon added in the melt. It shows a linear dependence of total silicon concentration on the silicon concentration in the melt,  $[Si_i]$ . In *Ge*-doped *GaAs*, it was shown that *Ge* concentration increased parabolically at high *Ge* concentration in the melt due to the excess *Ge* in the form of neutral  $Ge_{Ga}Ge_{As}$  nearest neighbor pairs. In the case of *Si*-doped *GaAs*, however, concentrations of each defect species calculated using this model showed that the last term in equation (4.48), representing  $[Si_{Ga}Si_{As}]$  complex, is a minor defect in gallium arsenide even at high concentration of *Si*. Using equations (4.38), (4.39), (4.40), and (4.44), the concentration of each defect,  $[Si_{Ga}^+]$ ,  $[Si_{As}^-]$ , and  $[Si_{Ga}V_{Ga}^-]$ , has been calculated and is also plotted in figure 4-6. The model predicts that silicon in gallium arsenide predominantly occupies the gallium sublattice, and that the concentration of  $Si_{Ga}V_{Ga}^-$  is higher than that of  $Si_{As}^-$ . This agrees with Mo *et al.* (173) who proposed that  $Si_{Ga}V_{Ga}^-$  was the predominant compensating acceptor in silicon doped gallium arsenide crystal.

Silicon doping of the melt grown crystals produces n-type conductivity and the electron concentration in the crystal can be written as:

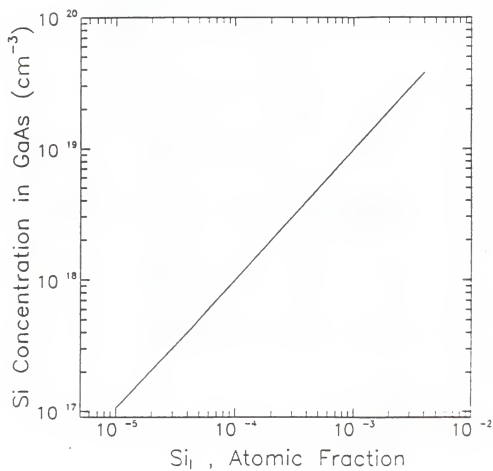


Figure 4-5. Total silicon concentration predicted by the model as a function of silicon concentration in the melt.

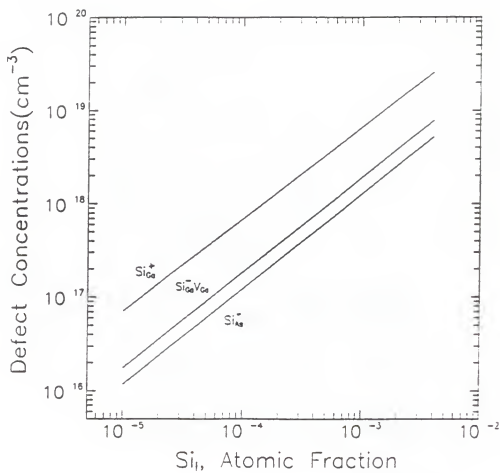


Figure 4-6. The concentrations of each silicon defect in *GaAs* as a function of silicon concentration in the melt.

$$\begin{aligned}
 n_{rt} &= [Si_{Ga}^+] - [Si_{As}^-] - [Si_{Ga}V_{Ga}^-] \\
 &= [K_{13} \frac{P_{As_2}^{\frac{1}{2}}}{n(gt)} - K_{14} \frac{n(gt)}{P_{As_2}^{\frac{1}{2}}} - K_{15} P_{As_2} n(gt)] Y_{Si} [Si_i] \quad (4.49)
 \end{aligned}$$

This expression is plotted in figure 4-7. Several researchers have studied the compensation ratio. Using the table given by Walukiewicz *et al.* (who defined the compensation ratio as  $N_A^-/N_D^+$ ) (184), Green found a compensation ratio of 0.4 for his samples, and this value is much higher than the value of about 0.2 for the  $[Si_{As}^-]/[Si_{Ga}^+]$  ratio deduced from the LVM measurements (183). On the other hand, Brozel *et al.* (185) studied silicon doping gallium arsenide and measured  $[Si_{Ga}^+]$  and  $[Si_{As}^-]$ . The value of compensation ratio,  $\theta = [Si_{As}^-]/[Si_{Ga}^+]$ , was found to be 0.14. However, the compensation ratio of Brozel *et al.*'s and Green's did not include  $Si_{Ga}V_{Ga}^-$  complex which acts as the dominant acceptor, leading to serious error. The model proposed here gives a compensation ratio of about 0.43 up to the concentration of  $5 \times 10^{-4}$  atomic fraction of Si in the melt, which produces about  $2-3 \times 10^{18}/cm^3$  of silicon in gallium arsenide. In this paper, compensation ratio is calculated as the ratio between acceptor and donor (*i.e.*,  $([Si_{As}^-] + [Si_{Ga}V_{Ga}^-])/[Si_{Ga}^+]$ ), and is plotted in figure 4-8. Mullin *et al.* (174) expected a compensation ratio of  $\sim 0.4$  if an unknown acceptor (*i.e.*,  $Si_{Ga}V_{Ga}^-$ ) was included in the calculation; a value close to this prediction. The compensation ratio increases rapidly above  $5 \times 10^{-3}$  atomic fraction of Si in the melt, meaning silicon produces more  $Si_{As}^-$  and  $Si_{Ga}V_{Ga}^-$  than  $Si_{Ga}^+$ . The segregation coefficient for silicon,  $\kappa = \Sigma[Si]/[Si_i]$ , is shown in figure 4-9.

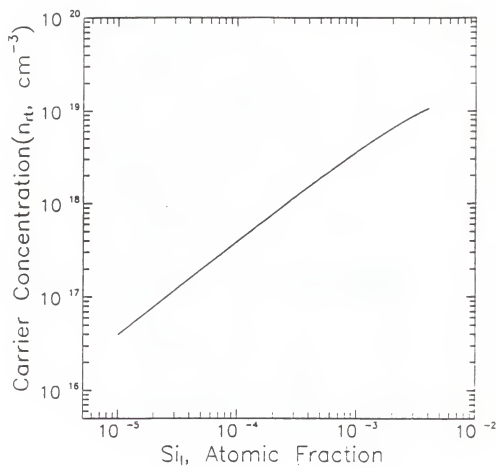


Figure 4-7. Carrier concentration predicted by the model as a function of silicon concentration in the melt.

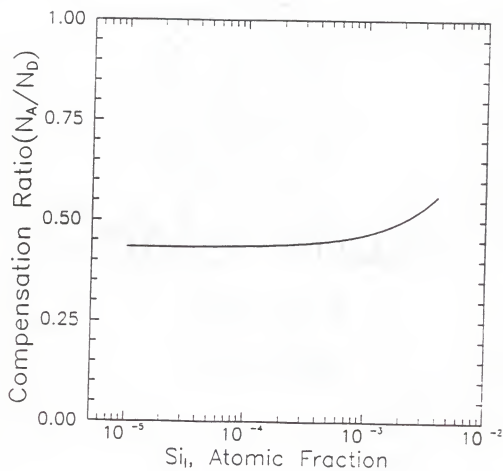


Figure 4-8. Predicted compensation ratio by the model.



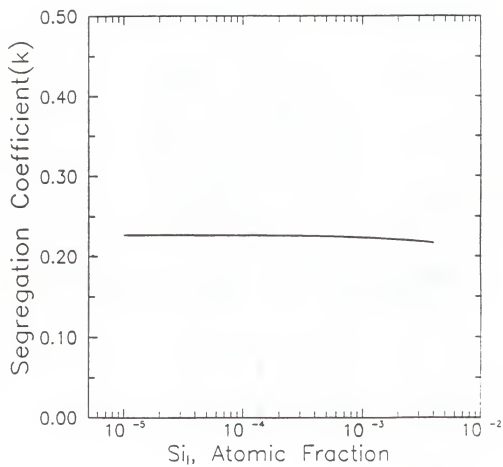


Figure 4-9. Predicted segregation coefficient by the model.

Pelevin *et al.* (186) measured the total silicon concentration in Si-doped GaAs and deduced 0.136 as a segregation coefficient. Green (183) calculated a value of 0.1236 using his experimental data. But his value was calculated based on the assumption that the compensation ratio was 0.3. This is the average of 0.4 and 0.2 from the literature. If 0.4 is used instead of 0.3 as the compensation ratio, the  $\kappa$  value must be about 0.21 which is very close to the value 0.226 predicted by our model. Also the  $\kappa$  value of 0.22 was calculated using the data of Mo *et al.* for silicon-doped gallium arsenide grown by the gradient freeze and Bridgman techniques.

#### 4.4.3. Conclusions

A thermochemical model for the point defect chemistry of silicon-doped gallium arsenide has been developed and applied to melt grown gallium arsenide. The model includes Frenkel disorder on the arsenic sublattice as the dominant disorder, Schottky disorder, electron and hole generation and recombination, and the incorporation of silicon. Several unknown equilibrium constants were lumped together and these lumped equilibrium constants at the growth temperature were estimated using data from the literature. The model developed in this study fits very well with data in the literature showing  $N_D - N_A$  vs.  $N_D + N_A$ . This model was used to predict the total silicon concentration in gallium arsenide, the concentration of each defect, and the free carrier concentration as a function of silicon atomic fraction in the melt. The model also predicts a compensation ratio ( $N_A/N_D$ ) of 0.43 and a segregation coefficient of silicon of 0.226. To develop a model capable of predicting

silicon behavior in LPE and VPE growth in addition to that in melt growth, more extensive studies on silicon doping of gallium arsenide need to be performed.

## CHAPTER 5

### SUMMARY AND RECOMMENDATIONS

#### 5.1 Chemistry of Interaction Between GaAs, Encapsulant, and the Quartz Crucible

The study of the chemistry of interaction between the conventional encapsulant ( $B_2O_3$ ), the conventional growth container (quartz) and molten *GaAs* was presented in chapter 2. The objectives of this study were to provide a better understanding of the melt-encapsulant-container chemistry and verification of three suitable mixed oxide system that can be used to improve encapsulated growth of *GaAs*. Based on several criteria, a long list of alternative encapsulants was narrowed to the addition of an isoelectronic analog oxide to  $B_2O_3$ . The list of mixed oxides and compositions studied is given in table 2-5.

The dissolution of *Ga*, *As* and *Si* by encapsulant and of *Si* and oxide metal (*B*, *La*, *Nb*, *Al*) in gallium arsenide during growth was studied as a function of the  $B_2O_3$  water content and contact time. The amount of *Ga* dissolved in  $B_2O_3$  after contact for an hour at 1250 °C was significant and found to depend on the initial water content in the  $B_2O_3$ . The *Ga* uptake was seen to be significant (about 0.4 wt. %) and not strongly dependent on the choice of encapsulant. To understand the reaction and dependence of *Ga* uptake on the encapsulant water content, two possible *Ga* oxidation reactions with water in encapsulant were considered. The reaction which

represents the formation of  $Ga_2O$  by reaction of  $Ga$  with  $H_2O$  was seen to be stoichiometrically consistent with the experimental results. The  $Ga$  uptake was found not to depend on contact time, indicating true equilibrium was reached. Similar studies were performed on the  $As$  uptake, though the uptake level was considerably lower (near the detection limit of ICP).

The behavior of  $Si$  dissolution in the encapsulant was the opposite to that found with  $Ga$ . The uptake was time dependent and did not depend on the  $H_2O$  content. Apparently the dissolution of  $SiO_2$  by the encapsulant is kinetically controlled; the rate slightly different with each different additives. The incorporation of various elements in the grown gallium arsenide was analyzed by SIMS. The main impurities in gallium arsenide were  $Si$  and the metal atoms used in the oxide encapsulant. The concentrations of  $Si$  and  $B$  in gallium arsenide were found to be a function of the  $H_2O$  content in the starting  $B_2O_3$ . A higher water content in the encapsulant suppressed the incorporation of  $Si$  and  $B$  in gallium arsenide. The concentrations of these two elements in gallium arsenide were reduced by adding  $Ga_2O_3$  to the encapsulant.

Measurement of the surface tension between molten gallium arsenide and the liquid encapsulant was attempted by the Wilhelmy plate method. The measurements were not successful due to the difficulties in working at an extremely high temperature. Preliminary experiments at room temperature with organic systems, however, indicated that Wilhelmy plate method was a suitable method to measure surface tension of liquid-liquid systems. Though some progress was made (e.g.,

improved crucible design which utilized a graphite guide for better alignment), there are still problems to be solved such as balance wire reaction and plate wetting.

### 5.2 Measurement of the Ga Activity Along the Ga-Rich Liquidus and Critical Assessment of the Phase Diagram and Thermochemistry of the Ga-As System

A thermodynamic study of the *Ga-As* system was carried out in a solid electrolyte galvanic cell. This galvanic cell used yttria stabilized zirconia as a solid electrolyte to measure the activity of gallium in *Ga-As(l)* along the *Ga*-rich liquidus line. A improved cell design was used to prevent the loss of arsenic by vaporization during the experiment. The activity of gallium was obtained from the open-circuit emf of this galvanic cell in the temperature range 923 to 1373 K. The activity of gallium showed negative deviation from ideal solution behavior. There have been two previous reports in the literature of activity of gallium measurement using solid electrolyte cells. There are, however, major discrepancies between these results. The activity data obtained in this study were found to be consistent with other thermodynamic and phase diagram data.

The assessment and optimization of thermodynamic properties and phase diagram of *Ga-As* system was conducted using the Redlich-Kister expression for the excess Gibbs energy of the liquid phase. The calculated melting temperature with optimized coefficients was 1237.75 °C, which agrees very well with experimental data. Also the enthalpy of mixing is fully consistent with experimental data at 1300 °C. Activity data obtained experimentally in this study matches well with the optimized model, suggesting the measurements were successful.

### 5.3 The Thermochemical Model of Si Incorporation in GaAs During Crystal Growth

Silicon is commonly used as an intentional n-type dopant in *GaAs* crystal growth. Belonging to the group IV column of the periodic table, silicon can substitute on either a gallium or an arsenic site, resulting in n-type or p-type material, respectively. Under most conditions, *Si* will substitute for *Ga*, rendering *GaAs* n-type. Therefore, in order to produce *GaAs* crystals with the desired electrical properties, one needs to have a means to control the incorporation of silicon. In chapter 4, a thermochemical model was developed to predict the total concentration of *Si* in gallium arsenide, the concentration of each native point defect, and the carrier concentration as a function of silicon atomic fraction in the melt.

The model includes arsenic Frenkel disorder as well as Schottky disorder. The model allows silicon to substitute on either the gallium or the arsenic sublattice. The interstitial site is, however, excluded. Complex defects such as  $Si_{Ga}Si_{As}$  and  $Si_{Ga}V_{Ga}^-$  were also postulated to exist. A set of defect formation reactions as well as the electroneutrality condition were used to represent the equilibrium incorporation of silicon in gallium arsenide. Unknown equilibrium constants, which were required to solve this set of reaction equations, were lumped together and the values were estimated from a fit to existing *Si* incorporation data in the literature.

The growth conditions described in the literature were applied to this model and the results were compared to their experimental results. The free carrier concentration calculated by the model showed very good agreement with

experimental values. The model showed that silicon predominantly occupies gallium substitutional sites and the  $Si_{Ga}V_{Ga}^-$  was the predominant compensating acceptor in melt grown gallium arsenide. The model gave a compensation ratio of 0.43 and a segregation coefficient for Si of 0.21.

#### 5.4 Recommendations

Alternative Encapsulant. The proposed mixed oxide as encapsulants should be the subject of thermophysical property measurements (e.g., dynamic viscosity, surface tension and thermal conductivity). The surface tension measurement was attempted by this author, but was not successful. There are two major problems to be solved in the measurement by the Wilhelmy plate method. First, a balance wire material needs to be found which can endure the high temperature and reactive melts. Second, a plate material which is chemically compatible with the gallium arsenide melt and completely wets the liquid encapsulant and gallium arsenide melt must be found to achieve accurate measurement. It is suggested that an extensive material test be preceded before the measurement.

The magnitude of the improvement possible by use of these alternative encapsulants can only be ascertained after the thermophysical properties have been determined. The initial results, however, suggest further study is warranted.

Electrochemical Study. Extension of the experimentally accessible temperature range to temperatures greater than the melting temperature of gallium arsenide would be important as this range lies outside that accessible by most techniques (e.g., Knudsen cell mass spectrometry). To achieve this, a more reliable



cell design needs to be developed to prevent arsenic loss due to its high vapor pressure at the higher temperatures (approximately 1 atm at 1238 °C). Coulometric titration could be used to measure the extent of solid solution in gallium arsenide.

A few experimental data for the Gibbs energy of formation of  $GaAs$  have been published. Therefore, there is a need to obtain experimental data. A simple galvanic cell using a solid electrolyte can be used to measure the Gibbs energy of formation. The reference electrode consists of  $Ga(l)$  with  $Ga_2O_3$  and the working electrode consists of  $GaAs(s)$  and  $As(s)$  with  $Ga_2O_3$ . The emf of this cell can be used to obtain the Gibbs energy of formation for  $GaAs$  as a function of temperature.

It is also suggested to apply solid electrolytes to visualize the extent of convective flow in the melt. With the use of a solid oxygen ion conducting electrolyte, trace quantities (*ppm*) of oxygen can be electrochemically introduced into the melt at a point or surface in a very accurate manner (*e.g.*, a constant flux or concentration boundary condition can be applied). The concentration of oxygen can then be measured electrochemically as a function of time at other locations in the melt. This permits flow patterns to be "visualized" in a non-disruptive fashion.

Defect Model. The thermochemical model developed in chapter 4 for the incorporation of  $Si$  in melt grown gallium arsenide needs to be expanded to include liquid phase epitaxy (LPE) as well as vapor phase epitaxy (VPE) data. Silicon shows a very complicated behavior which depends on the technique and conditions of growth. For example, in LPE there is a critical temperature (850 °C), below which silicon doping generates p-type material, while above this temperature n-type gallium

arsenide is produced. For gallium arsenide bulk material grown with an encapsulant, the effects of the encapsulant on the incorporation of silicon into crystal should be taken into consideration.

In order to develop a complete thermochemical model, more studies on the thermodynamics of defect formation and a experimental technique for the identification of defect species should be preceded. It is also expected that the semi-insulating behavior of undoped gallium arsenide crystals may be understood through the native defect study of gallium arsenide crystals.

## APPENDIX 1

### MEASUREMENT OF THE SURFACE TENSION BETWEEN A LIQUID ENCAPSULANT AND THE GaAs MELT BY THE WILHELMY PLATE METHOD

#### 1.1 Theory

The Wilhelmy plate method (187) utilizes the weight change occurring when a thin plate is just detached (receding) from or contacted (advancing) to the liquid surface of interest. The general equation governing this process is:

$$\gamma \cos \theta = \frac{\Delta W}{p} \quad (A1.1)$$

where  $\Delta W$  is the change in weight (*i.e.*, force exerted by) of the plate when it is detached from or contacted to the liquid surface, and  $\gamma$  the surface tension, and  $p$  the perimeter of the plate.  $\theta$  is the contact angle and, if finite, may be measured in the same experiment (188). A zero contact angle, however, is preferred because measuring the height of top of the meniscus above the level liquid surface is extremely difficult especially in a high temperature experiment. The Wilhelmy plate method holds to within 0.1% error and no corrections are needed (189-191).

#### 1.2 Experimental

The experimental apparatus are depicted schematically in figure A1-1. The system had four main parts:

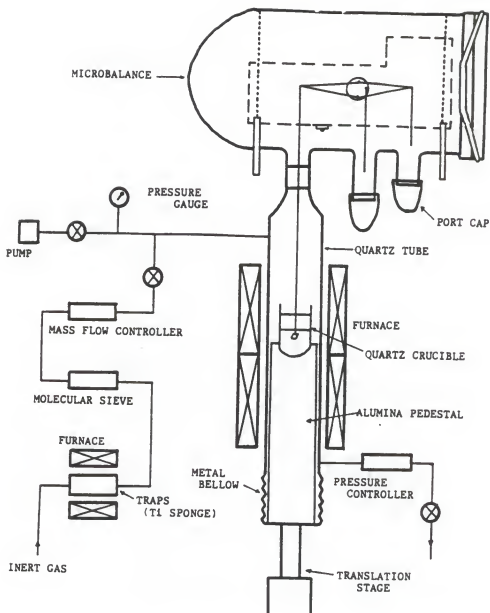


Figure A1-1. Schematic of the apparatus used for surface tension measurement.

- (a) Gas manifold: High purity argon gas was used as an inert gas and was purified further in two steps. Oxygen, nitrogen, carbon monoxide, and carbon dioxide were removed from the gas by passing through titanium sponge at 850 °C and water vapor was removed by a molecular sieve (type 13X). The pressure inside the quartz tube was controlled by a pressure controller (MKS type 250B pressure/flow controller). The tubing is 1/4 inch stainless steel and Swagelok fittings were used.
- (2) Microbalance: A recording microbalance was used with sensitivity of 0.1 microgram, capacity up to 3.5 grams, and repeatability of 0.001-0.005% (as a percent of total sample load).
- (3) The furnace (Model 1249 tubular tapped furnace from Marshall Furnace company) was designed specifically for the surface tension measurement. The specifications of the furnace were (a) 1300 °C operation, (b) multitaps for temperature profile adjustment, (c) 5 inch ID, 36 inch length, (d) two viewing ports, 180° apart, and (e) air operation.
- (4) Translation stage: This (Model # 440 -OMA with motorized drive model # 860-4 from Newport Corporation) is used to achieve vertical motion of crucible at the speed of 1-5 cm/hr.

The experimental procedure is outlined below.

Encapsulant and gallium arsenide were loaded in the crucible and the quartz tube was evacuated. Then the furnace was held at temperature of 1000-1100 °C for an hour to dry water absorbed on the surface of encapsulant. Vacuum was reapplied

and the temperature was raised above the melting temperature of gallium arsenide. Then, argon gas at the rate of 10-50 *sccm* flowed through the apparatus at the controlled pressure of 1-2 atm. After the temperature and flow of the gas were stabilized, the advancing and receding weight changes as the plate crossed the interface with the aid of the vertical motion of translation stage between molten gallium arsenide and encapsulant are measured by the microbalance.

### 1.3 Results and Discussion

Quartz might seem as the logical choice of the crucible material, but the chemical compatibility test showed that encapsulant dissolved the quartz. The crucible was, therefore, made of graphite which is inert to the encapsulant and *GaAs* melt. In addition graphite is easier to machine and less expensive than quartz (the crucible is not reusable). In the first experiments problems with aligning the plate in the center of the crucible were experienced. The plate would drift to the crucible wall and stick to it. To solve this problem, a graphite guide was designed as shown in figure A1-2. This graphite guide prevented the balance wire from moving to the side wall. Using the graphite crucible with the guide, the surface tension of several systems were measured at room temperature (i.e., water-air, benzene-air, water-n-hexane, and water-n-octanol). The results of these experiments are listed in table A1-1. A platinum plate was used in these room temperature experiments and our experimental values are very close to the published values, verifying the Wilhelmy plate method is suitable for measuring surface tension in liquid-liquid systems.

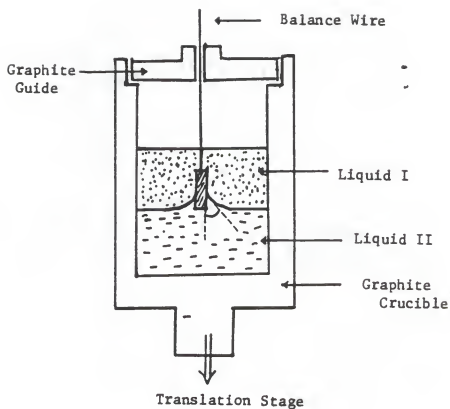


Figure A1-2. The graphite crucible with a graphite guide to align the balance wire.

Table A1-1. The results of preliminary surface tension measurements at room temperature using a platinum plate.

System	Plate <sup>(a)</sup>	Surface Tension at 23 °C (dyne/cm)	Published value <sup>(b)</sup> at 20 °C (dyne/cm)
Water-Air	1	72.25	71.97
	2	72.35	
Benzene-Air	1	28.75	28.85
	2	28.72	
Water-n-Hexane	1	45.62	50.8
	2	45.62	
Water-n-Octanol	1	7.01	8.5
	2	7.01	

- (a) Plate 1: Platinum, P = 5.2 cm  
 Plate 2: Platinum, P = 5.8 cm

- (b) Data from CRC handbook of Chemistry and Physics, 63rd Ed.



In order to measure the surface tension by Wilhelmy plate method, the contact angle,  $\theta$ , must be known. A zero contact angle is desirable in this method so that the cosine term in the equation (A1.1) becomes unity. Measurement of the contact angle is difficult, especially at temperatures in excess of 1000 °C (the temperature of interest in this study). Therefore, different plate materials were studied to achieve a contact angle of zero. If the contact angle is not zero, the measured weight changes are different when the plate is advancing toward the interface compared to that when the plate is receding from the interface. On the other hand, these values are the same when the contact angle is zero. The former case is illustrated in figure A1-3. The surface tension for the water-hexane system was measured with a PBN plate at room temperature. As shown in figure A1-3, the measured weight change when the plate was advancing is different from that when the plate was receding, which means that the contact angle was not zero. This PBN plate was designed for the measurement of molten gallium arsenide-encapsulant system.

Because gallium and arsenic react with most materials, there was little choice but using PBN. In order for the plate to be immersed in the gallium arsenide melt, the density of PBN should be greater than that of the gallium arsenide melt. Since this is not the case for PBN, the plate was made of tungsten covered with a PBN sheath so that the total density of plate was greater than that of the gallium arsenide melt. In addition, the size of the plate should be less than one third of the crucible

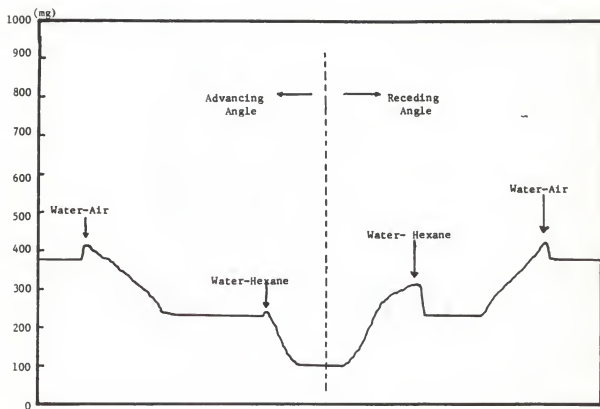


Figure A1-3. Measurement of surface tension of water-hexane system with a PBN plate. A non-zero contact angle causes a difference between advancing and receding values.

diameter to avoid wall effects. The thickness of plate should also be minimized as much as possible to eliminate the erroneous result due to buoyancy effects.

Several experiments at room temperature were performed to measure the surface tension of  $B_2O_3$ -inert gas ( $Ar$ ) with a PBN plate at 700 °C. The result is shown in figure A1-4. Advancing and receding values were different from each other and not close to the published values. This is because the PBN is not completely wetted by the  $B_2O_3$  (i.e., non-zero contact angle).

Measurement of surface tension of the gallium arsenide melt-encapsulant system was attempted with a 0.1 mm diameter tungsten wire as the balance wire. Above 700 °C, this wire broke in every experiment. Nicrome and platinum wires were also tried, but these experiments were not successful either. Using a thicker balance wire to prevent this breakage is not acceptable because the total weight (wire+plate+force by surface tension) would exceed the maximum capacity of microbalance.

While the Wilhelmy plate method was hindered by a balance wire problem, a different approach was attempted to measure the surface tension: the drop weight method. This method has been used in the past to measure the surface tension of liquid-air and liquid-liquid interfaces. The procedure is to form drops of the liquid at the end of a capillary tube allowing them to fall into the container containing the second liquid phase. After collecting a sufficient number of drops, the weight per drop is determined accurately. A simple expression for the weight of a drop,  $W$ , is given by Tate' law (192):

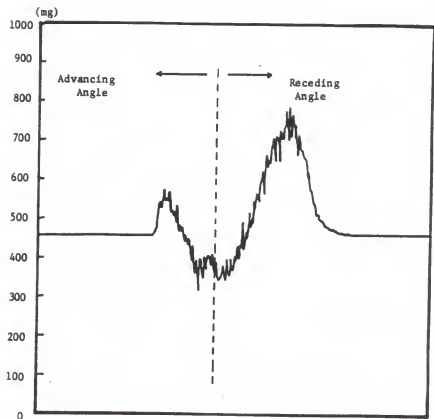


Figure A1-4. Measurement of the surface tension of  $B_2O_3$ -Inert gas (Ar) system with a PBN plate. A non-zero contact angle causes a difference between the advancing and receding values.

$$W = 2\pi r\gamma f \quad (\text{A1.2})$$

where  $W$ : the weight of a drop  
 $r$ : The radius of the tip of capillary  
 $\gamma$ : surface tension  
 $f$ : correction factor.

Several experiments were attempted using this method. It was required to optimize the diameter of capillary tube and develop a technique to generate drops continuously with the same volume (or weight). Another potential problem was that the capillary was made of quartz and the measurement might be affected by the dissolution of quartz into encapsulant, changing the value of the surface tension.

In conclusion, the Wilhelmy plate method appears to be a better technique to measure the surface tension of the gallium arsenide melt-encapsulant system. However, in order to be successful, a wire which can endure high temperature must be tested. Also efforts should be directed at finding a plate material which has a zero or small contact angle in the gallium arsenide melt-encapsulant system.

## APPENDIX 2

### PROCEDURE FOR CALCULATING THE CONCENTRATION OF EACH DEFECT SPECIES

#### 2.1 Calculation of $[Si_{Ga}^+]$

From equation (4.26)

$$[Si_{Ga}^+] = \frac{K_9[V_{Ga}]\gamma_{Si}[Si_i]}{\gamma_n n(gt)} \quad (A2.1)$$

We need to express  $[V_{Ga}]$  in terms of known variables. Therefore, from equations (4.22), (4.21), and (4.20)

$$[V_{Ga}] = \frac{K_3}{[V_{As}]} \quad (A2.2)$$

$$[V_{As}] = \frac{K_2}{[As_i]} \quad (A2.3)$$

$$[As_i] = \frac{K_1}{P_{As_2}^{-\frac{1}{2}}} \quad (A2.4)$$

Combining these equations gives

$$[V_{Ga}] = \frac{K_3}{K_2} [As_i] = \frac{K_1 K_3}{K_2 P_{As_2}^{-\frac{1}{2}}} \quad (A2.5)$$

and substituting equation (A2.5) into (A2.1), then

$$\begin{aligned}
 [Si_{Ga}^+] &= \frac{K_1 K_3 K_9}{K_2} \frac{P_{As_2}^{\frac{1}{2}}}{\gamma_n n(gt)} \gamma_{Si} [Si_i] \\
 &= K_{13} \frac{P_{As_2}^{\frac{1}{2}}}{\gamma_n n(gt)} \gamma_{Si} [Si_i]
 \end{aligned} \tag{A2.6}$$

where

$$K_{13} = \frac{K_1 K_3 K_9}{K_2}$$

## 2.2 Calculation of $[Si_{As}^-]$

From equation (4.27)

$$[Si_{As}^-] = \frac{K_{10} [V_{As}] \gamma_{Si} [Si_i]}{\gamma_p p(gt)} \tag{A2.7}$$

We need to express  $[V_{As}]$  and  $p(gt)$  in terms of known variables. From equations (A2.3) and (A2.4)

$$[V_{As}] = \frac{K_2}{[As_i]} = \frac{K_2}{K_1} P_{As_2}^{-\frac{1}{2}} \tag{A2.8}$$

and from equation (4.25)

$$p(gt) = \frac{K_8}{\gamma_n \gamma_p n(gt)} \tag{A2.9}$$

Substituting equations (A2.8) and (A2.9) into equation (A2.7) gives

$$\begin{aligned}
 [Si_{\Lambda s}^-] &= \frac{K_2 K_{10}}{K_1 K_8} \frac{\gamma_n n(gt)}{P_{\Lambda s_2}^{\frac{1}{2}}} \gamma_{Si} [Si_i] \\
 &= K_{14} \frac{\gamma_n n(gt)}{P_{\Lambda s_2}^{\frac{1}{2}}} \gamma_{Si} [Si_i]
 \end{aligned} \tag{A2.10}$$

where

$$K_{14} = \frac{K_2 K_{10}}{K_1 K_8}$$

### 2.3 Calculation of $[Si_{Ga} V_{Ga}^-]$

From equation (4.28)

$$[Si_{Ga} V_{Ga}^-] = \frac{K_{11} [Si_{Ga}^*] [V_{Ga}^-]}{\gamma_p p(gt)} \tag{A2.11}$$

and from equations (4.24) and (A2.5),

$$[V_{Ga}^-] = \frac{K_7 [V_{Ga}]}{\gamma_p p(gt)} = \frac{K_1 K_3 K_7}{K_2} \frac{P_{\Lambda s_2}^{\frac{1}{2}}}{\gamma_p p(gt)} \tag{A2.12}$$

Substitute equation (A2.9) into equation (A2.12) for  $p(gt)$ , then

$$[V_{Ga}^-] = \frac{K_1 K_3 K_7}{K_2} \frac{P_{\Lambda s_2}^{\frac{1}{2}}}{\gamma_p} \frac{\gamma_n \gamma_p n(gt)}{K_8} = \frac{K_1 K_3 K_7}{K_2 K_8} \gamma_n n(gt) P_{\Lambda s_2}^{\frac{1}{2}} \tag{A2.13}$$

Using equations (A2.6), (A2.9), and (A2.13),



$$\begin{aligned}
[Si_{Ga}V_{Ga}]^- &= \frac{K_{11}}{\gamma_p} \frac{\gamma_n \gamma_p n(gt)}{K_8} \frac{K_{13}^P A_{s2}^{\frac{1}{2}} \gamma_{Si}[Si_i]}{\gamma_n n(gt)} \\
&\times \frac{K_1 K_3 K_7 \gamma_n n(gt)^P A_{s2}^{\frac{1}{2}}}{K_2 K_8} \\
&= \frac{K_7 K_9 K_{11} K_1^2 K_3^2}{K_2^2 K_8^2} \gamma_n n(gt)^P A_{s2} \gamma_{Si}[Si_i] \\
&= K_{16}^P A_{s2} \gamma_n n(gt) \gamma_{Si}[Si_i] \quad (A2.14)
\end{aligned}$$

where

$$K_{16} = \frac{K_7 K_9 K_{11} K_1^2 K_3^2}{K_2^2 K_8^2}$$

#### 2.4 Calculation of $n(gt)$ from Electroneutrality Condition

Neglecting  $[V_{Ga}]^-$  from equation (4.19) (see section 4.4.2 for reason)

$$n + [Si_{As}]^- + [Si_{Ga}V_{Ga}]^- = p + [Si_{Ga}]^+ + [V_{As}]^+ \quad (A2.15)$$

Since expressions for  $[Si_{As}]^-$ ,  $[Si_{Ga}V_{Ga}]^-$ ,  $p$ , and  $[Si_{Ga}]^+$  have been derived above, only an expression for  $[V_{As}]^+$  need be found. From equation (4.23),

$$[V_{As}]^+ = \frac{K_6 [V_{As}]}{\gamma_n n(gt)} \quad (A2.16)$$

Substitute equation (A2.8) into above equation, then

$$[V_{As}]^* = \frac{K_6 K_2}{K_1} \frac{1}{\gamma_n n(gt) P_{As_2}^{\frac{1}{2}}} \quad (A2.17)$$

Inserting equations (A2.7), (A2.14), (A2.9), (A2.6), and (A2.17) into equation (A2.15) and solving for  $n(gt)$  gives

$$\begin{aligned} n(gt) + \frac{K_{14}}{P_{As_2}^{\frac{1}{2}}} \gamma_{Si}[Si_i] + \frac{K_{15}}{P_{As_2}^{\frac{1}{2}}} n(gt) \gamma_{Si}[Si_i] \\ = \frac{K_8}{n(gt)} + \frac{K_{13}}{n(gt)} \frac{P_{As_2}^{\frac{1}{2}}}{\gamma_{Si}[Si_i]} + \frac{K_2 K_6}{K_1} \frac{1}{n(gt) P_{As_2}^{\frac{1}{2}}} \end{aligned} \quad (A2.18)$$

Multiplying each side of equation (A2.18) with  $n(gt)$  and solving for  $n^2(gt)$  gives

$$\begin{aligned} n^2(gt) = \frac{K_8 + \frac{K_{13}}{P_{As_2}^{\frac{1}{2}}} \gamma_{Si}[Si_i] + \frac{K_2 K_6}{K_1} \frac{1}{P_{As_2}^{\frac{1}{2}}}}{1 + \frac{K_{14} \gamma_{Si}[Si_i]}{P_{As_2}^{\frac{1}{2}}} + \frac{K_{15}}{P_{As_2}^{\frac{1}{2}}} \gamma_{Si}[Si_i]} \end{aligned} \quad (A2.19)$$

## REFERENCE

1. Goldsmith, V. M., Trans. Faraday Soc., 25, 235 (1929).
2. Driscoll, C. M. H., Willoughby, A. F. W., Mullin, J. B., and Straughan, B. W., Gallium Arsenide and Related Compounds (Institute of Physic, London), 24, 275 (1975).
3. Straumanis, M. E., and Kim, C. D., Acta Crystallogr., 19, 256 (1965).
4. Pierron, E. D., Parker, D. L., and McNeely, J. B., Acta Crystallogr., 21, 290 (1966).
5. Blakemore, J. S., J. Appl. Phys., 53, R123 (1982).
6. Iida, S., and Ito, K., J. Electrochem. Soc., 118, 768 (1971).
7. Kern, W., RCA Rev., 39, 278 (1978).
8. Milnes, A. G., Deep Impurities in Semiconductors, John Wiley and Sons, New York, 1973.
9. Welker, H., and Weiss, H., in Solid State Physics. Vol. 1, ed. by Seitz, F., and Turnbull, D., p.1, Academic Press, New York, 1956.
10. Novikova, S. I., Sov. Phys. Solid State, 3, 129 (1961).
11. Bernstein, L., and Beals, R. J., J. Appl. Phys., 32, 122 (1961).
12. Feder, R., and Light, T., J. Appl. Phys., 39, 4870 (1968).
13. Touloukian, Y. S., and Buyco, E. H., editors, Thermophysical Properties of Matter. Vol. 13 ("Thermal Expansion"), p.747, Plenum Press, New York, 1976.
14. Holland, M. G., Phys. Rev., 134, A471 (1964).
15. Carson, R. O., Slack, G. A., and Silverman, S. J., J. Appl. Phys., 36, 505 (1965).

16. Sturge, M. D., Phys. Rev., 207, 768 (1962).
17. Sell, D. D., Phys. Rev. B., 6, 3750 (1972).
18. Casey, H. C., Sell, D. D., and Wecht, K. W., J. Appl. Phys., 46, 250 (1975).
19. Panish, M. B., and Casey, H. C., J. Appl. Phys., 40, 163 (1969).
20. Sell, D. D., Stokowski, S. E., Dingle, R., and DiLorenzo, J. V., Phys. Rev. B., 7, 4568 (1973).
21. Sell, D. D., Casey, H. C., and Wecht, K. W., J. Appl. Phys., 45, 2650 (1974).
22. Shay, J. L., Phys. Rev. B., 2, 803 (1970).
23. Urbach, F., Phys. Rev., 92, 1324 (1953).
24. Bimberg, D., and Schairer, W., Phys. Rev. Lett., 28, 442 (1972).
25. Thurmond, C. D., J. Electrochem. Soc., 122, 1133 (1975).
26. Shantharama, L. G., Adams, A. R., Ahmad, C. N., and Nicholas, R. J., J. Phys. C., 17, 4429 (1984).
27. Zurawsky, W. P., Littman, J. E., and Drickamer, H. G., J. Appl. Phys., 54, 3216 (1983).
28. Wolford, D. J., and Bradley, J. A., Solid State Commun., 58, 1069 (1985).
29. Welber, B., Cardona, M., Kim, C. K., and Rodriguez, S., Phys. Rev. B., 12, 5729 (1975).
30. Glazov, M. V., Chizhevskaya, S. N., and Glagoleva, N. N., Liquid Semiconductors, p.325, Plenum Press, New York, 1969.
31. Feigelson, R. S., and Route, P. K., Proc. Soc. Photo-Opt. Instrum. Eng., 214, 76 (1979).
32. Brice, J. C., EMIS Data Review, RN=2003, July 1985.
33. Hurle, D. T. J., J. Phys. Chem. Solid, 40, 613 (1979).
34. Bublik, V. T., Karataev, V. V., Kulagin, R. S., Mil'vidskii, M. G., Osvenskii, V. B., Stolyarov, O. G., and Kholoduyi, L. P., Sov. Phys. Cryst., 18, 218 (1973).

35. Brice, J. C., EMIS Data Review, RN=2001, July 1985.
36. Yarmolyu , N. I., Sov. Phys. Semicond., 14, 773 (1980).
37. Brice, J. C., EMIS Data Review, RN = 15257, September 1985.
38. Mullin, J. B., Straugham, B. W., and Briekell, W. S., J. Phys. Chem. Solids, 26, 782 (1965).
39. Metz, E. P. A., Miller, R. C., and Mazelsky, R., J. Appl. Phys., 33, 2016 (1962).
40. Stolte, C.A., Semiconductors and Semimetals, ed. by Willardson, R.K. and Bear, A.C., Vol. 20, p.95, Press Inc., Florida, 1984.
41. Holmes, D. E., Chen, R. T., Elliott, K.R., and Kirkpatrick, C. G., Appl. Phys. Lett., 40, 46 (1982).
42. Pekavek, L., Czech. J. Phys. B., 20, 857 (1970).
43. Puttback, R. C., Elliott, G., and Ford, W., LEC Synthesis and Growth of GaAs at Low Pressure, presented at ACCG-5, Coronado, CA., July 1981.
44. Duncan, W. M., Westphal, G. H., and Sherer, J. B., Elect. Dev. Lett., EDL-4, 199 (1983).
45. Sakurai, K., and Fukuda, T., Japan Semiconductor Technology News, 1, 10 (1982).
46. Ford, W., Galt, J., Barrera, J., and Helgeland, W., LEC Growth and Characterization of Very Large GaAs Crystals, presented at ACCG-6, Atlantic City, NJ., July 1984.
47. Honda, T., Ishii, Y., Miyazawa, S., Yamasakai, H., and Nanishi, Y., Jpn. J. Appl. Phys., 22, L270 (1983).
48. Swiggard, E. M., Digest of Paper: GaAs IC. Symp. Tech. Digest, IEEE., p.26, Piscataway, NJ., 1983.
49. Akai, S., Mass-Producing Technologies for Semi-Insulating GaAs Substrates, presented at The Topical Conference on "Compound Semiconductor Growth, Processing and Device for the 1990's: Japan/U.S. Perspectives", Gainesville, Florida, October 1987.

50. Chang, C. E., and Wilcox, W. R., J. Crystal Growth, 21, 135 (1974).
51. Parsey, T. M., Jr., Nanishi, Y., Lagowski, J., and Gatos, H. C., J. Electrochem. Soc., 129, 388 (1982).
52. Woods, J. F., and Ainslie, N. G., J. Appl. Phys., 34, 1469 (1963).
53. Woodall, J. M., Trans. Metall. Soc., AIME, 239, 378 (1967).
54. Weisberg, L. R., Rosi, F. D., and Herkart, P. G., in Properties of Elemental and Compound Semiconductors, Vol. 5, ed. Gatos, H. C., p.25, Interscience, New York, 1960.
55. Cochran, C. N., and Foster, L. M., J. Electrochem. Soc., 109, 149 (1962).
56. Martin, G. M., Jacob, G., Hallais, J. P., Grainger, F., Roberts, J. A., Clegg, B., Blood, P., and Poiblaud, G., J. Phys. C: Solid State Phys., 15, 1841 (1982).
57. Shikano, K., and Kobayashi, K., Appl. Phys. Lett., 46, 391 (1985).
58. Blum, S. E., and Chicotka, R. J., J. Electrochem. Soc., 120, 588 (1973).
59. Woodbury, H. H., J. Crystal Growth, 35, 49 (1976).
60. Clemans, J. E., Gault, W. A., and Monberg, E. M., AT&T Technical Journal, 65, 86 (1986).
61. Abemathy, C. R., Kinsella, A. P., Jordan, A. S., Caruso, R., Pearton, S. J., Temkin, H., and Wade, H., Technical Memorandum of AT&A Bell Laboratories, File Case 20102-1 38788-1, 1987.
62. Pfann, W. C., Zone Melting, 2nd ed., p.117, Wiley, New York, 1966.
63. Gatos, H.C., "Semiconductor Crystal Growth and Segregation Problems on Earth and in Space", in Materials Processing in the Reduced Gravity Environment of Space, ed. by Rindone, G.E., North-Holland, New York, 1982.
64. Carruthers, J. R., "Material Science in Space", in Material Processing in the Reduced Gravity Environment of Space, ed. by Rindone, G. E., North-Holland, New York, 1982.
65. Napolitano, L. G., Science, 225, 197 (1984).
66. Eyer, A., Leiste, H., and Nitsche, R., J. Crystal Growth, 71, 173 (1983).

67. Johnson, E. S., J. Crystal Growth, 30, 249 (1975).
68. Swiggard, E. M., J. Crystal Growth, 94, 556 (1989).
69. Ford, W. M., AACG West Conf. on Crystal Growth, Fallen Leaf Lake, California, 1979.
70. Emori, H., Kikuta, T., Inada, T., Obokata, T., and Fukuda, T., Jpn. J. Appl. Phys., 24, L291 (1985).
71. Weiner, M. E., Lassota, D. T., and Schwartz, B., J. Electrochem. Soc., 118, 301 (1971).
72. Oliver, J. R., Fairman, R. D., and Chen, R. T., Electron. Lett., 17, 839 (1981).
73. Rumsby, D. H., and Ware, R. M., Paper presented at Int. Symp. Gallium Arsenide and Related Compound, Inst. Phys. Conf. Ser. No.63, Chap. 12, Japan, 1981.
74. Chang, C. E., and Wilcox, W. R., Mat. Res. Bull., 6, 1297 (1971).
75. Mackenzie, J. D., J. Phys. Chem. Ithaca, 63, 1875 (1959).
76. Silver, A. H., J. Chem. Phys., 32, 959 (1960).
77. Adams, R. V., Phys. and Chem. of Glass, 2, 39 (1961).
78. Harrison, A. J., J. Am. Cer. Soc., 30, 326 (1947).
79. Rajan, K. G., Shekar, N. V., Sekar, M., and Selvakuman, D., Bull. Master. Sci., 10, 181 (1988).
80. Woodall, J. M., and Wood, J. F., Solid State Commun., 4, 33 (1966).
81. Derby, J. J., and Brown, R. A., J. Crystal Growth, 74, 605 (1986).
82. Samsomov, G. V., The Oxide Handbook, 2nd ed., IFI/Plenum Data Company, New York, 1982.
83. Pankratz, L. B., Thermodynamic Properties of Elements and Oxides, Bulletin (United States Bureau of Mines): 672, 1982.
84. Levin, E. M., ed., Phase Diagrams for Ceramists, Am. Cer. Soc., 1956.

85. Wypartowicz, J., and Fitzner, K., *J. Less-Comm. Metals*, 138, 289 (1988).
86. Katayama, I., Nakai, T., Inomoto, T., and Kozuka, Z., *Materials Transactions, JIM*, 30, 354 (1989).
87. Tmar, M., Cabriel, A., Chatillon, C., and Ansara, I., *J. Crystal Growth*, 69, 421 (1984).
88. Chatillon, C., Ansara, I., Watson, A., and Argent, B. B., *CALPHAD*, 14, 203 (1990).
89. Lukas, H. L., Henig, E. Th., and Zimmermann, Z., *CALPHAD*, 1, 255 (1977).
90. Kiukkola, K., and Wagner, C., *J. Electrochem. Soc.*, 104, 308 (1957).
91. Kiukkola, K., and Wagner, C., *J. Electrochem. Soc.*, 104, 379 (1957).
92. Schmalzried, H., *Metall. Chem., Proc. Symp.*, HMSO, London, 1971.
93. Komarek, K. L., *Ber. Buns. Phys. Chem.*, 87, 709 (1983).
94. Rapp, R. A., and Shores, D. A., *Tech. Metals Res.*, 4(Pt. 2), 123 (1970).
95. Ramanarayanan, T. A., and Worrell, W. L., *Can. Metall. Q.*, 13, 325 (1974).
96. Wagner, C., *J. Chem. Phys.*, 21, 1819 (1951).
97. Wagner, C., *Progress in Solid State Chemistry*, vol. 6, ed. Reiss, H., and McCaldin, J. O., Pergamon, New York, 1971.
98. Arthur, J. R., *J. Phys. Chem. Solids*, 28, 2257 (1967).
99. Thurmond, C. D., *J. Phys. Solids*, 26, 795 (1965).
100. Hall, R. N., *J. Electrochem. Soc.*, 110, 385 (1955).
101. K $\ddot{o}$ ster, W., and Thoma, B., *Z. Metallk.*, 46, 291 (1955).
102. Sol, N., Clariou, J. P., Lihn, N. T., and Moulin, M., *J. Crystal Growth*, 27, 325 (1974).
103. Hsieh, J. J., unpublished, Lincoln Laboratory Solid State Research Quarterly Report, vol. 3, pp25-28, Lincoln Laboratory, MIT, Lexington, Mass., 1974.



104. Rubenstein, M., J. Electrochem. Soc., 110, 385 (1963).
105. Rakov, V. V., Lainer, B. O., and Mil'vidskii, H. G., Russ. J. Phys. Chem., 44, 922 (1970).
106. Vigdorovich, E. N., Popov, V. V., Artamonov, M. M., and Andreev, V. M., Izv. Akad. Nauk SSSR Neorg. Mater, 2, 771 (1973).
107. Perea, E. H., and Fonstad, C. G., J. Electrochem. Soc., 127, 313 (1980).
108. DeWinter, J. C., and Pollack, M. A., J. Appl. Phys., 58, 2410 (1985).
109. Dutartre, D., Thesis, INSA, Lyon, 1983.
110. Ceolin, R., Bergman, C., Bellissent, R., Menelle, A., Rouland, J. C., and Gaspard, J. P., Solid State Comm., 71, 343 (1989).
111. Lyon, V. J., and Silvestri, V. J., J. Phys. Chem., 65, 1275 (1961).
112. Panish, M. B., J. Crystal Growth, 27, 6 (1974).
113. Richman, D., J. phys. Chem. Solids, 24, 1131 (1963).
114. Folberth, O. G., Z. Naturforsch, 13a, 856 (1958).
115. Pupp, C., Murray, J. J., and Pottie, R. F., J. Chem. Thermodyn. 6, 123 (1974).
116. Foxon, C. T., Joyce, B. A., Farrow, R. F. C., and Griffiths, R. M., J. Phys. D., (Appl. Phys.), 7, 2422 (1974).
117. Khukhryanskii, Y. P., Kondaurov, V. P., Nikolaeva, F. P., Panteleev, V. I., and Shshelev, M. I., Izv. Akad. Nauk SSSR Neorg. Mater, 10, 1877 (1974).
118. Drowart, J. and Goldfinger, P., J. Chim. Physique, 55, 721 (1958).
119. Hirayama, C., Straw, R. D., and Hobgood, H. M., J. Less-Comm. Metals, 109, 331 (1985).
120. van den Boomgaard, J., and Schol, K., Philips Res. Chem., 65, 1275 (1961).
121. Abbasov, A. S., Mamedov, K. N., Nikol'skaya, A. V., Gerasimov, Y. I., and Vasil'ev, V. P., Dokl. Akad. Nauk SSSR 170, 1238 (1966).

122. Krestovnikov, A. N., Ufimtsev, V. B., and Solopai, E. M., *Russ. J. Phys. Chem.*, 45, 1504 (1971).
123. Martosudirjo, S., and Pratt, J. N., *Thermochim. Acta*, 10, 23 (1974).
124. Sirota, N. N., in: Semiconductors and Semimetals, vol. 4, ed. Willardson, R. K., and Beer, A. C., Academic Press, New York, 1968.
125. Lichter, B. D., and Sommelet, P., *Trans. Met. Soc. AIME*, 245, 1021 (1969).
126. Yamaguchi, K., Itagakz, K., and Yazawa, A., *J. Jap. Inst. Metals*, 52, 966 (1988).
127. Dinsdale, A. T., N.P.L. Rep. DMA(A), N.P.L., Teddington, U.K., 1989.
128. Logan, R. M., and Hurle, D. T. J., *Phys. Chem. Solids*, 32, 1739 (1971).
129. Driscoll, C. M. H., and Willoughby, A. F. W., Defects in Semoconductor, p.377, 1972, *Inst. of Phys. Conf. Series*, No 16, 1973.
130. Ikoma, H., and Wang, S. S., *J. Phys. Soc. Japan*, 27, 512 (1969).
131. Iloma, H., *J. Phys. Soc. Japan*, 28, 1474 (1970).
132. Khokhov, V. I., Sidorov, Y. G., and Doveretskii, S. A., *Phys. Status Solidi (a)*, 25, 311 (1974).
133. Inada, T., Otoki, Y., and Kuma, S., *J. Crystal Grpwth*, 102, 915 (1990).
134. Holmes, D. E., Chen, R. T., Elliott, K. R., Kirkpatrick, C. G., and Yu, P. W., *IEEE Trans. on Microwave Theory Tech.*, MIT-10, 949 (1982).
135. Meyer, B. K., Spaeth, J. M., and Scheffler, M., *Phys. Rev. Lett.* 52, 851 (1984).
136. Kaminska, M., Skowronski, M., Lagowski, J., Parsey, J. M., and Gatos, H. C., *Appl. Phys. Lett.*, 43, 302 (1983).
137. Taniguchi, M., and Ikoma, T., *Appl. Phys. Lett.*, 45, 69 (1984).
138. Lagowski, J., Lin, D. G., and Gatos, H. C., *Appl. Phys. Lett.*, 45, 89 (1984).
139. Brozel, M. R., Grant, I., Ware, R. M., Stirland., and Skolnick, M. J., *J. Appl. Phys.*, 56, 1109 (1984).

140. Levinson, M., Phys. Rev., B28, 3660 (1983).
141. Walukiewicz, W., Lagowski, L., and Gatos, H. C., Appl. Phys. Lett., 43, 192 (1983).
142. Huber, A. M., Linh, N. T., Valladon, M., Debrun, J. L., Martin, G. M., Mittonneau, A., and Mircea, A., J. Appl. Phys., 50, 4022 (1979).
143. Lagowski, J., Gatos, H. C., Parsey, J. M., Wada, K., Kaminska, M., and Walukiewicz, W., Appl. Phys. Lett., 40, 342 (1982).
144. Figielski, T., Appl. Phys. A., 35, 255 (1984).
145. Aref'ev, I. S., Bublik, V. T., Morozov, A. N., Karataev, V. V., Koval'chuk, I. A., Mil'vidskii, M. G., and Morozova, O. Y., Sov. Phys. Crystallog., 32, 267 (1987).
146. Hurle, D. T. J., paper presented at 5th Conf. on Semi-insulating III-V Material, Malmö, Sweden, Chapter 1, p.11, 1988.
147. Morrow, R. A., J. Mater. Res., 2, 681 (1987).
148. Lagowski, J., Kaminski, M., Parsey, J. M., Gatos, H. C., and Walukiewicz, W., in GaAs and Related Compound Semiconductors, Inst. Phys. Conf. Ser., 65, 41 (1982).
149. von Bardeleben, H. J., Stievenard, D., Deresmes, D., Huber, A., and Bourgoin, J. C., Phys. Rev. B., 34, 7192 (1986).
150. Bourgoin, J. C., von Bardeleben, H. J., and Stievenard, D. J., Appl. Phys., 64, R65 (1988).
151. Thomas, R. N., Hobgood, H. M., Eldridge, G. W., Barrett, D. L., Braggins, T. T., Ta, L. B., and Wang, S. K., Semiconductor and Semimetals, ed. by Willardson, R. K., and Bear, A. C., Vol 20, p.31, Press Inc., Orlando, 1984.
152. Mircea, A., Mittonneau, A., Hollan, L., and Briere, A., Appl. Phys., 11, 153 (1976).
153. Makram-Ebeid, S., Gantard, D., Devillard, P., and Martin, G. M., Appl. Phys. Lett., 40, 161 (1982).
154. Gledhill, G. A., Newman, R. C., and Woodhead, J., J. Phys. C., 17, L301 (1984).

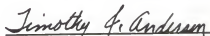
155. Fischer, D. W., and Yu, P. w., J. Appl. Phys., 59, 1952 (1986).
156. Yu, P. W., and Reynolds, D. C., J. Appl. Phys., 53, 1263 (1982).
157. Yu, P. W., Mitchel, W. C., Meir, M. G., Li, S. S., and Wang, W. L., Appl. Phys. Lett., 41, 532 (1982).
158. Bishop, S. G., Shanabrook, B. V., and Moore, W. J., J. Appl. Phys., 56, 1785 (1984).
159. Moore, W. J., and Hawkins, R. L., J. Appl. Phys., 63, 5699 (1988).
160. Frank, W., Gosele, U., Mehrer, H., and Seeger, A., Diffusion in Crvstalline Solids, Edited by Murch, G. E., and Newick, A. S., Academic, NY, 1984.
161. Kung, J. K., and Spitzer, W. G., J. Appl. Phys., 52, 4866 (1969).
162. Morrizumi, T., and Takahashi, K., Jpn. J. Appl. Phys., 8, 348 (1969).
163. Spitzer, W. G., and Allred, W., J. Appl. Phys., 39, 4999 (1968).
164. Weiner, M. E., and Jordan, A. S., J. Appl. Phys., 43, 1767 (1972).
165. Teramoto, I., Jpn. J. Appl. Phys., 18, 1817 (1974).
166. Teramoto, I., J. Phys.Chem. Solids, 33, 2089 (1972).
167. Hurle, D. T. J., J. Phys. Chem. Solids, 43, 639 (1979).
168. Hurle, D. T. J., Paper presented at 5th Conf. on Semi-insulating III-V Materials, Chap. 1, p.11, Malmö, Sweden, 1988.
169. Hurle, D. T. J., J. Phys. Chem. Solids, 40, 627 (1979).
170. Hurle, D. T. J., J. Phys. Chem. Solids, 40, 647 (1979).
171. Kung, J. K., and Spitzer, W. G., J. Appl. Phys., 45, 2254 (1974).
172. Swaminathan, V., and Copley, C. M., J. Appl. Phys., 47, 4405 (1976).
173. Mo, P., Yang, J., Li, S., Jiang, D., and Zhao, H., J. Crystal Growth, 65, 243 (1983).
174. Mullin, J. B., Royle, A., and Benn, S., J. Crystal Growth, 50, 625 (1980).

175. Jaros, M., and Brand, S., Phys. Rev., 14, 4494 (1976).
176. Blashku, A. I., and Dzhaferov, T. D., Krist. Stekloobraznye Poluprovodov, 207 (1977).
177. Il'im, N. P., and Masterov, V. F., Soc. Phys. Semicond., 10, 496 (1976).
178. Prigogine, I., and Defay, R., Chemical Thermodynamics, Longmans, London, 1954.
179. Thurmond, C. D., and Kowalchik, M., Bell System. Tech. J. 39, 1969 (1960).
180. Hwang, C. J., and Brews, J. R., J. Phys. Chem. Solids, 32, 837 (1971).
181. Herbert, D. C., Hurle, D. T. J., and Logan, M. R., J. Phys. C., 8, 3571 (1975).
182. Brozel, M. R., Laithwaite, K., Newman, R. C., and Özbay, B., J. Crystal Growth, 50, 619 (1980).
183. Green, P. D., J. Crystal Growth, 50, 612 (1980).
184. Walukiewicz, W., Lagowski, L., Jastrzebski, L., Lichtensteiger, M., and Gatos, H. C., J. Appl. Phys., 50, 899 (1979).
185. Brozel, M. R., Clegg, J. B., and Newman, R. C., J. Phys. D. (Appl. Phys.), 11, 1331 (1978).
186. Pelevin, O. V., Shershakova, I. N., Gimel'farb, F. A., Mil'vidskii, M. G., and Ukhorskaya, T. A., Sov. Phys. Cryst., 16, 528 (1971).
187. Wilhelmy, L., Ann. Phys., 199, 177 (1863).
188. Neumann, A. W., and Tanner, W., Tenside, 4, 220 (1967).
189. Ruysen, R., Rec. Trav. Chim., 65, 850 (1967).
190. Jordan, D. O., and Lane, J. E., Australian J. Chem., 17, 7 (1964).
191. Davies, J. T., and Rideal, E. K., Interfacial Phenomena, Academic Press, NY, 1961.
192. Tate, T., Phil. Mag., 27, 176 (1864).

## BIOGRAPHICAL SKETCH

Hyeon-Deok Lee was born in Seoul, Korea, on March 7, 1961. He received his B.S. degree in chemical engineering from Yonsei University, Seoul, Korea, in 1984. H then joined the graduate program in the Department of Chemical Engineering, the University of Florida, in August 1984 and received his M.S. degree in chemical engineering in August 1985. After completion of his one-year military service in Korea, he rejoined the graduate program in the Department of Chemical Engineering to continue his study toward a Ph.D degree while working as a research assistant.

I certify that I have read this study and that in my opinion it conforms to acceptable standards of scholarly presentation and is fully adequate, in scope and quality, as a dissertation for the degree of Doctor of Philosophy.



---

Timothy J. Anderson, Chairman  
Professor of Chemical Engineering

I certify that I have read this study and that in my opinion it conforms to acceptable standards of scholarly presentation and is fully adequate, in scope and quality, as a dissertation for the degree of Doctor of Philosophy.



---

Ranga Narayanan  
Associate Professor of Chemical  
Engineering

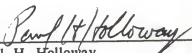
I certify that I have read this study and that in my opinion it conforms to acceptable standards of scholarly presentation and is fully adequate, in scope and quality, as a dissertation for the degree of Doctor of Philosophy.




---

Spyros A. Svoronos  
Associate Professor of Chemical  
Engineering

I certify that I have read this study and that in my opinion it conforms to acceptable standards of scholarly presentation and is fully adequate, in scope and quality, as a dissertation for the degree of Doctor of Philosophy.

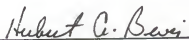
  
Paul H. Holloway  
Professor of Materials Science  
and Engineering


I certify that I have read this study and that in my opinion it conforms to acceptable standards of scholarly presentation and is fully adequate, in scope and quality, as a dissertation for the degree of Doctor of Philosophy.

  
Reza Abbaschian  
Professor of Materials Science  
and Engineering

This dissertation was submitted to the Graduate Faculty of the College of Engineering and to the Graduate School and was accepted as partial fulfillment of the requirements for the degree of Doctor of Philosophy.

May 1991

  
for Winfred M. Phillips  
Dean, College of Engineering

  
Madelyn M. Lockhart  
Dean, Graduate School